

# **Three-Dimensional Simulation of Plasma Spray with Particle Melting and Oxidation**

A Dissertation Presented

by

**Hongbing Xiong**

to

The Graduate School

in Partial Fulfillment of the Requirements

for the Degree of

**Doctor of Philosophy**

in

Mechanical Engineering

Stony Brook University

June 2004

## **Abstract of the Dissertation**

### **Three-Dimensional Simulation of Plasma Spray with Particle Melting and Oxidation**

by

**Hongbing Xiong**

**Doctor of Philosophy**

in

**Mechanical Engineering**

Stony Brook University

**2004**

Plasma spray is widely utilized to deposit finely metallic and nonmetallic particles in a prepared substrate. The combination of coating and base-material can provide resistance to heat, wear, erosion and/or corrosion, as well as unique sets of surface characteristics. The increased demand for thin film coatings of high quality at low cost has motivated extensive research efforts on thermal spraying science and technologies. However, the scientific research has lagged far behind the technological applications due to the complexity of the phenomena involved, e.g., plasma flame generation, heat and momentum transfer to particles, powder injection and reaction with the environment. This dissertation is aimed at developing a fundamental understanding of the transport phenomena during the particles in flight, and investigating the process conditions and optimization. For this purpose, we have developed a comprehensive model that involves major physical mechanisms for plasma spray, *i.e.*, transport phenomena of plasma flame, particle heating, acceleration, evaporation and oxidation. Two plasma

generation systems are studied: direct current (DC) plasma and radio frequency induction coupled plasma (RF-ICP).

For DC plasma spray, a three-dimensional computational model is developed to describe the plasma jet coupled with the orthogonal injection of the carrier gas and the particles. For RF induction plasma spray, a two-dimensional numerical model is developed for the thermo-fluid flow and the induction electromagnetic (EM) field. A comprehensive model describing the melting and oxidation of the in-flight particles during plasma spray is also presented. Special efforts are directed to particle melting, oxidation, evaporation, and non-uniform temperature distribution of particles. These numerical simulations are integrated directly with the experiments and aimed at improving the process control.

An argon-hydrogen DC plasma spray system is studied based on molybdenum and zirconium oxide particles. For this system, the effects of carrier gas and multiple particle injection on the plasma jet are baistudied, in which the numerical method is extended from the two-dimensional LAVA. The heating and melting process of particles with different sizes along their trajectories are predicted, as well as other particle parameters such as velocity, evaporation rate and oxide content. The effects of spray distance, particle size, and carrier gas flow rate on the particle behaviors have also been discussed.

The simulation of RF induction plasma spray process has also been carried out with the feedstock of partially stabilized zirconium oxide powder. The modeling includes two parts. Firstly, the RF heating induced by the electromagnetic field is solved with the Maxwell equations. Then, the temperature and velocity field of the plasma are simulated by solving the Naiver-Stokes equations coupling with the RF heating. Finally, the effects of power level, powder size, and injection position on the plasma generation and the particle behavior are investigated and discussed.

The melting and oxidation behavior of in-flight particles are of vital importance to the coating quality. As a special topic, an order-of-magnitude analysis and one-dimensional thermal network model are employed to investigate the heat and mass transport from the plasma flame to the particle. Two dimensionless parameters, “melting index” and “oxidation index” are derived to characterize the melting status and the oxide content of the in-flight particles, respectively. These two indices are correlated with

experimentally measurable parameters, such as particle size, velocity, temperature, and spray distance.

Numerical simulations and experimental results are used to validate the analytic solutions.

*To my parents*

## Table of Contents

TABLE OF CONTENTS.....	VI
LIST OF TABLES .....	X
LIST OF FIGURES.....	XI
NOMENCLATURE.....	XVI
ACKNOWLEDGEMENT.....	XX
CHAPTER 1 INTRODUCTION.....	1
1.1 <i>Thermal spray technology</i> .....	1
1.2 <i>Literature review</i> .....	7
1.2.1    DC plasma spray.....	8
1.2.2    RF plasma spray.....	13
1.2.3    Particle physics.....	16
1.3 <i>Research objectives</i> .....	21
1.4 <i>Preview of the thesis</i> .....	23
CHAPTER 2 MATHEMATICAL MODEL OF PLASMA FLAME.....	24
2.1 <i>DC plasma</i> .....	24
2.1.1    Plasma source.....	24
2.1.2    Plasma jet.....	25
2.1.3    Chemical reactions .....	27
2.1.4    Turbulence model.....	28
2.1.5    Boundary conditions.....	30
2.2 <i>RF Plasma</i> .....	32
2.2.1    Assumptions.....	32
2.2.2    Electromagnetic field .....	32

2.2.3	Transport model.....	33
2.2.4	Boundary conditions.....	35
CHAPTER 3	INTERACTION BETWEEN PARTICLES AND PLASMA FLAME.....	36
3.1	<i>Particle models</i> .....	36
3.1.1	Acceleration and heating .....	36
3.1.2	Evaporation.....	41
3.1.3	Oxidation.....	43
3.2	<i>Particle effects to the plasma flame</i> .....	45
3.3	<i>Stochastic scheme of multiple particle generation</i> .....	45
CHAPTER 4	COMPUTATIONAL SCHEME.....	47
4.1	<i>Plasma jet</i> .....	47
4.1.1	DC Plasma jet.....	47
4.1.2	RF Plasma jet.....	49
4.2	<i>Particle</i> .....	50
4.2.1	Coordinate transformation of particle equations.....	50
4.2.2	Numerical scheme for particles.....	51
CHAPTER 5	PARAMETRICAL STUDIES OF DC PLASMA SPRAY IN 3-D GEOMETRY.....	52
5.1	<i>Introduction</i> .....	52
5.2	<i>Basic description of the problem</i> .....	54
5.3	<i>Development of LAVA-3D-P</i> .....	55
5.4	<i>Results of 3-D plasma jet</i> .....	62
5.4.1	Effects of carrier gas flow on plasma jet.....	62
5.4.2	Effects of multiple particles.....	69
5.5	<i>Results of particle behavior</i> .....	72
5.5.1	Comparison of single particle behavior in 2D and 3D plasma jet.....	72
5.5.2	Effects of particle size.....	76

5.5.3	Effects of carrier gas flow rates.....	82
5.5.4	Multiple particle spray pattern and the comparison with experiments.....	87
5.5.5	Statistical distribution of particle size, velocity and temperature .....	92
CHAPTER 6	MELTING INDEX AND SIMULATION GUIDED DIAGNOSTIC OF PARTICLE BEHAVIOR .....	99
6.1	<i>Introduction</i> .....	99
6.2	<i>Melting index</i> .....	101
6.3	<i>Oxidation index</i> .....	104
6.4	<i>Determination of the heat and mass transfer coefficients</i> .....	107
6.5	<i>Experimental process</i> .....	108
6.6	<i>Results and discussion</i> .....	108
6.6.1	Melting index.....	108
6.6.2	Melting index for experiments.....	115
6.6.3	Oxidation index .....	118
CHAPTER 7	PARAMETRIC STUDIES OF RF INDUCTION PLASMA SPRAY.....	124
7.1	<i>Introduction</i> .....	124
7.2	<i>Basic description of the problem</i> .....	125
7.3	<i>Validation of the electromagnetic model</i> .....	127
7.4	<i>Results of magnetic, flow and temperature fields of argon plasma</i> .....	130
7.5	<i>Results of particle behaviors</i> .....	135
7.5.1	Effects of particle injection position.....	135
7.5.2	Effects of particle size .....	135
7.5.3	Multiple particles behavior.....	136
CHAPTER 8	CONCLUSIONS AND RECOMMENDATIONS .....	141
8.1	<i>Conclusions</i> .....	141
8.1.2	3-D simulation of DC plasma spray.....	141

8.1.2	2-D simulation of RF plasma spray .....	142
8.1.3	Melting index .....	142
8.2	<i>Recommendations</i> .....	143
APPENDIX	.....	144
	<i>A: Reaction Mechanisms for an Ar + H<sub>2</sub> Plasma into Air.....</i>	144
	<i>B: Differential form of governing equations for DC plasma flame.....</i>	144
REFERENCES	.....	146

## **List of Tables**

Table 1.1: Summary of selected model and simulation results in DC plasma research.....	11
Table 1.2: Summary of selected model and simulation results in RF plasma research.....	16
Table 1.3: Summary of selected model in particle-plasma interaction research.....	20
Table 1.4: Summary of selected experimental results in particle-plasma interaction research.....	21
Table 5.1: Basic operating conditions for DC plasma torch .....	54
Table 5.2: Particle conditions and properties.....	55
Table 5.3: Operating conditions for the DC plasma torch in 2D and 3D.....	58
Table 5.4: Operating conditions for the benchmark case .....	61
Table 6.1: Operating conditions for plasma spraying of ZrO <sub>2</sub> and Mo. ....	102
Table 6.2: Simulation results of the oxidation index of Mo at spray distance of 15 cm .....	120
Table 7.1: Operating conditions for RF induction plasma spraying. ....	126

## List of Figures

Figure 1.1: Schematic of DC plasma spray process.....	4
Figure 1.2: Schematic of RF induction plasma spray.....	6
Figure 1.3: Schematic of an inductively coupled RF discharge.....	14
Figure 3.1: Schematic of particle heat transfer.....	38
Figure 3.2. Random distribution of particle size.....	46
Figure 4.1: Computational cells for plasma jet domain at x and y directions.....	48
Figure 4.2: Computational cells for particle transport equations.....	52
Figure 5.1: Geometry, computational mesh and boundary conditions in: (a) cross section plane in radial and azimuthal directions, (b) middle section plane of 3D plasma jet.....	55
Figure 5.2: (a) ZrO <sub>2</sub> and (b) NiCrAlY particle size distribution and the data achieved in the simulation.....	57
Figure 5.3: (a) Gas temperature, (b) radial velocity, (c) axial velocity, and (d) circular velocity obtained from the LAVA 2D (dash line) and LAVA 3D at $\theta = 90^\circ$ (solid line) at the spray distance of 0.5, 1.0, 2.5, 5.0 and 10.0 cm.....	59
Figure 5.4: Trajectories of particles calculated from LAVA 2D and LAVA 3D models, respectively... ..	60
Figure 5.5: (a) Particle velocity and (b) temperatures of particle surface and gas surrounding the particles calculated from LAVA 2D and LAVA 3D models, respectively. ....	60
Figure 5.6: Particle velocity along the centerline of the side injector after particles exit from the injector, where the solid-line represents the simulation result, and symbols are experimental results [Fincke, 1997 and 2000]. ....	62
Figure 5.7: Comparison of (a) gas temperature contours and (b) velocity vector at the ABCE plane (indicated in Fig. 1.1) with carrier gas flow rate of 4.5 slm and without carrier gas.....	64
Figure 5.8: Temperature contour and gas velocity vector at the cross section S-S (see Fig. 1) near the injector with carrier gas flow rate of 3 slm.....	65

Figure 5.9: (a) Gas temperature contours and (b) velocity vector at the ABCE plane (indicated in Fig. 1.1) for carrier gas flow rate of 15 slm.....	66
Figure 5.10: (a) Gas temperature profiles and (b) axial velocity profiles at the cross lines in the ABCE plane (lines parallel to AB or CE in Fig. 1.1) for carrier gas flow rate of 15 slm. ....	67
Figure 5.11: Effects of carrier gas flow rate on gas radial velocity at the centerline of the plasma jet....	68
Figure 5.12: (a) Gas axial velocity and (b) temperature at the cross line away from nozzle 5 cm. The solid, dotted, and dash-dot lines are for cases without carrier gas and with carrier gas flow rates of 3 and 6 slm, respectively.....	68
Figure 5.13: Temperature contour of 3D plasma jet flow with multiple Mo particles injected along with carrier gas of argon.....	69
Figure 5.14: Radial velocities at cross lines of the flow field before and after multiple Mo particles injected. ....	70
Figure 5.15: Axial velocities at cross lines of the flow field before and after multiple Mo particles injected. ....	70
Figure 5.16: Temperature at cross lines of the flow field before and after multiple Mo particles injected. ....	71
Figure 5.17: (a) The gas axial velocity and (b) temperature at the cross line away from nozzle 5 cm. The solid, dash, and dash-dot lines are for cases with carrier gas of 6 slm, and then with ZrO <sub>2</sub> particles injection, and without carrier gas respectively.....	72
Figure 5.18: ZrO <sub>2</sub> Particle trajectories with and without carrier gas effects.....	73
Figure 5.19: ZrO <sub>2</sub> Particle velocities with and without carrier gas effects.....	74
Figure 5.20: ZrO <sub>2</sub> Particle temperatures with and without carrier gas effects.....	74
Figure 5.21: Deposition location of ZrO <sub>2</sub> Particles with and without carrier gas of Ar 3 slm.....	75
Figure 5.22: Velocity of ZrO <sub>2</sub> Particles with and without carrier gas of Ar 3 slm.....	75
Figure 5.23: Surface temperature of ZrO <sub>2</sub> Particles with and without carrier gas of Ar 3 slm.....	76

Figure 5.24: Effects of particle size on ZrO <sub>2</sub> particle behaviors: (a) trajectories, (b) velocity, (c) temperature, and (d) evaporation rate. The carrier gas flow rate is 6 slm.....	79
Figure 5.25: Effects of particle size on Mo particle behaviors: (a) trajectories, (b) velocity, (c) temperature, (d) evaporation rate and (e) oxide content. The carrier gas flow rate is 3 slm....	81
Figure 5.26: Effects of carrier gas flow rate on ZrO <sub>2</sub> particle behaviors: (a) trajectories, (b) velocity, (c) temperature, and (d) evaporation rate.....	84
Figure 5.27: (a) Diameter, (b) temperature and (c) velocity distributions of multiple ZrO <sub>2</sub> particles on the substrate. The carrier gas flow rate is 1.5 slm.....	85
Figure 5.28: (a) Diameter, (b) temperature and (c) velocity distributions of multiple ZrO <sub>2</sub> particles on the substrate. The carrier gas flow rate is 3 slm. ....	87
Figure 5.29: (a) Spray pattern centroid position and (b) width for ZrO <sub>2</sub> and NiCrAlY as a function of carrier gas flow rate.....	90
Figure 5.30: (a) Average particle temperature and (b) velocity for ZrO <sub>2</sub> and NiCrAlY as a function of carrier gas flow rate.....	91
Figure 5.31: Histograms for particle size, velocity and temperature of ZrO <sub>2</sub> particles with diameter of 10~60 μm at the spray distance of 8 cm .....	94
Figure 5.32: Histograms for particle size, velocity and temperature of ZrO <sub>2</sub> particles with diameter of 10~60 μm at the spray distance of 10 cm.....	95
Figure 5.33: Histograms for particle size, velocity and temperature of ZrO <sub>2</sub> particles with diameter of 10~60 μm at the spray distance of 15 cm (light gray), with the dark gray histograms indicating the distributions of specified size particles: (a) small particles and (b) large particles.....	96
Figure 5.34: Distributions of (a) particle temperature and (b) particle enthalpy at spray distance of 8 cm for the ZrO <sub>2</sub> particles with diameter of 50 μm.....	97
Figure 5.35: Experimental result of ZrO <sub>2</sub> particle temperature distributions.....	98

Figure 6.1: SEM picture of the splat formed (a) by a totally melted ZrO <sub>2</sub> particle and (b) by a partially melted ZrO <sub>2</sub> particle.....	102
Figure 6.2: Schematic of the in-flight particle melting process .....	103
Figure 6.3: Schematic of the in-flight particle oxidation process: (a) cross section of an oxidized particle, (b) mass transfer and diffusion of oxidant through the particle.....	105
Figure 6.4: (a) Particle velocity, and (b) surface temperature for different sizes of ZrO <sub>2</sub> particles, with experimental data (in courtesy of L. Li, A. Vaidya and S. Sampath). ....	112
Figure 6.5: (a) Heat transfer coefficient, (b) flame temperature, (c) dimensionless temperature $A = (T_f - T_m)/(T_s - T_m)$ and (d) melting index vs. the non-dimensional melting radius, $r^* = (r_p - r_m)/r_p$ , for ZrO <sub>2</sub> particles. ....	115
Figure 6.6: (a) SEM pictures of collected splats and (b) effects of melting index on deposition rate at different spray distances of 6, 8, 10 and 12 cm (in courtesy of L. Li, A. Vaidya and S. Sampath). ....	118
Figure 6.7: Effects of melting index and particle Reynolds number on splat fragmentation degree (in courtesy of L. Li, A. Vaidya and S. Sampath). ....	118
Figure 6.8: (a) Mass transfer coefficient, (b) mass fraction of oxygen in the gas phase, and (c) oxide content vs. the spray distance for Mo particles with diameters of 20, 30, 40, 50 and 60 $\mu\text{m}$ .....	122
Figure 6.9: Oxide content at the spray distance of 10 cm vs. $(V_p d_p^2)^{-1}$ , for Mo particles with diameters of 20, 30, 40, 50 and 60 $\mu\text{m}$ .....	123
Figure 7.1: SEM pictures of RF sprayed ZrO <sub>2</sub> splats and coatings. ....	125
Figure 7.2: Contour of the vector potential ( $\text{A H m}^{-1}$ ) for the constant electrical conductivity load $\sigma = 1500 \Omega^{-1} \text{ m}^{-1}$ : (a) the real part, and (b) the imaginary part .....	127

Figure 7.3: Radial profiles at $x = 136$ mm of (a) real part of the axial magnetic field $H_x$ ( $A\ m^{-1}$ ), (b) real part of the induced current density $J_{ind}$ ( $A\ m^2$ ), for different electrical conductivities of the load.....	130
Figure 7.4: Contour of the vector potential ( $A\ H\ m^{-1}$ ) for the argon plasma: (a) the real part, and (b) the imaginary part.....	131
Figure 7.5: (a) Temperature contours of argon plasma with different power input: (Maximum = 10192 K, minimum = 1030 K, incremental value = 1018 K and operating conditions are given in Table 7.1); (b) Streamlines of the plasma flow fields with different power input...	133
Figure 7.6: (a) Contours of the Joule heating $Q_J$ ( $W\ m^3$ ) in the plasma for argon plasma with different power input: (Minimum = $4.5 \times 10^7$ , incremental value = $4.5 \times 10^7$ ); and (b) Contours of the radial Lorentz force $F_r$ ( $N\ m^3$ ): (Maximum = - 600, incremental value = - 600).....	134
Figure 7.7: (a) Trajectory (b) velocity and (c) surface and center temperatures of $ZrO_2$ particle in RF plasma spray with different injection location of 8 and 10 cm.....	138
Figure 7.8: (a) Trajectory (b) velocity and (c) surface and center temperatures of $ZrO_2$ particle in RF plasma spray with different diameter of 60 and 80 $\mu m$ .....	140
Figure 7.9: Histograms for particle velocity, temperature and diameter of $ZrO_2$ particles in RF plasma spray with initial diameters ranging from 50 and 110 $\mu m$ .....	140

## Nomenclature

$A$	vector potential, A H m <sup>-1</sup>
$B$	magnetic flux density, T
$B_m$	mass transfer number
$Bi$	Biot number, $Bi = hr_p / k_l$
$Bi_m$	mass transfer Biot number, $Bi_m = r_p h_m / \rho_l D_{o,l}$
$C_p$	specific heat, J kg <sup>-1</sup> K <sup>-1</sup>
$C_D$	drag coefficient
$d_p$	particle diameter, m
$D$	diffusion coefficient, m <sup>2</sup> s <sup>-1</sup>
$e$	internal energy per unit mass, J kg <sup>-1</sup>
$E$	electric field, V m <sup>-1</sup>
$f$	frequency, Hz
$f_{Kn}$	factor of Knudsen number
$f_{\text{prop}}$	factor to account property variation
$f_v$	factor for mass transfer
$F$	force, N m <sup>-3</sup>
Fo	Fourier number, $Fo = \alpha_l t / r_p^2$
Fo <sub>m</sub>	Mass transfer Fourier number, $Fo = D_{o,l} t / r_p^2$
$h$	heat transfer coefficient, W m <sup>-2</sup> K <sup>-1</sup>
$h_m$	mass transfer coefficient, kg m <sup>-2</sup> s <sup>-1</sup>
$J$	current density, A m <sup>-2</sup>
$k$	thermal conductivity, W m <sup>-1</sup> K <sup>-1</sup>
$L_m$	latent heat of fusion, J kg <sup>-1</sup>

$L_{evap}$	latent heat of evaporation, $\text{J kg}^{-1}$
$\dot{m}_v$	vaporization rate, $\text{kg s}^{-1}$
$\dot{m}_{ox}$	oxidation rate, $\text{kg s}^{-1}$
$p$	pressure, $\text{kg m}^{-1} \text{s}^{-2}$
Pr	Prandtl number
$q$	heat flux, $\text{J m}^{-2} \text{s}^{-1}$
$\dot{Q}_{conv}$	convection heat transfer rate, $\text{J s}^{-1}$
$\dot{Q}_{rad}$	radiation heat transfer, $\text{J s}^{-1}$
$\dot{Q}_{vap}$	heat transfer rate for vaporization, $\text{J s}^{-1}$
$r$	radial coordinate, m
$r_m$	position of the melting interface, m
$r_p$	particle radius, m
Re <sub>p</sub>	Reynolds number
$S$	Spray distance, cm
$Sc$	Schmidt number
$Sh$	Sherwood number
$t$	time, s
$T$	temperature, K
$T_m$	melting point, K
$T_s$	particle surface temperature, K
$\mathbf{V}$	velocity vector, $\text{m s}^{-1}$
$\mathbf{V}'$	velocity fluctuation, $\text{m s}^{-1}$
$\mathbf{V}_p$	particle velocity, $\text{m s}^{-1}$
$u, v, w$	fluid velocity components, $\text{m s}^{-1}$

$W$  molecular weight, kg mol<sup>-1</sup>

$x, y, z$  coordinate, m

$Y_o$  oxidant concentration

### Greek symbols

$\alpha$  thermal diffusivity, m<sup>2</sup> s<sup>-1</sup>

$\varepsilon$  emissivity

$\delta$  skin depth, m

$\theta$  circular coordinate

$\mu$  viscosity, kg s<sup>-1</sup> m<sup>-1</sup>

$\mu_0$  permeability in vacuum,  $4\pi \times 10^{-7}$  H m<sup>-1</sup>

$\rho$  density of gas mixture, kg m<sup>-3</sup>

$\rho_p$  density of particle, kg m<sup>-3</sup>

$\Phi$  viscous dissipation, kg m<sup>-1</sup> s<sup>-3</sup>

$\omega$  angular frequency, rad s<sup>-1</sup>

$\sigma$  electrical conductivity, S m<sup>-1</sup>

### Subscript

$i$  species  $i$

$f$  film temperature

$l$  liquid

$p$  particle

$s$  solid

$t$  turbulence

$w$  wall

$\infty$  environment

**Superscript**

$c$  chemical reaction

## **Acknowledgement**

I would like to express my sincere gratitude and appreciation to my research advisor, Dr. Lili Zheng, for her constant support, encouragement and guidance through out my Ph.D. program. Her desire for precision, enthusiasm for exploring and spirit for scientific inquiry are the most valuable treasures that I learned from her. I would also like to give my special thanks to Dr. Hui Zhang, for his inspiring advice and comments. I would also like to thank Dr. S. Sampath in Material Science Department and Dr. J. Fincke and Dr. Williamson in INEEL Laboratory for their suggestions and support on this work.

I also own many thanks to my colleagues in our lab and in Center of Thermal Spray Research, for their helps with my research.

Deepest thanks go out to my family. The encouragements and love from my parents and sister helped me to finish my Ph.D. program successfully. Special thanks go to my husband, Yuan Ma, for his comfort and support.

I would like to acknowledge the sponsorship of this research by the NSF POWRE program (Grant # 0074589) and the NSF MRSEC Program (Grant #0080021), as well as the Department of Energy INEEL through a subcontract.

# **Chapter 1**

## **Introduction**

Thermal spray process is a versatile and widely used technology, for providing protective coatings to material surfaces. It involves the formation of a combustion or plasma flame, feeding fine metal or ceramic particles into the hot zone of the flame, and particle deposition on the targeted substrate. During the short time of in-flight, the particles are rapidly heated, forming a spray of partially or completely melted droplets, which facilitates the process of particle impact, spreading and solidification onto the prepared substrate and form the protective coating. Typically, this protective coating can improve the base material's resistance to heat, wear, erosion or corrosion, depending on the particle material. Since the momentum, heat and mass transports govern this process, control of these phenomena is critical to the mechanical and thermal properties of the coatings. Due to the increased interest in thermal spray coatings from military and commercial sectors, much research has been dedicated to thermal spraying science and technologies. However, the scientific research has lagged far behind the technological applications due to the complexity of the phenomena involved, e.g., the phase-change and oxidation of the in-flight particles. In this chapter, the current thermal spray knowledge is briefly reviewed, including the heat, mass and momentum transport processes in thermal spray and the versatility of the industrial thermal spray technologies.

### **1.1 Thermal spray technology**

Thermal spray is a technological group, including combustion spray, arc spray, plasma spray, cold spray and so on. Various protective coatings from thermal spray have wide applications in the industry. For example, the wear-, chemical- and thermal barrier coatings are desirable for the aerospace and automotive industries, and high temperature-erosion protection for boiler tubes and fire chambers of coal-fired power plants. Main advantage of this coating technology is that it combines two dissimilar materials, resulting in composites that enhance the performance of the coatings or that create new functional properties. Generally, coatings of high performance materials, such as metal, alloy or ceramic, are applied to

relatively easy-to-work and more economical base materials, by various thermal spray techniques. Thermal barrier coating is one of the best-known applications of ceramics, whereas metallic coatings are mostly used to improve corrosion, oxidation and wear resistance. This technique is also being widely used to repair and resurface metallic parts.

Different heat sources have been used for thermal spray techniques: combustion or plasma. Among the five basic thermal spray processes available commercially, the flame spray, high velocity oxygen fuel spray (HVOF), and detonation (D-gun) are three of the processes associated with combustion, whereas wire arc and plasma spray are two other processes that utilize electric energy to help melt consumable materials. Cold spray is a new process that relies more on high kinetic energy and less on thermal energy. For spray with combustion flames, gas temperature and its enthalpy are defined by the gas composition and the pressure, with maximum gas temperature of about 3000 K. For plasma, the temperature and enthalpy are defined by electrical power supplied, gas flow rate and composition, nozzle shape and its diameter. Usually, low-temperature plasma is used for plasma spray, with temperature ranges from  $10^3$  to  $10^4$  K. In the next part, a brief overview of these five basic thermal spray processes will be given: flame spray, wire arc spray, HVOF spray, D-gun spray and plasma spray.

*Flame spray.* Flame spray is among the oldest methods of applying thermal spray coatings. According to the different forms of feeding materials, the flame spray includes wire flame spray and powder flame spray. Combustion flame spray is achieved by burning a mixture of oxygen and hydrocarbon (acetylene, propane, etc.) or hydrogen in a torch having a flame-accelerating nozzle. For material in wire form, the flame is concentric to the wire fed through the nozzle axis. Combustion gas melts, atomizes, and propels molten particles to the surface for coating. For powder flame spray, powders are injected into the flame nozzle by carrier gas, where they melt and are projected to the surface.

*Wire arc spray.* In wire arc spray, two consumable wire electrodes of either identical (conventional wire arc process) or dissimilar (pseudo-alloy process) metals are melted and the liquid metal is projected onto a substrate. The necessary thermal energy required to melt the wires is produced by means of an electric arc developed between the electrodes by applying a potential difference across the wires. An electric arc is

produced by the passage of electric current through an ionized gas. High current density leads to the generation of heat in the ionized gas, and thereby causes fusion of the two-wire electrodes. An atomizing gas, usually compressed air, is directed through the arc-zone to form a relatively high-velocity melt spray. The various arc-spraying parameters influencing the atomization process are: atomizing gas pressure, wire diameter, arc potential difference and wire feed rate. The main advantage of arc spray is the much higher deposition rates as compared to plasma or flame spraying, as high as 40 kg/h.

HVOF. The high velocity oxygen fuel spray (HVOF), introduced by Jet Kote in the 1980s, is based on the internal combustion in a water-cooled chamber with high-pressure (0.4 MPa to 1.35 MPa). It becomes another popular spray technology besides plasma spray technology since the coating applied by this process exhibits good density, hardness and bond strength characteristics. In this device, high pressure was produced continuously due to combustion in a pressurized water-cooled chamber from where the combustion gases expanded through a nozzle as they exhaust to the atmosphere. Hence, the particles inside this high-pressure chamber, where Mach number can reach 4, can be accelerated to high velocity in the range of 400-800 m/s, and tend to produce high density and high bond strength coatings. The spray rate ranges from 2 to 4 kg/h. The HVOF is mainly used for relatively low melting point materials such as metals, alloys and cermets. The high velocity air fuel spray (HVAF) is another thermal spray process using combustion flame.

D-gun spray. Detonation gun (D-Gun) is a combustion process marketed by Union Carbide. It can produce premium metallic and cermets coatings, with many advantages such as higher density, improved corrosion barrier, higher hardness, better wear resistance, higher bonding and cohesive strength, almost no oxidation, thicker coatings and smoother as-sprayed surfaces, compared to other thermal spray techniques [Thorpe, 1992]. However, it was available only as a service, and not much research work was published on this process. The Detonation gun basically consists of a long water-cooling barrel (about 1 m long with diameter of 25 mm) with inlet valves for gases and powder. Oxygen and fuel (acetylene most common) are fed into the barrel along with a charge of powder. A spark is used to ignite the gas mixture and the resulting detonation heats and accelerates the powder to supersonic velocity down the barrel. A

pulse of nitrogen is used to purge the barrel after each detonation. This process is repeated many times a second (3-7 detonation per second), with noise sound level larger than 150 db. The high kinetic energy of the hot powder particles, achieving particle velocity of 600-800 m/s upon impact with the substrate, results in a build-up of a very dense and strong coating.

DC plasma spray. Plasma spray process consists of three parts: gun used for generating high temperature flame jet, particles in-flight, and substrate deposition. The plasma flame jet, is produced in the arcs formed by a direct current (DC) discharge or in a torch heated by the radio frequency (RF) coil. Figure 1.1 shows the schematic of DC plasma spray process, in which a high temperature gas mixture is generated inside the plasma gun and is looped out of the nozzle exit to form a plasma flame. The powder materials, usually with diameter from 5 to 100  $\mu\text{m}$ , are introduced from the internal or external injectors thanks to the carrier gas. When the particles flying through the flame jet, they are heated and accelerated towards the substrate, and eventually deposited on the substrate layer by layer. Usually, the DC plasma gun contains a cone-shaped tungsten cathode (W-2wt%Th) inside a cylindrical copper anode, which is water-cooled to prevent overheating.

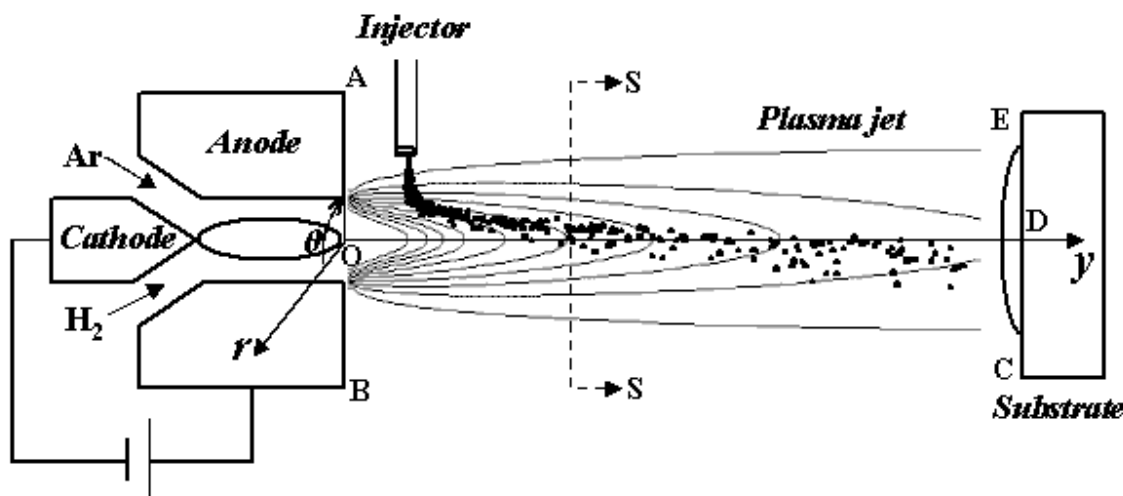


Figure 1.1: Schematic of DC plasma spray process

The main advantage of this process is that there is no limitation to the melting temperature of the sprayed materials. It dramatically extends the technology possibility to any material that could be melted, including refractory ceramics. Plasma spray is also highly efficient, reliable and easy to handle. Because of these advantages, plasma spray has become one of the most common techniques to produce functional coatings. The typical feeding rate of plasma spray is 3-5 kg/h. The plasma spray process is cost-effective, and is an excellent fit for applications where the extremely low porosity is not a priority and where substantial amounts of material must be applied. It is also the only method by which ceramics can be efficiently thermally sprayed.

This process can be carried out under various environments, such as atmospheric plasma spray (APS), vacuum plasma spray/low pressure plasma spray (VPS/LPPS), water plasma spray, etc. The use of VPS or LPPS makes it possible to suppress some important drawbacks of APS. During air plasma spraying (APS), turbulent mixing with atmosphere causes the velocity and temperature of the plasma flame to decrease rapidly with distance from the nozzle exit. Also, depending upon the reactivity of the metal and the gases present in the environment, particle-gas reaction products (e.g., oxides and nitrides) are commonly present in the spray-deposit. However, during VPS, the absence of turbulence-induced mixing results in a significantly enlarged and lengthened plasma flame. Another advantage of VPS over APS is the absence of greatly reduced particle-environment reactions, which yields dense coatings with almost no oxidation. The disadvantage of VPS is, firstly, the much higher expense of investments. Secondly, the large plasma flames obtained in VPS result in a lower energy density of the flame, which necessitate higher electric power and longer spray distances to ensure complete melting of the powder particles. The inert plasma spray (IPS) process is also used to reduce the oxidation and chemical composition, but it also requires considerable capital cost and running expenses. The plasma jet using high DC power up to 200 kW (Plazjet gun) is also available to achieve high deposition rate up to 17 kg/h. *RF induction plasma spray.* Other than DC plasma spray, RF induction plasma spray utilizes the radio frequency heating to create an inductively coupled plasma plume in the torch (see Fig. 1.2). The RF plasma flame has a high temperature ranging from 5000 to 10 000 K, depending on the plasma gas

composition. It has the advantages of stability, cleanness, large volume, high temperature and high chemical reactivity. This is benefited from two characteristics of RF induction plasma. Firstly, the plasma source can be produced in the absence of electrodes. Secondly the plasma chemical reaction time is longer compared to DC discharge. The axial injection of feedstock materials is another significant advantage of this system, which makes the particle or precursor feeding much easier. Since the RF induction plasma torch can produce low-gas velocities by controlling the gas injection, particles have longer residence time than those in the DC plasma. Therefore, particles can be heated more thoroughly in RF plasma spray, even for large particles with diameters over 100  $\mu\text{m}$ .

The RF torch can be operated under a wide range of conditions with oxidizing gas, reducing atmosphere or inert plasma gas environments. The exit nozzle used in the RF torch can also be changeable: divergent, convergent or convergent-divergent, depending on the application. Divergent nozzles are recommended for powder spheroidization while convergent nozzles are best adapted to film deposition. Convergent-divergent nozzles can be used for the deposition of nano-structured coating, which provide the acceleration of the molten droplets towards the substrate.

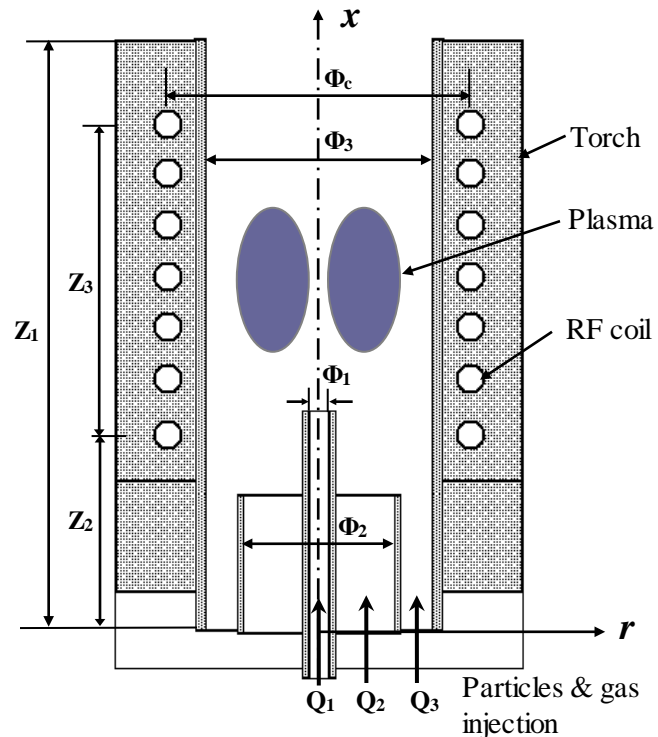


**Figure 1.2: Schematic of RF induction plasma spray**

## 1.2 Literature review

There has been growing interest in thermal spray processing of materials in the past years, with the existing applications widen and new applications explored. Many experimental and numerical studies are conducted in this area to understand the fundamental phenomena involved in this process and to optimize the operating parameters for the improvement of the coating quality. However, such study is difficult since this process involves many physical phenomena and chemical reactions. Although the trial and error experimental method with proper post-sample analysis has provided a tool to understand the plasma and particle behaviors, it suffers from high cost, long cycle duration, and insufficient information that can be acquired. As the results, numerical simulation becomes an alternative tool to provide insights of physical and chemical processes occurring in the plasma jet and in-flight particles. It allows extensive studies of many issues such as particle size, velocity, temperature and phase composition. Note that evaporation and oxidation of the particles, among the major process concerns but difficult for experiment measurements, can also be studied with numerical method.

However, the plasma spraying modeling is also difficult due to the complicated physical, chemical and statistical problems involved. Firstly, the plasma jet exhibits unusual properties: *i.e.*, for DC plasma flame, high flow velocities (up to 2500 m/s) and high temperatures (up to 14 000 K), steep temperature and velocity radial gradients (up to  $10^7$  K/m and  $5 \cdot 10^5$  /s) and low gas density (1/30 to 1/50 that of the cold gas). They are laminar in their core and turbulent in their fringes, associated with the entrainments of ambient air which is heated and mixed with the hot plasma gas. Then, the solid particles are injected into the plasma jet through an injector with trajectory, velocity and temperature distributions at the injector exit, which are caused by particle collisions between themselves and the injector wall. It results in a dispersion of their trajectories and thus acceleration and heating within the jet, and adds the difficulty in the modeling and coating control. Beside heating and acceleration, the particles in the plasma jet also experience phase change and possible chemical reactions before impacting, spreading and solidified on the substrate.

### 1.2.1 DC plasma spray

Plasma physics. The high temperatures plasma (greater than 15,000 K is possible), which allows the melting and deposition of refractory materials, is produced when sufficient energy is transported to the gas being ionized. Plasma is a dense cloud of electrons, ions, atoms and molecules, defined as the fourth state of matters. There is no clear-cut boundary between the plasma and the gas. The plasma retains many of the properties of gases and also satisfies the physical laws valid for gases. Specific properties of plasma different from the neutral gases rely on its response to electro-magnetic forces [Dembovsky, 1985].

The DC plasma is generated by arc discharge formed between two electrodes. When an electric arc is struck in a gas, electrons are emitted from the cathode. These electrons collide with the atoms, thus these atoms can be excited or ionized. The ionization frees electrons which are accelerated, and, by a cascade, free other electrons. As the reaction continues, the number of charged particles increases until the gas becomes highly conductive. Under this condition a breakdown may occur whereby gas and sparks may pass through the gas from the cathode to the anode. This breakdown is characterized by a large increase in current flow and electron emission. The frequency of collisions also increases and subsequently increases the temperature of the plasma. The higher temperatures further increase the conductivity and result in additional current flow. The process escalates until being limited by the resistance of the arc source.

The plasma gas is ionized inside the torch. When the collision between ions, atoms and electrons is frequent enough to establish the steady state, the stabilized thermal plasma is formed: the thermodynamic state of the plasma approaches local thermodynamic equilibrium (LTE). The assumption of local thermodynamic equilibrium is only valid when the plasma temperature is high and pressure is high while it is at low voltage field. However, the increasing evidence that the existence of LTE even in atmospheric pressure plasmas, is the exception rather than the rule. Both measurements and modeling confirmed deviations from chemical and/or kinetic equilibrium [Heberlein, 1999].

The temperature, as well as the degree of ionization, of the plasma is governed by the rate at which energy is supplied and the inherent ionization energy of the atoms involved. Conventional gas stabilized

plasma guns normally operate at power levels of about 40 kilowatts. Using the water stabilized plasma spray (WSP), higher power level around 160 kilowatts can be used to achieve a high production rate [Herman, 1996].

There are two basic gases used in the plasma gas: atomic gas such as Ar, He, and molecular gas such as H<sub>2</sub>, N<sub>2</sub>, O<sub>2</sub>. The molecular gas has much higher enthalpy and specific heat, since it can absorb more energy when dissociation firstly occurs before its ionization. The primary plasma gas prefers to noble gas as Ar, due to its no reactivity with the processed materials. In order to optimize the thermodynamic properties of the plasma gas, such as enthalpy, thermal conductivity and viscosity, the secondary gas (H<sub>2</sub>, N<sub>2</sub>, He) are introduced at a proper ratio. For example, adding H<sub>2</sub> to Ar can increase its enthalpy and thermal conductivity dramatically and decrease the viscosity [Boulos, 1994].

The high temperature of the plasma is reduced near the walls of the water-cooled anode, leading to a boundary layer of low electrical conductivity [Dembovsky, 1985]. This layer compresses the plasma, leading to an increase in the temperature and pressure at the core of the plasma. This is known as the thermal pinch effect. A magnetic pinch is concomitant with the thermal effect because the core of the plasma is electrically conductive and the electric field lines encircle the plasma flame, further confining plasma core and increasing its energy density.

DC Plasma torches fall into two categories: transferred arc and non-transferred arc. The transferred arc requires that the substrate being sprayed be the anode, with the torch acting as the cathode. A more common design is the non-transferred arc, which has both the cathode and anode incorporated in the torch.

*Flame jet and turbulence flow.* A number of numerical models have been proposed to simulate plasma spray process [Lee, 1984; Amsden, 1989; Chang, 1990]. Most models considered only the plasma jet outside the torch, assuming velocity and temperature distributions at the nozzle exit matching with the plasma gas mass flow rate and its enthalpy. Recently, Mariaux [2003] developed a 3D transient model of plasma spray, in which the conversion of energy in the torch nozzle, from electric power to thermal energy, is considered. The power generation is assumed uniform throughout the medium and takes into account as a source term in the heat equation. This simple model yielded an estimation of the effective

power of the gun. However, no comprehensive and reliable model can currently take into account the arc column inside the torch with its attachment to the anode-nozzle wall, which is a full 3-D unsteady state problem. Haddad et al. [Haddad, 1989] had extended the simulation to the interior of the torch to remove the assumption of torch exit conditions. However, the results did not agree well with the experimental measurements because of over simplifications. The local thermodynamic equilibrium is generally assumed except for the two-temperature model studied by Chang et al. [1996], in which the electrons and heavy particles have different temperatures. He treated the plasma as a compressible, continuous multi-component, chemically reacting ideal gas with temperature-dependent thermodynamic and transport properties.

Most numerical simulations have been conducted in a 2-D computational domain in which the axisymmetric assumption is necessary. In reality, the plasma jet exhibits three-dimensional behavior due to the side jet injection of particles and the fluctuation of the plasma jet. Therefore, a transient three-dimensional model is needed to fully simulate the effects of side carrier gas jet and injected particles. Ahmed and Bergman [2001] studied the ceramic particles in Ar-H<sub>2</sub> plasma jet using a 3-D model coupled with the commercial computational code FLUENT. Vardelle et al. [2001] have performed 3-D simulations for the plasma spray process using the commercial computational fluid dynamics code ESTET. Li and Chen [2001; 2002] developed a three-dimensional computational model that is capable of handling transverse carrier gas injection and its influence on the plasma jet behavior and particles trajectories. Noted that most three-dimensional models so far are based on the assumption: the particle temperature is uniform across the radius during in-flight, and some models neglect the effects of particles on the plasma gas.

Turbulence influences the plasma jet significantly. As the plasma jet exits the nozzle, it encounters a steep laminar shear layer at the outer edge of the jet. The large velocity difference causes rolling-up of the shear layer flow around the nozzle exit into a ring vortex, which is pulled downstream by the flow, allowing the process to repeat itself again at the nozzle exit. Adjacently formed vortex rings at the outer edge of the jet have the tendency to coalesce, forming larger vortices; perturbations to these vortices then

lead to wave instabilities growing around the entire ring. Next, the distorted vortex rings start entangling themselves with adjacent rings, finally resulting in total breakdown of the vortex structure into large-scale eddies and the onset of turbulent flow.

Various models have been adopted in the numerical simulations of turbulent jet under plasma conditions: mixing hypothesis [Shaeffer, 1978], two-equation  $k - \varepsilon$  model [Chang, 1993], multiple time scale turbulence model [Lee, 1983], etc. The most commonly used model is the  $k - \varepsilon$  model, if necessary, with the correction to account for low Reynolds number. Although the results predicted by the  $k - \varepsilon$  model are not satisfactory, it has provided semi-quantitative information on the plasma jet. Some researchers turned to more sophisticated turbulence model, and found that the multiphase models could be a better one for turbulent flow. Huang et al. [1995] developed a two-fluid model for an argon plasma jet flowing into an argon stagnant environment. In their study, the plasma jet was considered as a two-fluid mixture consisting of hot, out-moving fragments and cold, in-moving fragments.

**Table 1.1: Summary of selected model and simulation results in DC plasma research**

Author & references	Model and simulation	Comments
Haddad [1989]	Model the interior of the torch but the results did not agree well with experiment	Over simplification.
Ramshaw and Chang [1995]	Implicit calculation of kinetics and equilibrium chemical reaction.	
Chang and Ramshaw [1990]	Model of compressible multi-component and bipolar diffusion plasma flow.	Comprehensive model
Ahmed [2000]	3D model to study melting of the ceramic particles.	Using commercial code FLUENT
Vardelle [2001]	3D simulation of plasma jet generation and particle injection.	Using commercial code ESTET
Huang [1995]	Two-fluid turbulence model, which considered two parcels: in-moving and out-moving.	
Chang and Ramshaw [1996]	Model the non-equilibrium effects in nitrogen and Hydrogen plasma.	

Issues and Challenges. The growth of this technology has been relatively slow for two reasons: there is still a lack of a solid engineering base in terms of control, reproducibility, and optimization of the thermal plasma spray process, and there is only a limited range of applications that appear to be economically viable, based on present technology. It is anticipated that with recent modeling and experimental advances,

our knowledge of thermal spray can be enhanced and the controlling of the process can be improved, i.e., establishing control parameters for optimizing the process. The modeling of plasma spray is hampered by the complicated physical and chemical phenomena occurring in the plasma generation and propagation, particle interaction with the flame, and the droplet deposition and coating buildup.

In order to optimize the thermal spray process and improve the quality of the coating, several technological innovations are made in the torch gun. For DC plasma spray, the optimal design of torch nozzle conducted by Cao et al. [1997] improved the heat and momentum transfer to the injected particles in plasma jet. The use of ternary Ar-H<sub>2</sub>-He plasma-forming gas mixtures increases both the thermal conductivity of the plasma gas and its viscosity, thereby, improving the heat transfer and delaying the mixing of the surrounding air with the plasma gas, compared to a classical Ar-H<sub>2</sub> mixture [Janissson, 1999]. The phenomena of the piston flow induced by the arc root fluctuations, which is also related to anode erosion, was investigated and results showed that it enhances the entrainment of the dense ambient gas into the low density plasma jet [Huang, 1995].

In addition, non-conventional plasma torches are also developed and commercialized such as rotating torches, torches with two external anodes, water plasma torches, torches with axial injection, micro-plasma torches, torches with three cathodes such as TRIPLEX from Sultzer-Metco. Water plasma torches with a consumable graphite electrode and an external rotating anode are used to spray high quantities of oxides or metals [Dibble, 1996]. Moreau et al. [1995] reported that the use of torches with axial injection improves the heat transfer to particles. It is especially beneficial to the system with particles that are difficult to melt, or to particles larger than those used in conventional torches. Such torches allow the spraying of very dense oxide coatings. Yushchenko et al. [1997] reported that micro-plasma spraying torches with jet diameters between 2 and 4 μm and lengths between 30 and 50 μm were used to coat a restricted surface area or spray on narrow strips. Torches with three cathodes and a segmented anode [Zierhut, 1998] have been developed. The arc current is distributed between the three cathodes, so that erosion is less than that of a single cathode torch. The arc has a controlled length owing to the segmented anode, thereby resulting in very low voltage fluctuations.

In addition to the plasma torch, control of the powder injection also plays an important role on coating properties. A number of studies were conducted to investigate how powder chemical composition, particle size distribution and morphology, and injector size, shape, position and location affect the coating properties [Kubel, 1990]. Particle morphology [Wigren, 1996], which is related to the powder manufacturing techniques, plays an important role on pneumatic feeding. Research shows that the homogeneity of the particles [Kolman, 1994] is a key parameter for coating behavior, especially at high temperatures.

### 1.2.2 RF plasma spray

Plasma generation. The RF plasma is generated by receiving electromagnetic energy that is induced by the surrounding coils. As schematically shown in Fig. 1.3, the alternative electric current in the coil has a radio frequency, thus an oscillating magnetic field is produced. An electric field is also induced, which gives rise to the currents in the plasma, directing opposite to the primary current in the coil. The plasma temperature is raised up to a high degree by Joule heating effect. The plasma is electric conductive due to the gas ionization from the thermal collisions of the particles. The formation of the plasma is dependent on an adequate magnetic field strength and the pattern of the gas streams. The Lorentz force is another effect in RF induction plasma. Such force will stir the plasma gas and affect the flow and temperature distribution.

In order to prevent possible short-circuiting as well as meltdown, the plasma has to be insulated from the rest of the torch. Insulation is achieved by the concurrent flow of gases through the system. Usually, three gases flow through the system: the sheath gas, central gas, and carrier gas. The sheath gas is typically argon or nitrogen, which serves several purposes including maintaining the plasma, stabilizing the position of the plasma, and thermally isolating the plasma from the outer tube. Argon is commonly used for both the central gas and carrier gas. The purpose of the carrier gas is to inject the particles to the plasma.

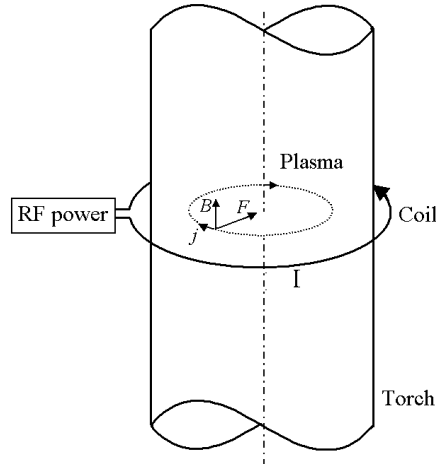


**Figure 1.3: Schematic of an inductively coupled RF discharge.**

RF plasma spray and synthesis. The RF induction plasma spray system was firstly introduced by Boulos et al. [1991]. It has evolved quickly from an interesting laboratory tool to an industrial source with wide applications in the material processing. Induction plasma can be applied to thin/thick film deposition, suspension plasma spray, ultra-fine powder production, powder densification and spheroidization, waste treatments, etc.

Powder densification and spheroidization is one of the simplest and most widely accepted applications of induction plasma technology [Margolies, 1998]. It consists of in-flight heating and melting of feed material in the form of sintered or crushed powders. The thus-formed molten spherical droplets are gradually cooled and completely solidified before reaching the bottom of the reactor chamber.

The ultra-fine powders are produced from the solid feedstock or liquid/vapor precursor. The product size depends on the quenching process, typically ranging from 20 to 100 nm. Such small-scale materials display unusual properties (chemical, physical, electrical, optical, mechanical, magnetic, etc.) as compared to their bulk states and therefore have received extensive research efforts [Lau, 1998; Welz, 2003].

Suspension Plasma Spraying is a new process used to synthesize functional materials. A suspension of fine powders is atomized by a pressurized gas and injected into the RF plasma. The plasma discharge vaporizes the carrier substance, e.g. the water, and agglomerates the small solid particles into partially or

totally melted droplets. The melted droplets are accelerated to hit the substrate and form the coating or alternatively, are solidified in-flight and collected into a vessel to produce powders. One of the major advantages of suspension plasma spraying over conventional techniques is its simplicity. Suspension plasma spraying is basically a one-step process incorporating atomization, drying, melting and solidification into approximately 10 milliseconds in-flight process under plasma conditions. The feeding of suspension has a number of potential benefits. For instance, the very fine particles can be protected against decomposition or evaporation in the plasma or against oxidation in the case of metals, owing to the presence of liquid film surrounding the particles. Also, the suspension can be arranged so that the chemical reaction between the liquid and particles occurs in the plasma, making it possible to synthesize advanced ceramics and composites.

Reactive synthesis from suspension induction plasma spray has been successfully applied to various intermetallic matrix or functional oxides. For example, the titanium aluminide matrix composites (TiN and AlN) are synthesized from the Ti (99.8 wt% purity), Al (99.7 wt% purity) and TiAl (99.4 wt% purity) particles sprayed on the stainless steel substrate using the RF Ar/N<sub>2</sub> plasma spraying [Tsunekawa, 2000]. Recent work in Stony Brook has been conducted on the RF plasma reactive synthesis and obtained successful direct deposition of YAG and YIG oxides from the liquid precursors, i.e., nanostructured YAG coatings synthesized from a liquid precursor of boehmite sol and aqueous yttrium nitrate [Devi, 2002].

*Modeling of RF Induction Plasma.* Numerical simulation is an excellent tool to investigate the complex induction plasma spray system. It can calculate the flow, temperature and species concentration fields, as well as the interaction between the particles and the plasma. Up to now, numerical simulations have been performed to study the induction plasma behavior, from 1-D, 2-D to 3-D [Bernardi, 2004]. Boulos and his colleagues have conducted numerous investigations for the heat and mass transfer in the coupled induction plasma spray system. Both the standard model and extended field model have been used to calculate the electromagnetic field. The effect of the spiral coil angle has also been considered to obtain a better understanding of the axial electric field induced by the axial component in the coil current [Xue, 2003]. They also studied the turbulence phenomenon [Ye, 1999] and the supersonic plasma jet system

[Selezneva, 2001]. Desilets, Bilodeau and Proulx have studied the reactive synthesis, the nucleation and growth process of ultra-fine powders in RF plasma spraying [1997]. Tanaka proposed a model for the non-equilibrium chemical reaction during the plasma generation [2002] and recently, Shigeta studied the RF induction plasma with seeded metal vapor, potassium [2004]. Most of these models focus on the electromagnetic field and the plasma field in the induction plasma spraying. Unfortunately, the particle behaviors are critical for the coating quality control but not considered in most of the literature study.

**Table 1.2: Summary of selected model and simulation results in RF plasma research**

Author & references	Model and simulation	Comments
Xue and Boulos [2001]	Model of the extended-field electromagnetic field generated by the RF coils.	Better than the standard model.
Shigeta [2004]	RF induction plasma with seeded metal vapor of potassium.	SIMPLE algorithm used.
Bernardi [2004]	Three-dimensional simulation of RF induction plasma.	
Xue [2003]	Improved two-dimensional model with considering the effect of the spiral coil angle.	
Tanaka [2002]	Model for the non-equilibrium chemical reaction.	For nitrogen plasma
Desilets [1997]	Study the reactive synthesis of ultra-fine powders in RF plasma spraying numerically.	W/ nucleation and growth of particles

### 1.2.3 Particle physics

The interaction of particles with the thermal spray jet is a critical factor determining the coating properties, which, to a large extent, depend on the particle temperature, velocity and melting status at the instant of impact on the substrate. Therefore, an accurate description of transport phenomena of particles is essential to the improvement and control of the coating process. Current status of the research about particle physics in thermal spray is briefly reviewed in the following.

Particle acceleration and heating. Heat and momentum transfer between a particle and a high temperature flow received much attention in the 1980s [Boulos, 1993]. Computational models developed so far have taken into account all special effects related to thermal spray conditions, e.g., steep temperature gradient, non-continuum effects, and vaporization.

Most models treat the particles in the flow as discrete Lagrangian entities that exchange mass, momentum, and energy with the gas [Lee, 1981; Wan, 1999]. Special characteristics of thermal plasma, such as steep temperature gradients in the boundary layer surrounding the particle, non-continuum effects (Knudsen effect), varying plasma properties, thermophoresis, turbulent dispersion, evaporation, etc. have also been studied [Chen and Pfender, 1983; Wan, 2001]. However, the understanding of particle behaviors in plasma jet is not complete, especially for particle phase change, evaporation and oxidation.

The description of powder injection with a stochastic distribution also remains as a problem. In the modeling of the plasma spray process, the conditions of particles injection in the flow govern the particle trajectory distribution and, therefore, their treatment. Thus, these conditions must be as realistic as possible and they depend on particle size, injection velocity and direction distribution at the injector exit.

Since the molten state of the particles when they impact on the substrate will affect the particle spreading and solidification, many efforts have been devoted to optimizing operating conditions to ensure complete melting of particles before impact on the substrate. He et al. [2001] investigated particle melting during HVOF thermal spraying using Inconel 625 powders. They concluded that the volume fraction of unmelted particles in the coatings was dependent on the proportion of powder within a specified size range, in their experiments, 30 to 50  $\mu\text{m}$ . Fauchais et al. [1992] investigated the behavior of particles in-flight. They demonstrated the surging and whipping of the plasma jet due to the arc-root fluctuations, which changes the mean trajectory of the particles and the engulfment process of the air entrainment. Prystay and Moreau et al. [2001] used an integrated optical monitoring system to measure the particle velocity and temperature and studied the correlation between particle temperature and velocity with the structure of plasma-sprayed zirconia coatings. They showed that the temperature of the sprayed particles has a significant effect on the coating properties than the velocity under the conditions they investigated.

*Particle evaporation.* Vaporization can be easily achieved for particles with relatively low-boiling temperature materials in a high temperature plasma jet. They, subsequently, introduce vapor into the environment and thus influence the heat, momentum and mass transfer of the particles.

Fiszdon [1979] is probably the first author who investigated the phase change of particles and the vapor diffusion in plasma spray. His model only considered evaporation after the particle surface temperature reaches boiling point. It was based on the assumption that the heat flux at the particle surface controls the evaporation rate, which is obviously oversimplified. Westhoff [1992] included the Langmuir evaporation and mass transfer of species between the particle and plasma jet. Vardelle [1997] noted that Langmuir equation could only account for the maximum flux of vaporization from a droplet surface at vacuum. The evaporation models that assumed the diffusion control through the thermal boundary around the particle under plasma conditions, were also studied by other researchers [Vardelle, 1997; Wan, 1999]. Droplet evaporation considered as a diffusion control process has been extensively studied in the area of combustion [Faeth, 1983]. Wan et al. [1999; 2001] applied the same concept to describe the evaporation of molten droplets. In addition, the evaporation can also be induced by chemical reaction, for example, by the oxidation of metal, molybdenum (Mo) particles under an atmospheric condition [Wan, 2002]. The effects of mass transfer on convective heat transfer were also studied [Chen and Pfender, 1982].

Experimental studies on particle evaporation are limited due to the technological difficulty. Most experiments were conducted to measure the particle size change. Li and Vardelle et al. [1996] measured the size distribution of iron particles before and after thermal treatments to estimate the total vaporized mass fraction. Their data showed a strong dependence of vaporization on initial particle size.

Particle oxidation. The plasma spraying of metals under atmospheric conditions inevitably leads to oxide formation. The oxygen content and oxide types are related to various parameters such as particle temperature and velocity, spray distance, feedstock composition, plasma gas type, and substrate temperature. Also, the high temperatures encountered in thermal spraying result in the formation of a wide variety of metastable oxide structures. The oxides within the particles upon impact will affect the coating properties significantly. Currently most applications of spray coating call for low oxide levels, since the coating performance will be degraded due to the brittleness and reduced corrosive resistance by the oxide within the coating. However, the general opinion that oxides deteriorate the coating properties may not be necessarily true [Volentik, 1997]. Rather it may lead to new application of forming coatings

with controlled proportions of metal and oxide phases. Therefore, it is desirable to understand the mechanism of oxidation and its effect on coating properties, and hence to control the amount, composition and distribution of oxides within the deposits.

Two stages of oxidation exist in thermal spray: in-flight oxidation and splat oxidation. During the first stage, particles interact with the entrained air, and strongly depend on the particle temperature and whether the molten or solid particle can react. The solidified deposit material interacts with a gaseous mixture consisting mainly of the ambient atmosphere. It is typical second stage of oxidation, which is characterized by rapid decrease of splat temperature. Hackett et al. [1994] discussed three possible sources of oxidation during plasma spray: i) the core of the flame, (ii) the end of the plume to the substrate and (iii) the time on the substrate exposed to hot gases until subsequently covered by another layer of splats. It was concluded that oxidation occurs primarily on the substrate. However, Vardelle et al. [1995] discussed that oxidation does not primarily occur at the substrates, it is rather from the in-flight part. Dobler [1996] investigated the WSP oxidation and concluded that the WSP may not be inherently oxidizing and thus oxidation primarily occurs during the particles in-flight from the end of the plume to the substrate.

The amount of oxide in the APS coating is significantly greater than that in the VPS deposits, and the shrouded deposits qualitatively have less oxide compared to unshrouded deposits [Dobler, 1996], since the inert gas shrouding of the plasma can reduce oxygen entrainment during spraying of metals.

Recently efforts have also been made to study the oxidation of in-flight particle and deposited splat experimentally, theoretically and numerically. Most of these papers observe the amount and distribution of oxide formed inside in-flight particles of different materials during APS process. However, there are a very limited number of publications in which attempts have been made to interpret the oxidation mechanism. It is still challenging to model the oxidation of metal droplets in thermal spray. Vardelle et al. [1995] presented an estimation of the oxidation of pure iron during plasma spraying, by assuming that the gas-phase diffusion as the rate-controlling process. A quasi-steady-state model of the iron particle oxidation during deposition was proposed by Smith et al. [1997] considering the diffusion of Fe through  $\text{FeO}_2$  scale

in the solid state as the rate-limiting step. Wan et al. [2001] developed a comprehensive oxidation model for covering broad temperature ranges during the particle flight and deposition. Their model considered oxidant diffusion around the particle surface or spat, oxidation on the surface, as well as oxygen diffusion in the molten molybdenum. The effects of particle size and other parameters, such as particle temperature and velocity, on oxidation and evaporation have not been discussed.

Experimental studies have been conducted on two stages of oxidation in thermal spray process [Espie, 1999; Neiser, 1998; Vardelle, 1995; Sobolev, 1999; Ahmed, 2001]. Espie et al. [1999] observed the amount and distribution of oxide formed iron particles during in-flight for atmospheric plasma spray, with oxide of more than 10 wt% of FeO in low carbon steel particles. They also showed that the convection within the molten droplet will ease the formation of internal oxides, and oxidation is then no longer controlled by diffusion. Fresh metal at the particle surface is continuously renewed while the formed oxide is entrained within the particle by the convective movement of the liquid. Neiser et al. [1998] found that for the particle with temperature below the melting point, oxide shells will be formed around the particle. They observed the low-carbon steel particles in HVOF with oxide shell mainly made of  $\text{Fe}_3\text{O}_4$  and not  $\text{Fe}_2\text{O}_3$ . Vardelle et al. [1995] studied the oxidation of metallic substrates during plasma spraying, which is an important phenomenon affecting the adhesion of plasma deposited coatings. In addition, Delplanque [1999] investigated in-service oxidation of as-sprayed deposits. Some information has been obtained on high temperature behavior of metal or alloy coatings.

**Table 1.3: Summary of selected model in particle-plasma interaction research**

Author & references	Model and simulation	Comments
Crowe [1977]	Particle-source-in-cell model of gas-droplet flow.	
Chen and Pfender [1982, 1983]	Momentum and heat transfer to a single particle exposed to thermal plasma.	
Wan [1999,2001,2002]	Model of in-flight particle evaporation and oxidation (molybdenum).	Consider evaporation controlled by vapor diffusion through boundary layer.
Vardelle [1995]	Present an estimation of the oxidation of pure iron during plasma spray.	Assume the gas-phase diffusion as controlling process.

Smith [1997]	Propose a quasi-steady state model of the iron particle oxidation during deposition.	Consider the diffusion of Fe through $\text{FeO}_2$ scale in the solid state as the rate-limiting step
--------------	--	--

**Table 1.4: Summary of selected experimental results in particle-plasma interaction research**

Author & references	Experiment	Comments
Li and Vardelle [1996]	Measure the size distribution of iron particles before and after plasma spray to compute the total vaporized mass.	Strong dependence of vaporization on particle size.
He [2001]	Particle melting using Inconel 625 powder.	In HVOF spray
Espie [1999]	Measure the amount and distribution of oxide formed within the in-flight iron particles for atmosphere plasma spray.	Show that the convection within the molten droplet will ease the formation of internal oxides.
Neiser et al. [1998]	They observed the low-carbon steel particles in HVOF with oxide shell mainly made of $\text{Fe}_3\text{O}_4$ and not $\text{Fe}_2\text{O}_3$ .	For the particle with temperature below the melting point, oxide shells will be formed around the particle.

### 1.3 Research objectives

This research is aimed at improving the understanding of the mass, momentum and heat transport phenomena in plasma spray processes. Two systems are to be studied: one is DC plasma spray operated in an atmospheric environment; the other is RF plasma spray in a low-pressure torch. Mathematical models will be built for the plasma jet in the Eulerian system, coupled with the in-flight particle physics in the Lagrangian system. For the DC plasma spray, a three-dimensional model is developed in order to examine the plasma jet and particle behaviors. In the study of RF plasma spray, a two-dimensional model is used coupled with the electromagnetic modeling. The parametric studies are also conducted, which investigates these two plasma spray processes with different operating conditions, giving rise to a more comprehensive understanding of the particle behaviors. Finally, the order-of-magnitude analysis leads to the derivation of two dimensionless parameters, melting index and oxidation index, to characterize the melting status and oxide content of in-flight particles.

3D simulation of DC plasma jet. Most numerical simulations for plasma spray were conducted in a 2-D computational domain; the plasma jet is assumed to be axisymmetric, and the effects of carrier gas and feedstock injection are neglected. However, the 3-D modeling is mandatory to study the perturbation of the plasma jet by the carrier gas. For this purpose, the previous 2-D code for plasma jet generation will be extended to three-dimensional configuration by introducing special treatments, such as source terms for carry gas injection and boundary conditions, to include the effects of carrier gas and particle injection on plasma jet.

The 3D features of plasma jet induced by the carrier gas jet and powder injections will be investigated, with the preliminary results shown in Chapter 5. It is expected that the understanding can be improved for plasma jet behavior, and more accurate prediction of particle acceleration, heating, melting and metal oxidation will be achieved using this 3D model.

2D simulation of RF plasma spray. RF induction plasma is a promising technique with novel applications in materials processing, *i.e.*, film deposition and synthesis. This technique draws extensive efforts in the laboratory research and industrial development due to its unique characteristics. However, the fundamental understanding of this process is not fully developed. A two-dimensional numerical model has been developed to investigate the induction electromagnetic (EM) field and the thermo-fluid field in a radio frequency inductively coupled plasma (RF-ICP). Various physical and chemical phenomena have been considered such as the induction heating, plasma generation, and the in-flight particle interaction with the plasma jet. This model has been applied to the induction plasma spray process operated in a vacuum chamber. The partially stabilized zirconia powder (PSZ) has been used as an example for the feedstock. The effects of power input, spray distance and powder injection position on the plasma and particle behaviors have also been investigated and discussed.

Parametric studies of particle behavior in plasma spray. The effects of operating conditions on single and multiple particles behavior for different materials will be investigated both in the three-dimensional DC plasma spray and in the two-dimensional RF induction spray system. The spray pattern of particles and

the average particle velocity and temperature along with their statistical distributions will be studied under different operating conditions.

*Melting index and oxidation index.* The melting and oxidation of the in-flight particles are very important to the splat formation and the coating quality. Melting index and oxidation index are derived to characterize the particle melting and oxidation behavior analytically. These two indices are correlated with the measurable particle parameters.

#### 1.4 Preview of the thesis

Chapter 2 and Chapter 3 present the modeling fundamentals of the plasma jet formation and particle-plasma interaction. In Chapter 2, the theories for the plasma jet are introduced, including the schemes of the chemical reactions, the Maxwell equations for the electromagnetic field, and the transport equations governing the DC plasma jet and the RF plasma jet. The modeling of the interaction between the particles and the plasma jet are mainly described in Chapter 3, as well as the stochastic model of the particle injection.

Chapter 4 presents the numerical schemes used to discretize the governing equations introduced in Chapter 2 and Chapter 3.

Chapter 5 investigates the DC plasma jet and the particles behaviors in 3-D geometry. The effects of operating conditions on the in-flight particles are also studied. Specific attention is directed to effects of carrier gas flow and particle load on 3-D plasma jet and the effects of carrier gas flow rate on the in-flight particles. In Chapter 6, the melting index and oxidation index are derived using a one-dimensional network analysis. These two parameters are validated by the simulation results and the experiments. Chapter 7 studies the RF plasma torch in 2-D geometry. The effects of power input, spray distance and powder injection position on the plasma and particle behaviors are investigated and discussed.

Chapter 8 summarizes the work reported in this thesis and the recommendations for the future work are also addressed.

## **Chapter 2      Mathematical Model of Plasma Flame**

The plasma spray process is divided into three stages: plasma generation, particle-plasma interaction during in-flight, and coating formation on substrate. This chapter explains the mathematical models for the generation of the DC plasma and the RF plasma. The modeling of particle-plasma interaction will be addressed in the next chapter.

### **2.1 DC plasma**

The modeling for the DC plasma flame should consider various physical and chemical phenomena. The plasma source is generated by the direct current arc, and governed by the magneto-hydrodynamics of the gas flow between the two electrodes. The plasma jet is formed after the plasma source is expelled out of the plasma gun. At the fringes of the plasma jet downstream, large scale eddies are developed due to the shear stress, which leads to the transition to the unstable turbulent flow. The mass, momentum and energy transports of the plasma jet are greatly influenced by the turbulence. Chemical reactions are also present in this high-temperature multi-species gas, making the modeling more complex. All these phenomena will be detailed in this section.

#### **2.1.1 Plasma source**

The modeling of DC arc formation is reported in many works during the last two decades, which include the arc formation in the electrode region as well as the transition from the plasma to the electrode surface. Heberlein [1999] summarized these works and showed that strong deviations from kinetic equilibrium prevail in these regions, which make the phenomena of arc formation very complex. One of the challenges is the description of the phenomena at the anode wall. This description has to be dynamic and three-dimensional and includes numerous parameters affecting the arc-anode interaction.

Currently, most models of arc formation have been restricted to two-dimensional situations with the assumptions of Local thermodynamic equilibrium (LTE) and electrical neutrality. The classical equations are used: mass, momentum, energy and current density conservation, Ohm's law and Maxwell's equations for electric potential, the magnetic field being calculated from the current density

with the help of the Ampere's theorem. Since these models for arc formation are usually based on oversimplified assumptions for the anode and cathode phenomena, it is not surprising that the agreement between measurements and calculation is not very good [Scott, 1989]. 3-D transient modeling of the arc column has been reported recently [Vardelle, 2003] but without the consideration of the electrode regions.

Since the modeling of arc formation is complex and the result is not reliable, most simulations of plasma jet start from the results of calculating temperature and velocity distributions at the nozzle exit matching with the plasma gas flow rate and enthalpy:

$$v(r,0) = V_{cl} \left[ 1 - (r/R_i)^m \right] \quad (2.1)$$

$$T(r,0) = (T_{cl} - T_w) \left[ 1 - (r/R_i)^n \right] + T_w \quad (2.2)$$

where  $R_i$  is the torch nozzle exit radius. The parameter  $V_{cl}$ , m,  $T_{cl}$  and n are selected to match the known flow rate of cold plasma gas and the power supplied into the plasma torch as closely as possible. In our study, we use the expression from Chang [1993], which has already been validated with experiments [Fincke, 1994]. For example, for the flow rate (Ar-H<sub>2</sub> plasma gas) of 40/7 cm<sup>3</sup>/s and the net power of 19.52 kW, the values of  $V_{cl}$ , m,  $T_{cl}$  and n are 2560.23 m/s, 1.2, 12988 K and 6, respectively.

### 2.1.2 Plasma jet

The governing equations of the DC plasma jet consists of several parts: continuity, momentum and thermal energy equations for the multi-component fluid mixture, and species equations for each component of the mixture taking into account the mixing with the surrounding atmosphere, state relations for an ideal gas mixture with temperature-dependent specific heat, enthalpy and transport properties, and so on.

*Continuity equation:*

$$\frac{\partial \rho}{\partial t} + \nabla \cdot (\rho \bar{u}) = 0 \quad (2.3)$$

*Species equations:*

$$\frac{\partial \rho_i}{\partial t} + \nabla \cdot (\rho_i \vec{u}) = -\nabla \cdot \vec{J}_i + \dot{\rho}_i^c \quad (2.4)$$

where  $\nabla$  is the vector differential operator in cylindrical coordinate,  $J_i$  is the diffusion mass flux, the subscript  $i$  represents different species, and  $\dot{\rho}_i^c$  is the rate of change  $\dot{\rho}_i$  due to chemical reaction. The diffusion mass flux of species  $j$ ,  $J_j$ , is determined by a self-consistent effective binary diffusion approximation [Ramshaw, 1991], and given by:

$$J_j = -c M_j D_j \nabla \left( \frac{\rho_j}{M_j c} \right) + \left( \frac{\rho_j c}{\rho} \right) \sum_i M_i D_i \nabla \left( \frac{\rho_i}{M_i c} \right) \quad (2.5)$$

*Momentum equation:*

$$\frac{\partial(\rho \vec{u})}{\partial t} + \nabla \cdot (\rho \vec{u} \vec{u}) = -\nabla \left( p + \frac{2}{3} \rho k \right) + \nabla \cdot \vec{\sigma} + F \quad (2.6)$$

where,  $F$  represents the momentum source or sink due to injected particles,  $k$  is the turbulent kinetic energy per unit mass,  $\vec{\sigma}$  is the viscous stress matrix. The viscous stress is given by:

$$\vec{\sigma} = (\mu + \mu_t) [\nabla \vec{u} + (\nabla \vec{u})^T] + (\lambda + \lambda_t) \nabla \cdot \vec{u} I \quad (2.7)$$

where  $\mu$  is the viscosity,  $\mu_t$  is the turbulence viscosity, and  $I$  is the unit matrix:

$$\lambda = -2\mu/3 \quad (2.8)$$

$$\lambda_t = -2\mu_t/3 \quad (2.9)$$

*Thermal energy equation:*

$$\frac{\partial(\rho e)}{\partial t} + \nabla \cdot (\rho e \vec{u}) = -p \nabla \cdot \vec{u} - \nabla \cdot \vec{q} + \rho \varepsilon + \dot{Q}_c - \dot{Q}_R + \dot{Q}_p \quad (2.10)$$

where  $\vec{q}$  is the heat flux vector,  $\varepsilon$  is the viscous dissipation rate,  $\dot{Q}_c$  is the rate of change of  $\rho e$  due to chemical reactions,  $\dot{Q}_R$  is the heat loss rate due to radiation, and  $\dot{Q}_p$  is the heat source or sink due to injected particles.

The heat flux vector,  $\vec{q}$ , contains contributions from both pure heat conduction and species diffusion, which is given by:

$$\vec{q} = -K\nabla T + \sum_j h_j \vec{J}_j . \quad (2.11)$$

*State relations:* The average density, gas temperature and gas pressure are determined from the state equations as follows:

$$\rho = \sum_s \rho_i \quad \text{or} \quad C = \sum_s \frac{\rho_i}{M_i} \quad (2.12)$$

$$\rho e = \sum \rho_i e_i(T) \quad (2.13)$$

$$P = R_g T \sum \frac{\rho_i}{M_i} = R_g T C \quad (2.14)$$

### 2.1.3 Chemical reactions

The ionization, dissociation, recombination, and other chemical reactions take place in the plasma jet and can be treated using a general kinetic algorithm. A reduced set of chemical reactions for the argon-hydrogen plasma has been listed in Appendix A.

A partial equilibrium is assumed in which fast reactions are considered to be in equilibrium while slower ones proceed kinetically [Ramshaw, 1995]. The chemical reaction  $S$  can be symbolized by:



where  $X_i$  represents species  $i$ , and  $b_{is}$  and  $a_{is}$  are stoichiometric coefficients for reaction  $S$ . The mole density  $\rho_i^c$  is described by:

$$\rho_i^c = M_i \sum_s (b_{is} - a_{is}) \omega_s \quad (2.16)$$

where  $M_i$  is the molecular weight for  $i$  species.

1. Kinetic reactions: The kinetic chemical reaction  $s$  proceeds at a rate of  $\omega_s$  given by:

$$\omega_s = k_{fs} \prod_i (\rho_i / W_i)^{a'_{is}} - k_{bs} \prod_i (\rho_i / W_i)^{b'_{is}} \quad (2.17)$$

where reaction orders  $a'_{is}$  and  $b'_{is}$  are not necessarily equal to  $a_{is}$  and  $b_{is}$ , so that empirical reaction orders can be used. The coefficients  $k_{fs}$  and  $k_{bs}$  are determined by Arrhenius equation:

$$k_{fs} = A_{fs} \exp(-E_{fs}/T) \quad (2.18)$$

$$k_{bs} = A_{bs} \exp(-E_{bs}/T) \quad (2.19)$$

2. Equilibrium reactions: The progress rate for chemical reaction is calculated by an implicit scheme, and one kind of solution is using the equilibrium constant:

$$\prod_i (\rho_i/M_i)^{b_{is}-a_{is}} = K_s(T) \quad (2.20)$$

where  $K_s$  can be determined for every chemical reaction in such fashion:

$$K_p = B_p T^{n_p} \exp(Q_{k,ref}/RT) \quad (2.21)$$

$$\text{where } B_p = \exp\left(\sum_i (b_{is} - a_{is})\pi_{Ai}\right), \quad n_p = \sum_i (b_{is} - a_{is})\pi_{Bi} \quad \text{and} \quad Q_{k,ref} = \sum_i -(b_{is} - a_{is})H_{i,ref}$$

#### 2.1.4 Turbulence model

Large velocity difference between the plasma jet and its surrounding atmosphere results in a large-scale engulfment of the outside gas. Turbulence influences the fluid dynamics of plasma jet significantly, including mixing and entrainments. The most commonly used model in simulating plasma jet is the  $k - \varepsilon$  model, if necessary, with corrections to account for low Reynolds number.

For varying density flows in the plasma jet, the mass-weight decomposition and averaging suggested by Favre [1969] are preferred. In the Favre averaging procedure, the value of a conservation scalar quantity or velocity at a point can be considered as a sum of the mean value (time averaged) and fluctuating components, as for velocity:

$$u_i = \tilde{u}_i + u'_i \quad \text{where} \quad \tilde{u}_i = \frac{1}{\bar{\rho}} \lim_{\tau \rightarrow \infty} \frac{1}{\tau} \int_{t_0}^{t_0+\tau} \rho u_i dt \quad . \quad (2.22)$$

Substituting this equation into the momentum equation and taking the average over the equation yields the momentum equation of mean velocity in the tensor form as:

$$\frac{\partial R\bar{\rho}\tilde{u}_i}{\partial t} + \frac{\partial R\bar{\rho}\tilde{u}_i\tilde{u}_j}{\partial x_j} = -R\frac{\partial p}{\partial x_i} + \frac{\partial}{\partial x_j}[R\mu S_{ij}] + (-\mu S_{0,ij})\frac{\partial R}{\partial x_j} + RF_i + R\frac{\partial}{\partial x_j}\left(-\overline{\rho u'_i u'_j}\right). \quad (2.23)$$

This equation of time-averaged velocity has the same form as the fundamental momentum balance equation and only one additional term is introduced by turbulence through the Reynolds stress,  $\overline{\rho u'_i u'_j}$ .

Note that  $\overline{\rho u'_i u'_j}$  is a symmetric second order tensor and hence has six components. The main task of turbulence model is to provide the expressions or closure models of these correlations with the mean flow quantities.

The  $k - \varepsilon$  model is an eddy-viscosity model in which the Reynolds stresses are assumed to be proportional to the mean velocity gradients, with the constant of proportionality being the negative of the turbulence viscosity,  $\mu_t$ . With this assumption, known as Boussinesq hypothesis, provides the following expressions of the Reynolds stresses:

$$\overline{\rho u'_i u'_j} = \rho \frac{2}{3} k \delta_{ij} - \mu_t S_{ij} \quad (2.24)$$

where  $k$  is the turbulent kinetic energy.

This expression for Reynolds stresses is analogous to that describing the shear stresses in laminar flow with the turbulence viscosity  $\mu_t$  plays the same role as the molecular viscosity  $\mu$ . Therefore, the form of Favre-averaged momentum equations remain identical to the form of the laminar momentum conservation equation if  $\mu$  is replaced by the effective viscosity  $\mu_{eff}$ :

$$\mu_{eff} = \mu_t + \mu \quad (2.25)$$

Similarly, the form of Favre-averaged thermal energy can be obtained from the fundamental energy conservation equation by replacing thermal conductivity  $K$  with  $K_{eff}$ :

$$K_{eff} = K + K_t = K + \frac{C_p \mu_t}{Pr_t}. \quad (2.26)$$

Selection of different closure models for the turbulent equations, with regards to evaluating the turbulent transport properties, leads to several turbulence models such as zero-equation models, one-equation models, two-equation models, and Reynolds stress-equation models.

These models are classified according to the numbers of turbulent quantities that appear as dependent variables of differential equations. Turbulence viscosity is obtained by assuming that it is proportional to the product of a turbulent velocity scale and a length scale. The  $k - \varepsilon$  model is one kind of two-equation models, in which the velocity scale and length scale are obtained by two parameters: the turbulent kinetic energy,  $k$ , and the dissipation rate of  $k$ ,  $\varepsilon$ . The velocity scale is taken to be  $\sqrt{k}$ , and the length scale is taken to be  $\sqrt{k^3}/\varepsilon$ . Hence, turbulence viscosity  $\mu_t$  is given by:

$$\mu_t = \rho C_\mu \frac{k^2}{\varepsilon} \quad (2.27)$$

where  $C_\mu$  is an empirically constant that is usually set to be the value of 0.09.

The values of  $k$  and  $\varepsilon$  required in this equation are obtained by solving the following conservation equations in cylindrical coordinate:

$$\frac{\partial(\rho k)}{\partial t} + \nabla \cdot (\rho k \vec{u}) = -\frac{2}{3} \rho k \nabla \cdot \vec{u} + \nabla \cdot [(\mu + \mu_t) \nabla k] + \Phi - \rho \varepsilon + \dot{W} \quad (2.28)$$

$$\frac{\partial(\rho \varepsilon)}{\partial t} + \nabla \cdot (\rho \varepsilon \vec{u}) = \left( c_3 - \frac{2}{3} c_1 \right) \rho \varepsilon \nabla \cdot \vec{u} + \nabla \cdot \left[ \left( \mu + \frac{\mu_t}{c_4} \right) \nabla \varepsilon \right] + \frac{\varepsilon}{k} (c_1 \Phi - c_2 \rho \varepsilon + c_s \dot{W}) \quad (2.29)$$

Where  $\dot{W}$  is the source or sink term due to the interaction of particles with plasma gas. The coefficients is  $C_1=1.44$ ,  $C_2=1.92$ ,  $C_3=-1.0$ ,  $C_4=1.3$ ,  $C_s=1.5$ .

## 2.1.5 Boundary conditions

**Boundary conditions at the nozzle inlet of inflow.** Mass fractions of argon and hydrogen gas are given, and the temperature and axial velocity are estimated from:  $\tilde{v}(r,0) = V_{cl} [1 - (r/R_i)^n]$  and  $\tilde{T}(r,0) = (T_{cl} - T_w) [1 - (r/R_i)^n] + T_w$  where and the parameter  $V_{cl}$ , m,  $T_{cl}$  m and n are selected to match the known flow rate and the power supplied to the plasma gun;

**Boundary conditions at the torch wall.** The temperature is estimated from  $\tilde{T}(r,0) = 700 - 400 \ln(r/R_{in})/\ln(R_{out}/R_{in})$ , and the velocity components in r and y directions are zero, and  $\partial\phi/\partial y = 0$  is applied to  $\phi$ , representing the temperature and energy;

**Boundary conditions at the open boundaries.** The values of temperature and pressure are assigned the same as that in ambient for inflow, while  $\partial\tilde{\phi}/\partial y = 0$  for outflow. For example:

In the original LAVA code, the boundary conditions at the axis of the plasma jet, where  $x=0$ , are assigned in such fashion:  $u=0$ ,  $w = 0$ , and  $\partial v/\partial x = 0$ . This is only true for a single plasma jet. In the present of a side powder injection, the plasma jet no longer behaves symmetrical about the axis as the result of the interaction between the side jet, as well as the multiple particles injected, and the plasma jet. Therefore, the radial velocity,  $u$ , is not zero any more. However, the circular velocity should be symmetrical about a plane formed by the centerline of the plasma jet and the side jet. Thus the above boundary conditions at the centerline are not applicable.

**Boundary conditions at the symmetric axis ( $r=0$ ).** The values of each parameter,  $\phi$ , is determined according to the immediate neighborhood point in such format,

$$\phi|_{r=0} = \left( \sum_{i=1}^N \phi_i \right) / N(\phi = u, v, T), \quad \text{and} \quad w = 0 \quad (2.30)$$

where  $\phi_i$  ( $i = 1, 2, \dots, N$ ) are the values of  $\phi$  at locations with the distance  $\Delta r$  from the centerline. The specification of the boundary conditions for all other scalar parameters is the same as that for temperature.

**Boundary conditions at the circular direction, Z.** The periodic boundary condition is used:

$$\phi(x, y, 2\pi) = \phi(x, y, 0). \quad (2.31)$$

**Source terms of carrier gas and injected particles.** The source terms of carrier gas is added in the governing equations of species, momentum and energy, at the cells of the injector resided. The size of the injector is very small with the diameter of 1.8 mm, and its effect on the plasma jet is negligible. Instead of 3-D particle in a 2-D plasma jet, the model of 3-D particle in the 3-D cylindrical coordinate of a plasma

jet is incorporated into the code to take into account of full interaction between particles and the plasma jet.

The calculations are initialized from the cold air and then mixed with the incoming jet until the steady state is reached. The steady state solution is expected to be unique and independent of the initial conditions.

## 2.2 RF Plasma

Different from the DC plasma, the RF plasma is sustained by receiving the electromagnetic energy from the induction heating system. The electromagnetic field interacts simultaneously with the thermo-fluid field, which characterize the RF plasma. Therefore, the mathematical modeling should consider these two parts, *i.e.*, the Maxwell equations for the electromagnetic field and the transport equations for the thermo-fluid field, respectively.

### 2.2.1 Assumptions

This mathematical model is based on the following assumptions:

- (a) The flow is steady, laminar and axisymmetric.
- (b) Electromagnetic field is quasi-steady and axisymmetric. Axial component of the coil current is negligible.
- (c) Joule heating is generated by the eddy currents.
- (d) The viscous dissipation and the pressure work in the energy equation are negligible.
- (e) Local thermodynamic equilibrium and optically thin plasma are assumed.

### 2.2.2 Electromagnetic field

The modeling of electromagnetic field is based on the Maxwell equations, which can be expressed as follows,

$$\nabla \cdot \vec{H} = 0 \quad (2.32)$$

$$\nabla \cdot \vec{E} = 0 \quad (2.33)$$

$$\nabla \times \vec{H} = \vec{J} \quad (2.34)$$

$$\nabla \times \vec{E} = -\mu_0 \frac{\partial \vec{H}}{\partial t} \quad (2.35)$$

By introducing the magnetic vector potential  $\mathbf{A}$  that only has the tangential component for this case,  $(\theta, A_\theta)$ , we can rewrite the Maxwell equations (2.32-2.35) as such:

$$\left( \frac{1}{r} \frac{\partial}{\partial r} \left( r \frac{\partial}{\partial r} \right) + \frac{\partial^2}{\partial x^2} - \frac{1}{r^2} \right) A_\theta = -\mu_0 (J_{coil} + J_{ind}) \quad (2.36)$$

where  $J_{coil}$  is the current in the coil, and  $J_{ind}$  is the induced current in the plasma, which can be calculated from Ohms law:

$$J_{ind} = \sigma E = -i\sigma\omega A_\theta. \quad (2.37)$$

Once  $A_\theta$  is obtained, the electromagnetic field can be obtained from the following relations:

$$E_\theta = -i\omega A_\theta, \quad (2.38)$$

$$\mu_0 H_x = \frac{1}{r} \frac{\partial (r A_\theta)}{\partial r}, \quad (2.39)$$

$$\mu_0 H_r = -\frac{\partial A_\theta}{\partial x}. \quad (2.40)$$

The Lorentz forces and the Joule heating are expressed by:

$$F_r = \frac{1}{2} \mu_0 \sigma \operatorname{Re}(E_\theta \bar{H}_x) \quad (2.41)$$

$$F_x = -\frac{1}{2} \mu_0 \sigma \operatorname{Re}(E_\theta \bar{H}_r) \quad (2.42)$$

$$Q_J = \frac{1}{2} \sigma E_\theta \bar{E}_\theta \quad (2.43)$$

### 2.2.3 Transport model

The transport model of the RF plasma jet consists of several parts: continuity, momentum, thermal energy equations for the multi-component fluid mixture, and species equations for each component of the mixture.

Continuity:

$$\frac{\partial}{\partial x}(\rho u) + \frac{1}{r} \frac{\partial}{\partial r}(r \rho v) = 0 \quad . \quad (2.44)$$

Momentum:  $\frac{\partial}{\partial x}(\rho uu) + \frac{1}{r} \frac{\partial}{\partial r}(r \rho uv) = \frac{\partial}{\partial x}\left(\mu \frac{\partial u}{\partial x}\right) + \frac{1}{r} \frac{\partial}{\partial r}\left(r \mu \frac{\partial u}{\partial r}\right) + \left[ -\frac{\partial p}{\partial x} + \frac{\partial}{\partial x}\left(\mu \frac{\partial u}{\partial x}\right) + \frac{1}{r} \frac{\partial}{\partial r}(r \mu \frac{\partial v}{\partial x}) - \frac{2}{3} \mu \nabla \cdot \bar{\nabla} + F_x \right], \quad (2.45)$

$$\frac{\partial}{\partial x}(\rho uv) + \frac{1}{r} \frac{\partial}{\partial r}(r \rho vv) = \frac{\partial}{\partial x}\left(\mu \frac{\partial v}{\partial x}\right) + \frac{1}{r} \frac{\partial}{\partial r}\left(r \mu \frac{\partial v}{\partial r}\right) + \left[ -\frac{\partial p}{\partial r} + \frac{\partial}{\partial x}\left(\mu \frac{\partial u}{\partial r}\right) + \frac{1}{r} \frac{\partial}{\partial r}(r \mu \frac{\partial v}{\partial r}) - \frac{2}{3} \mu \nabla \cdot \bar{\nabla} - \mu \frac{2v}{r^2} + \rho \frac{w^2}{r} + F_r \right], \quad (2.46)$$

$$\frac{\partial}{\partial x}(\rho uw) + \frac{1}{r} \frac{\partial}{\partial r}(r \rho vw) = \frac{\partial}{\partial x}\left(\mu \frac{\partial w}{\partial x}\right) + \frac{1}{r} \frac{\partial}{\partial r}\left(r \mu \frac{\partial w}{\partial r}\right) + \left[ -\frac{w}{r^2} \frac{\partial}{\partial r}(r \mu) - \rho \frac{vw}{r} \right] \quad . \quad (2.47)$$

Energy:  $\frac{\partial}{\partial x}(\rho uh) + \frac{1}{r} \frac{\partial}{\partial r}(r \rho vh) = \frac{\partial}{\partial x}\left(\frac{k}{C_p} \frac{\partial h}{\partial x}\right) + \frac{1}{r} \frac{\partial}{\partial r}\left(r \frac{k}{C_p} \frac{\partial h}{\partial r}\right) + [Q_J - Q_{rad}] \quad . \quad (2.48)$

Species:  $\frac{\partial}{\partial x}(\rho u \rho_i) + \frac{1}{r} \frac{\partial}{\partial r}(r \rho v \rho_i) = \frac{\partial}{\partial x}\left(D_i \frac{\partial \rho_i}{\partial x}\right) + \frac{1}{r} \frac{\partial}{\partial r}\left(D_i \frac{\partial \rho_i}{\partial r}\right) + \dot{\rho}_{i,c} \quad . \quad (2.49)$

In Eq. (2.48),  $h$  stands for the enthalpy of the mixture, with unit of J/kg. In Eq. (2.49),  $i$  indicates the different species. For the current study with argon plasma, the species include Ar and Ar<sup>+</sup>, and an equilibrium reaction algorithm for the argon ionization and recombination is used [Ramshaw, 1995]. The details of this chemical reaction scheme have been stated in Section 2.1.3.

#### **2.2.4 Boundary conditions**

For the boundary condition of the electromagnetic field,  $A_\theta = 0$  is applied at  $r \rightarrow \infty$ . For the flow, the non-slip condition and thermal conduction are considered at the inner torch wall. The outer side of the torch wall is cooled by the water-cooling system and the temperature is fixed at 300 K. The inlet temperature of the gas and particles are also set as 300 K.

## Chapter 3      Interaction Between Particles and Plasma flame

This chapter presents the mathematical models for the particle physical and chemical phenomena. Computational particles are created at the point of injection and tracked throughout their flights. The solution of the plasma gas in Chapter 2 provides the information on the conditions external to the particles. The injected particles are treated in a Lagrangian coordinate. The effects of the particles feeding rate on the plasma flame are also taken into consideration.

### 3.1 Particle models

When the particles fly through the plasma flame, the mass, momentum and energy transfer from the flame will dramatically change the particle properties. These transport phenomena include particle acceleration, heating and melting, evaporation and the metal particle oxidation, etc.

#### 3.1.1 Acceleration and heating

The Lagrangian approach is used to trace the in-flight particles individually. Particle acceleration and heating are tracked after injection, by considering the drag force by plasma flame and the heat transport on the particle surface. For heat transfer, we have to consider some effects specific to thermal plasma environment. The main effects are due to the high temperature gradient prevailing in the boundary layer surrounding the particles, varying plasma properties, non-continuum conditions, thermophoresis, turbulent dispersion, evaporation and possible chemical reactions on the particle surface.

Particle acceleration model. Driving forces on a particle immersed into a plasma jet include the viscous drag, the pressure gradient and gravitational force. The drag force is the only prominent one that affects the particle momentum transfer significantly for the particle size of smaller than 100  $\mu\text{m}$  in plasma jet.

The momentum transfer between the particle and plasma jet can be described by:

$$F_p = m_p \frac{d\vec{V}_p}{dt}, \quad (3.1)$$

$$\frac{d\vec{V}_p}{dt} = \frac{3}{8} \frac{\bar{\rho}}{\rho_p} \frac{C_D}{r_p} \left| \tilde{\vec{V}} + \vec{V}' - \vec{V}_p \right| \left( \tilde{\vec{V}} + \vec{V}' - \vec{V}_p \right), \quad (3.2)$$

where  $\vec{V}'$  is the turbulence velocity fluctuation. The coefficient  $C_D$  for the drag force can be expressed as

[Lee 1981; Chen and Pfender 1983,]:

$$C_D = \frac{24}{Re_p} + \frac{6}{1 + \sqrt{Re_p}} + 0.4, \quad \text{for } Re_p < 100 \quad (3.3)$$

Or in some work, the drag coefficient is:

$$C_D = \begin{cases} \frac{24}{Re_p} & \text{for } Re_p < 1 \\ \frac{24}{Re_p} (1 + 0.15 Re_p^{0.687}) & \text{for } 1 < Re_p < 10^3 \\ 0.44 & \text{for } Re_p > 10^3 \end{cases} . \quad (3.4)$$

Reynolds number is defined as:

$$Re_p = \frac{\rho_f D_p |\tilde{\vec{V}} + \vec{V}' - \vec{V}_p|}{\mu_f} \quad (3.5)$$

where  $D_p$  is particle diameter,  $\rho_f$  and  $\mu_f$  are the mean density and viscosity of gas phase around the particle, respectively.

Lumped heat capacity model. If the particle temperature can be assumed as uniform, the energy conservation equation can be expressed as:

$$m_p C_p \frac{dT_p}{dt} = \pi D_p^2 \dot{q} \quad (\text{for } T_p \neq T_m) \quad (3.6)$$

$$m_p L_m \frac{d\chi_p}{dt} = \pi D_p^2 \dot{q} \quad (\text{for } T_p = T_m) \quad (3.7)$$

where  $\chi_p$  is the melt fraction of the particle, and  $\dot{q}$  is the heat flux at the particle surface.

One-dimensional model with heat conduction. When the Biot number related to particles is higher than 0.01 for ceramic material and large particles, the heat transfer in the particle has to be taken into account as the temperature gradient within the particles can be large. Therefore, a one-dimensional model for particle heating and melting is used in which a spherical shape of the particle is assumed and internal convection within the molten part of the particle is neglected. Figure 3.1 shows the geometry and the heat transfer between the particle and flame environment.

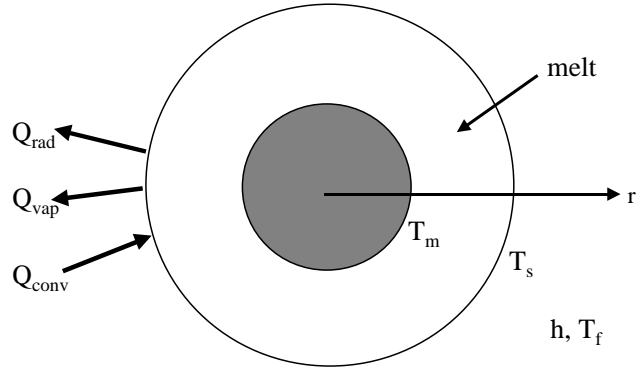


**Figure 3.1: Schematic of particle heat transfer.**

The temperature distribution inside the particle is described by conduction as follows,

$$\rho_p C_p \frac{\partial T_p}{\partial r} = \frac{1}{r^2} \frac{\partial}{\partial r} \left( K_p r^2 \frac{\partial T_p}{\partial r} \right), \quad (3.8)$$

where the subscript  $p$  represents the particle and the properties  $\rho_p$ ,  $C_p$ , and  $K_p$  are taken as local values.

The boundary conditions for a particle with melting interfaces are given below,

$$\left. \frac{\partial T_p}{\partial r} \right|_{r=0} = 0, \quad (3.9)$$

$$\left. \left( K_p \frac{\partial T_p}{\partial r} \right) \right|_{r=r_m^-} - \left. \left( K_p \frac{\partial T_p}{\partial r} \right) \right|_{r=r_m^+} = L_m \rho_p \frac{dr_m}{dt}, \quad (3.10)$$

$$4\pi r_p^2 \left. \left( K_p \frac{\partial T_p}{\partial r} \right) \right|_{r=r_p} = \dot{q}. \quad (3.11)$$

If resolidification occurs, an additional constraint has to be applied to the resolidification interface,

$$\left( K_p \frac{\partial T_p}{\partial r} \right)_{r=r_s^+} - \left( K_p \frac{\partial T_p}{\partial r} \right)_{r=r_s^-} = L_m \rho_p \frac{dr_s}{dt}. \quad (3.12)$$

The melting condition can be either considered as equilibrium or non-equilibrium. If an equilibrium melting or resolidification happens, the interface temperature is assumed to be melting temperature:

$$T_p \Big|_{r=r_m, r_s} = T_m \quad (3.13)$$

Otherwise for non-equilibrium melting, there is superheating and the interface movement is related to interface temperature,  $T_i$ , by:

$$\frac{dr_m}{dt} = \mu_k (T_m - T_i) \quad (3.14)$$

where  $\mu_k$  is the linear kinetic coefficient, for example, the values of  $\mu_k$  for molybdenum and zirconia are 0.23 and 0.01 m/s-K according to Wang [1996]. For the non-equilibrium solidification the consideration is similar to melting.

In the above energy conservation models, the heat flux at the particle surface can be expressed as following,

$$\dot{q} = \dot{Q}_{conv} - \dot{Q}_{vap} - \dot{Q}_{rad} \quad (3.15)$$

$$\dot{Q}_{conv} = 4\pi r_p^2 h (\tilde{T}_f - T_s) \quad (3.16)$$

$$\dot{Q}_{vap} = \dot{m}_v L_v \quad (3.17)$$

$$\dot{Q}_{rad} = 4\pi r_p^2 \epsilon_p \sigma (T_s^4 - \tilde{T}_\infty^4) \quad (3.18)$$

if considering heat transfer by convection, evaporation and radiation. Where the heat transfer coefficients is calculated from:

$$h = \frac{k_f N u}{2r_p} \quad (3.19)$$

$$N u = 2.0 + 0.6 R e_p^{1/2} P r^{1/3} \quad (3.20)$$

and  $\tilde{T}_f$  is the film temperature defined as the average value of gas temperature at the cell where the particle is located and at the immediate vicinity by the particle surface:

$$\tilde{T}_f = (T_c + T_w)/2. \quad (3.21)$$

Specific effects. Considering the effects specific to thermal plasma environment, for example, the high temperature gradient, strongly varying plasma properties, non-continuum conditions, evaporation and so on, the heating and acceleration of particles can be modified as:

$$C_{D, eff} = C_D f_{prop}^{-0.45} f_{Kn}^{0.45} \quad (3.22)$$

$$Nu_{eff} = Nu \left( \frac{C_{p,c}}{C_{p,w}} \right)^{0.38} (f_{prop})^{0.6} f_{Kn} f_v \quad (3.23)$$

where  $C_{p,c}$  and  $C_{p,w}$  are specific heat capacity of plasma gas at the cell where the particle is located and the vicinity of the particle surface.  $f_{prop}$  and  $f_{Kn}$  are the factors representing the effects of variable plasma properties and non-continuum, respectively.

$$f_{prop} = \frac{\rho_c \mu_c}{\rho_w \mu_w} \quad (3.24)$$

$$f_{Kn} = \left[ 1 + \left( \frac{2-a}{a} \right) \left( \frac{\gamma_w}{1+\gamma_w} \right) \frac{4}{Pr_w} Kn \right] \quad (3.25)$$

where  $a$  is the thermal accommodation coefficient with a recommended value of 0.8 [Chen and Pfender, 1983].  $\gamma_w$  and  $Pr_w$  are the specific heat ratio and the Prandtl number of the plasma gas evaluated at the surface temperature.  $Kn$  is the Knudsen number based on the effective mean free path and can be obtained from an approximate expression:

$$Kn = \frac{Pr_w}{\rho_w v_w r_p} \frac{k_f}{C_{p,f}} \quad (3.26)$$

where  $v_w$  is the mean molecular speed that is dependent on the average molecular weight  $W$  of the gas mixture as well as on the gas temperature near the particle surface  $T_w$ :

$$v_w = \left( \frac{8RT_w}{\pi W} \right)^{1/2} \quad (3.27)$$

$f_v$  accounts for the effect of mass transfer due to particle evaporation. Heat transfer and phase change within the particle and mass transfer from its surface can be calculated based on this information.

$$f_v = \frac{\dot{m}_v c_{p,f} / 2\pi r_p K_f}{\exp\{\dot{m}_v c_{p,f} / 2\pi r_p K_f\} - 1} \quad (3.28)$$

### 3.1.2 Evaporation

There are different models for particle vaporization. The simplest one considered evaporation only after the particle surface temperature reaches boiling point, assuming that the heat flux at the particle surface controls the evaporation rate. In reality the process of evaporation is very complicated, since the evaporation from the particle surface can occur at a temperature lower than the boiling point, and the formation of volatile species can be generated through thermal decomposition and/or reaction with the environment gas.

The maximum molar flux of vaporization from a droplet surface can be predicted by Langmuir equation:

$$N_{\max} = \frac{P_v}{\sqrt{2\pi W R T}} \quad (3.29)$$

where  $P_v$  is the vapor pressure of the liquid material at an absolute temperature  $T$ ;  $W$  and  $R$  are the molecular weight and gas constant. This equation describes the maximum flux of vaporization that could only be expected from a droplet surface at vacuum. When the vaporization occurs in a gaseous atmosphere and vapor pressure lower than the atmospheric pressure, the rate of vaporization will be strongly affected by diffusion of the vapor through the boundary layer around the droplet. The evaporation rate controlled by vapor diffusion through the boundary layer around the particle is described as follows [Wan, 1999]:

$$\dot{m}_v = 2(\bar{\rho}D_g)_f \pi r_p \ln(1 + B) Sh \quad (3.30)$$

where  $Sh$  is the Sherwood number, and  $B$  is the mass transfer number.  $Sh$  accounts for convective mass transfer:

$$Sh = 2.0 + 0.6 \text{Re}_p^{1/2} Sc^{1/3} \quad (3.31)$$

The Schmidt number is defined as:

$$Sc = \frac{\mu_f}{(\rho D)_f} \quad (3.32)$$

Mass transfer number  $B$  is a function of the local mass fraction of vapor in the gas phase and the vapor concentration on the droplet surface:

$$B = \frac{Y^* - \bar{Y}_\infty}{1 - Y^*} \quad (3.33)$$

where  $\bar{Y}_\infty$  is the mass fraction of vapor outside the boundary layer, usually taken at the computational cell, and  $Y^*$ :

$$Y^* = \frac{W_p}{W_p + W_0(\tilde{p}_c / p_v - 1)} \quad (3.34)$$

$Y^*$ , the mass fraction of vapor in the vicinity of the particle surface, is strongly related to the temperature, since vapor pressure,  $p_v$  is a strong function of the temperature. The higher the particle surface temperature is, the higher the vapor pressure is.

The evaporation rate increases rapidly as the particle surface temperature approaches the boiling point. As soon as the heat gained at the surface is not sufficient to meet the latent heat of evaporation needed by this amount of mass,  $\dot{m}_v$ , the rate of evaporation drops. Heat transfer controls the evaporation:

$$\dot{m}_{v,heat} = \dot{q}_{net} / L_v \quad (3.35)$$

The effect of mass transfer on heat and momentum transfer due to evaporation is also taken into account by factor  $f_v$ , which is defined as Eq. (3.28). In addition, the evaporation can also be introduced due to the oxidation of metal with the entrained air under atmospheric operating conditions, and subsequently affect

the heat and momentum transfer. For example, when the temperature of molybdenum particle is between  $500^{\circ}\text{C}$  and the melting point  $2622^{\circ}\text{C}$ , the volatile oxide,  $\text{MoO}_3$ , is formed, which introduce the vaporization of molybdenum due to oxidation.

### 3.1.3 Oxidation

For the oxidation of an in-flight metal particle, a series of processes are involved: transport of oxidizer from gas to the metal surface; reactions at the surface in the form of adsorption, dissociation and incorporation into a solid reaction product; diffusion of anions and/or cations through the oxide scale formed by oxidation; desorption of the gaseous product; and transport of the gaseous product away from the surface into the surrounding. The rate limiting process of the oxidation is the slowest one among the aforementioned processes. For molybdenum particles, three typical oxidation mechanisms can be used.

Diffusion in an oxide thin film. When temperature is below  $450^{\circ}\text{C}$ , an adherent thin film or scale of oxide is formed. The growth rate of the thin film is formulated as [Gulbransen, 1963; Wan, 2001]:

$$\frac{d\xi}{dt} = N\nu v \exp\left(-\frac{W}{kT}\right) \exp\left(\frac{zeaE_0}{kT}\right) \quad [\text{m/s}] \quad (3.36)$$

where  $N$  is the number of ions on “P” sites per unit-area surface,  $a$  is the distance between the ions,  $v$  is the frequency of oscillation,  $V$  is the volume of metal oxide per ion,  $ze$  is the charge on the ion,  $k$  is the Boltzmann’s constant,  $W$  is the energy of formation of the ion, and  $E_0$  is the electric-field strength. The direct application of Eq. (3.36) is difficult because of the lack of the data on the related parameters for molybdenum oxides.

Chemical reactions on the surface. Chemical reactions on a metal surface become the rate determining process when the oxidation temperature ranges from  $500$  to  $700^{\circ}\text{C}$  for Mo. The reaction of



is formed. The reaction (or oxidation) rate can be estimated from

$$\dot{m}_{ox} = A \exp(-E/RT) \quad [\text{kg/m}^3\text{s}] \quad (3.38)$$

Here T is the surface temperature of the particle. The values of the factor  $A = 10^{21.5}$  atom/cm<sup>2</sup>-s (5.04 kg/m<sup>2</sup>-s) and the activation energy E = 19.7 kcal/mole (82.4 kJ/mole) [Gulbransen, 1963].

Diffusion of oxidant in gas. Transport of oxidizer in the gas phase to the metal surface is the diffusion rate controlled process when the surface temperature exceeds 700 °C. If the particle is solid, the reaction mechanism is the same as Eq. (3.37). If the particle is melted, oxygen will be adsorbed in the melt and diffuse in the melt as interstitial atoms represented by



Reaction is a diffusion-controlled process and the diffusion rate of oxygen from the gas to the surface is given as

$$\dot{m}_{ox} = h_m (\tilde{Y}_o - Y_o^*) \quad [\text{kg} / \text{m}^2 \text{s}], \quad (3.40)$$

where  $Y_o$  is the mass fraction of oxidizer (including both atomic and molecular oxygen). The mass transfer coefficient can be obtained from

$$h_m = \frac{Sh(\bar{\rho}D_g)}{2r_p} f_{Kn} \quad \text{where} \quad \bar{\rho}D_g = \frac{\mu_f}{Sc}. \quad (3.41)$$

In the liquid Mo, oxygen atoms diffuse inside the melt. The concentration of interstitial oxygen atoms within the particle is

$$\rho_d \frac{\partial Y_o}{\partial t} = \frac{1}{r^2} \frac{\partial}{\partial r} \left( \rho_d D r^2 \frac{\partial Y_o}{\partial r} \right). \quad (3.42)$$

The concentration of interstitial oxygen satisfies the conditions:

$$\text{at } r = 0: \left. \frac{\partial Y_o}{\partial r} \right|_{r=0} = 0, \quad (3.43)$$

$$\rho_d D \left. \frac{\partial Y_o}{\partial r} \right|_{r=r_p} = \dot{m}_{ox} \quad \text{at the surface of the particle:} \quad (3.44)$$

### 3.2 Particle effects to the plasma flame

Most current models for the particle-plasma interaction assume that the effects of loaded particles on the plasma jet are negligible. However, this is not the case in practice, especially when the particle feeding rate is high. Also, the small amount of injected particles can have a great influence on the plasma turbulence structure. Recently, some models have been proposed for the two-way interaction of the particle and plasma jet. Ramachandran and Nishiyama [2002, 2004] developed a three-dimensional model with considering the two-way interactions of energy, momentum and turbulence.

In our model, the effect of plasma cooling by the injected particles is incorporated, by considering the source terms of heat and momentum for coupling the particle phase to the gas phase equations. The particles in the LAVA code are considered as discrete Lagrangian entities that interact with the plasma gas. Each computational particle represents a group of similar real particles and it is stochastically generated by sampling from the probability distributions of the particle size, velocity and its direction at the injection nozzle.

For coupling the particles and gas phases, the exchange terms of momentum  $F_p$  and heat  $\dot{Q}_{conv}$  and  $\dot{Q}_{rad}$  must appear with the opposite sign in the fluid dynamical equations for the plasma gas. For this purpose, it is necessary to sum over all particles in the corresponding computational cell. Therefore, the source terms due to injected particles in the governing equations of plasma jet are defined as:

$$F = -\frac{1}{\alpha V_{cell}} \sum_p N_p F_p \quad (3.45)$$

$$\dot{Q} = \frac{1}{\alpha V_{cell}} \sum_p N_p \left[ 4\pi r_p^2 h (T_s - \tilde{T}_f) + F_p (\tilde{\vec{V}} + \vec{V}' - \vec{V}_p) \right] \quad (3.46)$$

$$\dot{W} = -\frac{1}{\alpha V_{cell}} \sum_p N_p F_p \vec{V}' \quad (3.47)$$

### 3.3 Stochastic scheme of multiple particle generation

The method for solving particle generation is based on the ideas of Monte Carlo method and discrete particle method [Amsden, 1989]. The particles are created by sampling randomly from assumed

probability distributions that govern particle properties at injection, *i.e.*, position, size and velocity. Given the distribution function  $f(x)$  corresponding to the random variable  $x$  ( $x_1 \leq x \leq x_2$ ), such as shown in Fig. 3.2, the number of particles in the interval  $dx$  about the value  $x$ , is given according to distribution function  $f(x)$ :

$$dN = f(x)dx \quad (3.48)$$

The random variable,  $P$ , is defined as:  $P(x) = \int_{x_1}^x f(x')dx'$ , and it is noted that  $N(x) = P(x)$ . Hence, the

number of particles is uniformly distributed with respect to the variable  $P(x)$ . Commonly, the random number generator with a uniform distribution in the range from zero to one. Therefore, if we sample from

the given distribution of  $x$ , and scale by  $\int_{x_1}^{x_2} f(x)dx$  to obtain  $P(x)$ :

$$P(x) = \frac{\int_{x_1}^x f(x')dx'}{\int_{x_1}^{x_2} f(x)dx} \quad \text{and} \quad P(x) \in [0, 1] \quad (3.49)$$

Then invert the random number  $P$  to get  $x$ , which is then distributed according to  $f(x)$ .

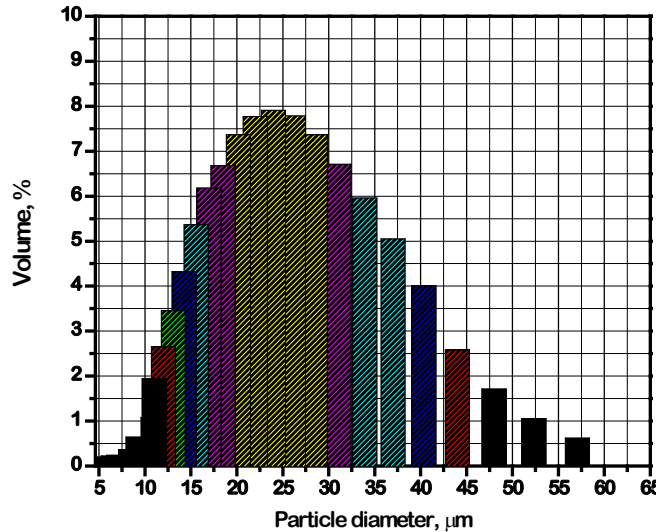


**Figure 3.2. Random distribution of particle size.**

## Chapter 4

### Computational Scheme

The procedures for numerical solutions of the equations governing the plasma jets and particles are presented in this chapter. The numerical algorithm uses the Eulerian and Lagrangian approaches for the gas and particle phases, respectively.

#### 4.1 Plasma jet

The governing equations of the DC plasma jet, as presented in Section 2.1, are discretized using an explicit scheme and solved in the LAVA program. Whereas, the governing equations of the RF plasma jet in Section 2.2 are discretized using an implicit scheme and solved by the SIMPLE algorithm.

##### 4.1.1 DC Plasma jet

The governing equations for the DC plasma jet (Eqs. 2.3, 2.4, 2.6 and 2.10) can be generalized as:

$$\frac{\partial(R\phi)}{\partial t} + \nabla \cdot (R\phi\vec{u}) = \nabla \cdot (RD\nabla\phi) + S_\phi, \quad (4.1)$$

where  $\nabla \cdot (R\phi\vec{u})$  and  $\nabla \cdot (RD\nabla\phi)$  are convection and diffusion terms for different governing equations, respectively, and  $S_\phi$  is the source term. The explicit algorithm is used for solving this equation numerically.

The simulation of the plasma jet uses an explicit temporal differencing with respect to a sequence of discrete times:

$$\left( \frac{\partial\phi}{\partial t} \right)_n = \frac{\phi^{n+1} - \phi^n}{\Delta t}, \quad (4.2)$$

The spatial differencing is derived by the finite volume method in which the temporally differenced

equations are averaged over the area or volume of the mesh cell [Ranocha, 1992], such as follows,

$$\phi = \begin{cases} \frac{1}{A} \int_A \phi \, dA & \text{(for 2D planar)} \\ \frac{1}{V} \iiint_V \phi \, dx \, dy \, dz & \text{(for 3D cylindrical)} \end{cases} \quad (4.3)$$

Specifically, in current 2-D ( $r, y$ ) or 3-D ( $r, \theta, y$ ) cylindrical coordinate we investigate:  $dx = dr$ , and  $dz = rd\theta$ .

$$\begin{aligned} \text{The diffusion term } \nabla \cdot (R D \nabla \phi) |_P &\text{ is discretized as: } \sum_{\alpha} A_{\alpha} R_{\alpha} D_{\alpha} \vec{n}_{\alpha} \cdot (\nabla \phi)_{\alpha} \\ &= \frac{1}{dx} (f_{x,P} - f_{x,W}) + \frac{1}{dy} (f_{y,P} - f_{y,S}) + \frac{1}{dz} (f_{z,P} - f_{z,B}) \end{aligned} \quad (4.4)$$

where  $f_{x,P} = x_e \cdot \frac{D_p + D_e}{2} \cdot \frac{\phi_e - \phi_p}{\delta x}$ , and the subscript B represents the cell in the plane behind the  $x$ - $y$

plane showed in Fig. 4.1, corresponding to cell P (the shadow enclosed by dashed lines and centered at P).

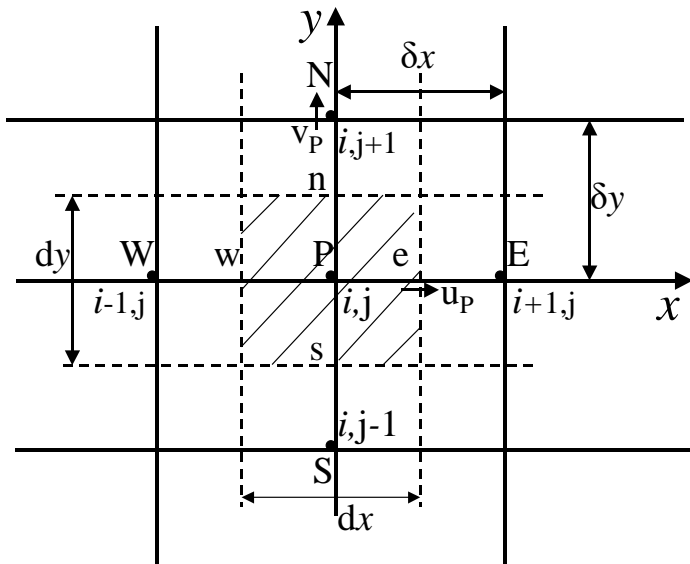


**Figure 4.1: Computational cells for plasma jet domain at x and y directions.**

In spatial differencing, the momentum equations are averaged over auxiliary momentum cells centered on the regular cell faces. The different velocity components are averaged over different momentum cells. The convection terms are evaluated by a weighted average of centered and upwind scheme, and all other terms are evaluated as simple centered differences. Thus, the convection term is discretized as:

$$\begin{aligned}
\nabla \cdot (\phi \vec{u}) &= \frac{1}{\Delta x \Delta y \Delta z} \sum_{\alpha} A_{\alpha} \phi_{\alpha} \vec{n}_{\alpha} \cdot \vec{u}_{\alpha} \\
&= \frac{1}{dx} (f_{x,P} - f_{x,W}) + \frac{1}{dy} (f_{y,P} - f_{y,S}) + \frac{1}{dz} (f_{z,P} - f_{z,B})
\end{aligned} \tag{4.5}$$

where  $f_{x,P} = [(1 - \omega_P) \phi_E + \omega_P \cdot \phi_P] u_P$ , and  $\omega$  is the weight factor of velocity.

The time step is automatically given based on stability restrictions of convection, diffusion, propagation of sound waves,  $\Delta t_c$ ,  $\Delta t_d$ , and  $\Delta t_s$  respectively. It is derived after simplifying the stability analysis by assuming a uniform mesh and neglecting some terms [Ramshaw, 1992]:

$$\Delta t = \min(f \Delta t_c, f \Delta t_d, f \Delta t_s, 1.05 \Delta t^n) \tag{4.6}$$

where  $f < 1$ , and the factor of 1.05 ensures an increase of time step no more than 5%, and:

$$\Delta t_c = \min \left[ \left( \frac{|u|}{\Delta x} + \frac{|v|}{\Delta y} + \frac{|w|}{\Delta z} \right)^{-2} \left( \frac{u^2}{\Delta x^2} + \frac{v^2}{\Delta y^2} + \frac{w^2}{\Delta z^2} \right)^{\frac{1}{2}} \right], \tag{4.7}$$

$$\Delta t_d = \min \left[ \frac{1}{2D_{\max}} \left( \frac{1}{\Delta x^2} + \frac{1}{\Delta y^2} + \frac{1}{\Delta z^2} \right)^{-1} \right], \tag{4.8}$$

$$D_{\max} = \max \left( \frac{2\mu + \lambda + 2\mu_t + \lambda_t}{\rho}, \frac{k + c_p \mu_t / \text{Pr}}{\rho c_v}, D_i + D_t \right), \tag{4.9}$$

$$\Delta t_s = \min \left[ \frac{1}{c_{se}} \left( \frac{1}{\Delta x^2} + \frac{1}{\Delta y^2} + \frac{1}{\Delta z^2} \right)^{\frac{1}{2}} \right], \tag{4.10}$$

where the “min” operation is taken over all cells in the computational domain, and  $c_{se}$  is the effective sound speed, which is the true sound speed in un-accelerated transient calculations.

#### 4.1.2 RF Plasma jet

The governing equations of the velocity, temperature and species concentration are solved using the SIMPLE algorithm [Patankar, 1985]. The computational simulations were performed with the uniform staggered  $160 \times 60$  grids in axial and radial directions respectively. The computational domain for the

electromagnetic field is extended to outside of the plasma region, using the non-uniform  $282 \times 175$  grids in axial and radial directions respectively.

## 4.2 Particle

The governing equations for the particle heat and mass transfer, as detailed in Section 3.1.1 and Section 3.1.3, are also solved. The moving boundaries of the phase-change interfaces in one-dimensional spherical geometry require specific numerical treatments. In this study, the scheme of coordinate transformation has been used.

### 4.2.1 Coordinate transformation of particle equations

To fix the moving boundaries of the phase-change interfaces, a numerical technique of coordinate transformation has been used to nondimensionalize the original physical coordinate, when calculating the temperature and oxide distribution inside the particle [Wan, 1999]. Each physical domain separated by the phase-change interface has been transformed to a corresponding computational domain starting from 0 to 1. The governing equation and boundary conditions are also transformed.

If a one-dimensional domain, index by  $i$ , has two dependent boundaries:  $r_i^- = f(t)$  and  $r_i^+ = g(t)$ ,

it can be mapped to a domain not time-dependent using the following equation:

$$\xi_i = \frac{r - f(t)}{g(t) - f(t)} \quad f(t) \leq r \leq g(t) \text{ and } 0 \leq \xi_i \leq 1 \quad (4.11)$$

where  $f(t)$  and  $g(t)$  represent the inner and outer radii of one phase domain, respectively. For example, for the liquid phase of a partially melted particle,  $f(t)$  and  $g(t)$  are 0 and  $r_m$  respectively.

Using this transformation, each physical domain separated by the phase-change interface is transformed to a corresponding computational domain starting from 0 to 1. The Eq. (3.8) is transformed to:

$$\rho_p C_p \frac{\partial T}{\partial t} = \frac{1}{(g-f)^2 [(g-f)\xi_i + f]^2} \frac{\partial}{\partial \xi_i} \left\{ k [(g-f)\xi_i + f]^2 \frac{\partial T}{\partial \xi_i} \right\} + \rho_p C_p \frac{\partial T}{\partial \xi_i} \left( \frac{\xi_i}{g-f} \frac{dg}{dt} + \frac{1-\xi_i}{g-f} \frac{df}{dt} \right). \quad (4.12)$$

The boundary conditions for each domain are given as, for example, the boundary equations (3.9-3.11) are transformed to:

$$\left. \frac{\partial T}{\partial \xi_1} \right|_{\xi_1=0} = 0 \quad (4.13)$$

$$\frac{1}{r_m} \left( k_p \left. \frac{\partial T}{\partial \xi_1} \right|_{\xi_1=1} \right) - \frac{1}{r_p - r_m} \left( k_p \left. \frac{\partial T}{\partial \xi_2} \right|_{\xi_2=0} \right) = L_m \rho_p \frac{dr_m}{dt} \quad (4.14)$$

$$4\pi r_p^2 \frac{1}{r_p - r_m} \left( k_p \left. \frac{\partial T}{\partial \xi_2} \right|_{\xi_2=1} \right) = \dot{Q}_{conv} + \dot{Q}_{vap} + \dot{Q}_{rad} \quad (4.15)$$

The equations in other computational domain are transformed in the same way. For the case considered here,  $f(t)$  and  $g(t)$  are defined in solid, liquid and resolidified regions as follows:

Solid region 1:  $0 < r < r_m$ :  $f(t) = 0$ ,  $g(t) = r_m$ ;

Liquid region 2:  $r_m < r < r_p$ :  $f(t) = r_m$ ,  $g(t) = r_p$ ; (4.16)

Resolidified region 3:  $r_s < r < r_p$ :  $f(t) = r_s$ ,  $g(t) = r_p$ .

#### 4.2.2 Numerical scheme for particles

Governing and boundary equations for internal heat conduction inside the particle, Eqs. (4.12-4.15), is solved using the finite volume method. The finite differencing equation of nodal temperature is obtained by the integration of the differential equations from time  $t$  to  $t+\Delta t$  over each control volume cell. For example, for Eq. (4.12), the corresponding difference equation for the temperature at node  $J$  in the solid is given as:

$$a_p T_i^n = a_E T_{i+1}^n + a_W T_{i-1}^n + b \quad (4.17)$$

$$a_E = \frac{\Delta t}{\Delta R^2} \frac{k_e r_e^2}{(\delta \xi)_e^2} + \frac{\rho c_p}{\Delta R} \frac{(\Delta r)_e r_e^2}{2} \quad (4.18)$$

$$a_W = \frac{\Delta t}{\Delta R^2} \frac{k_w r_w^2}{(\delta \xi)_w^2} - \frac{\rho c_p}{\Delta R} \frac{(\Delta r)_w r_w^2}{2} \quad (4.19)$$

$$a_p = a_E + a_W + \rho c_p \frac{r_e^2 + r_w^2 + r_e r_w}{3} \Delta \xi \quad (4.20)$$

$$b = \rho c_p T_P^{n-1} \frac{r_e^2 + r_w^2 + r_e r_w}{3} \Delta \xi \quad (4.21)$$

where:

$$\Delta R = r_i^+ - r_i^- \quad (4.22)$$

$$r_e = \xi_e + \frac{r_i^-}{r_i^+ - r_i^-} \quad (4.23)$$

$$(\Delta r)_e = dr_i^- + \xi_e (dr_i^+ - dr_i^-) \quad (4.24)$$

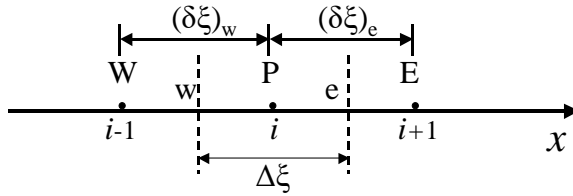


**Figure 4.2: Computational cells for particle transport equations.**

## Chapter 5 Parametrical Studies of DC Plasma Spray in 3-D Geometry

The integrated model developed in Chapter 2 and Chapter 3 for the DC plasma flame and the particle-plasma interaction is applied to simulate the DC plasma spray process. The plasma temperature and particle behaviors are predicted numerically and compared with the experimental data. Effects of the operating conditions on the particle behaviors are investigated.

### 5.1 Introduction

The modeling of plasma spray process has received considerable attention during the last few decades. Numerical simulation has been very helpful in improving the scientific understanding of the complex heat, momentum and mass transport phenomena involved, and the process control and optimization. Most of these efforts were primarily conducted in 2-D configurations. The effects of carrier gas flow and particle injection are typically neglected in these models because the complex 3D interaction of carrier gas with

the jet cannot be accurately modeled with an axisymmetric assumption. However, the carrier gas flow injection, which enables the particle entrainment in the high-temperature high-velocity plasma jet, does disturb the flame and has significant influence on the in-flight particle characteristics [Fincke, 1997 and 2000]. The understanding of carrier gas effects on plasma jet and particle behavior is desirable for the control and design of plasma spray process.

The study of three-dimensional behavior of the plasma jet reflecting actual conditions has been started in the last few years. Ahmed and Bergman [2001] studied the ceramic particles in Ar-H<sub>2</sub> plasma jet using a 3-D model coupled with the commercial computational code FLUENT. Li and Chen [2002] developed a three-dimensional computational model that is capable of handling transverse carrier gas injection and its influence on the plasma jet behavior and particles trajectories. Mariuax and Vardelle et al. [2001 and 2003] have performed 3-D simulations for the plasma spray process, in which the conversion of energy in the torch nozzle, from electric power to thermal energy, is considered. However, most authors use empirical velocity and temperature profiles at the nozzle exit matching with the plasma gas mass flow rate and its enthalpy, due to the complexity of the arc dynamics inside the torch with its attachment to the anode-nozzle wall [Herberlein, 1999]. The local thermodynamic equilibrium is also generally assumed. Noted that most three-dimensional models so far are based on the assumption that the particle is in uniform temperature during in-flight. And some models neglect the effects of particles on the plasma gas.

In this chapter, a three-dimensional transient numerical model for plasma jet and particle is developed to investigate the plasma jet perturbation by carrier gas and particle loading, and their effects on the in-flight particle behavior. The plasma jet and the particle trajectory are described in the three-dimensional geometry, and the non-thermal equilibrium of the particle in-flight is considered by employing one-dimensional thermal model. This model is incorporated into the LAVA code, originally developed at INEEL in a two-dimensional geometry. The modified computational code LAVA-P-3D is tested with experiment and further applied to thermal spray process. The numerical simulations are

performed to investigate the three-dimensional behavior of the plasma jet and its influence on particle in-flight velocity and temperature.

## 5.2 Basic description of the problem

The present study is conducted for a D.C. plasma system that uses Metco 9MB plasma gun with the inner,  $R_i$ , and outer,  $R_o$ , radius of the nozzle as 0.39 cm and 1.5 cm, respectively. The powder materials of Mo (molybdenum),  $ZrO_2$  (zirconium oxide or zirconia) and NiCrAlY subjected to heating by the Argon-hydrogen plasma jet have been simulated for the initial particle size ranging from 5 – 120  $\mu\text{m}$ . The injector is located at 8 mm above the plasma central axis, and 6 mm from the plasma gun exit. The basic operating conditions for plasma gun are listed in Tables 5.1, and the particles conditions of Mo, NiCrAlY and  $ZrO_2$  and their properties are listed in Table 5.2.

The computational domain and some of the boundary conditions employed in the calculation of plasma jet are described in Fig. 5.1. The simulation is based on the three-dimensional computational domain, with the mesh size of  $44 \times 53 \times 24$  in the cylindrical coordinate ( $r, y, \theta$ ) system. The radius and axial lengths of the computational regime are 6 cm and 15 cm, respectively; while  $2\pi$  in the circular direction. The calculations are initialized from the cold air mixing with the incoming jet until the steady state is reached.

**Table 5.1: Basic operating conditions for DC plasma torch**

Processing parameters	Value
Gun nozzle exit	8mm
First plasma gas, Ar, slm	40
Secondary plasma gas, $H_2$ , slm	7
Arc current, A	500
Voltage, V	61
Carrier gas material	Ar
Carrier gas flow rate, slm	1.5-15.0
Injector position ( $y, z$ ), cm	(0.6, 0.8)
Injector diameter, mm	1.8

**Table 5.2: Particle conditions and properties**

Particle material	Mo	ZrO <sub>2</sub>	NiCrAlY
Particle feeding rate, g/s	0.5-4.5		
spray distance, cm	8-10		
Average particle size, $\mu\text{m}$	40	30	50
$k_s$ , W/m-K	84	2.0	74
$k_i$ , W/m-K	46	2.32	43
$C_{p,s}$ , J/kg-K	339	580	448
$C_{p,l}$ , J/kg-K	570	713	448
$\rho_s$ , g/cm <sup>3</sup>	10.2	5.89	8.1
$\rho_l$ , g/cm <sup>3</sup>	9.35	5.89	8.1
Minimum $T_m$ , K	2895.1	2950	1360
Maximum $T_m$ , K	2895.1	2950	1411
$L_m$ , kJ/kg	375.3	707	299
$L_{evap}$ , kJ/kg	6150	6000	7330

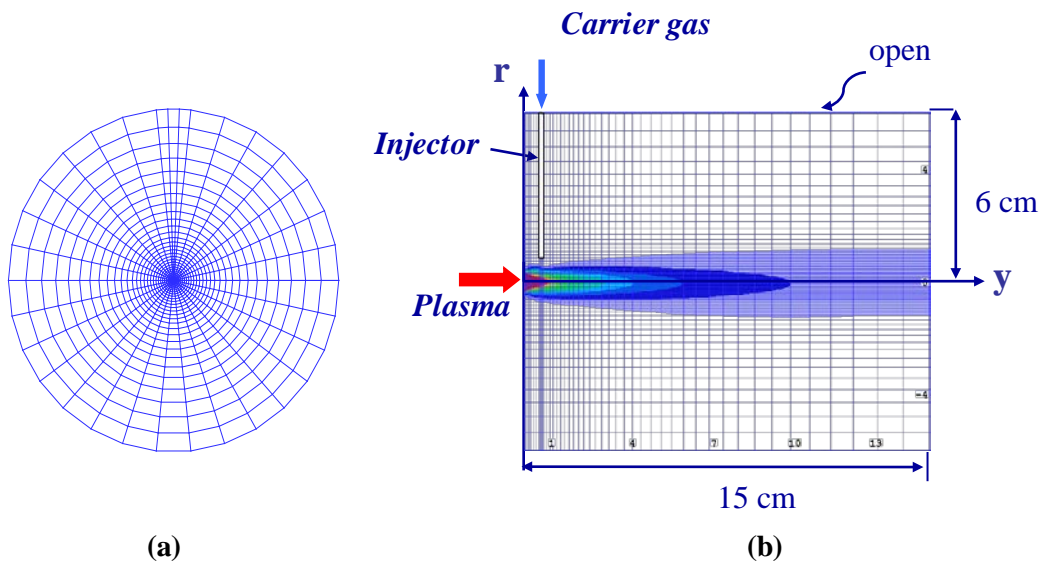
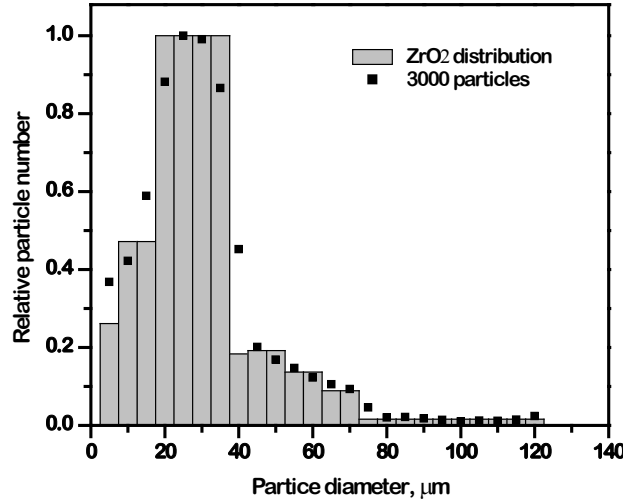


**Figure 5.1: Geometry, computational mesh and boundary conditions in: (a) cross section plane in radial and azimuthal directions, (b) middle section plane of 3D plasma jet.**

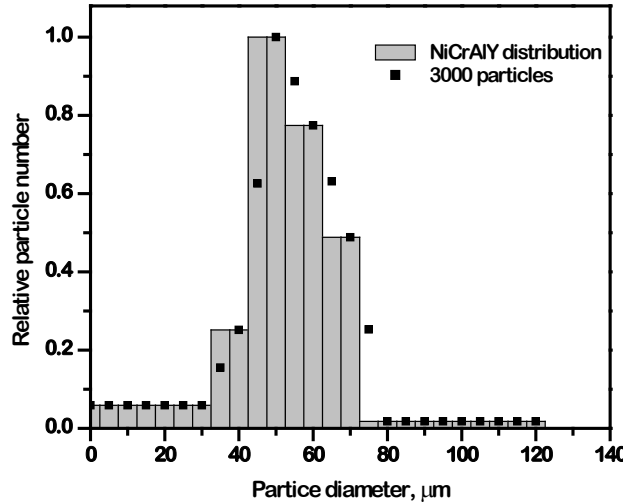
### 5.3 Development of LAVA-P-3D

To accurately predict the 3D plasma jet and in-particle behavior, special treatments have been proposed and incorporated into the LAVA-P-3D code for the boundary conditions, the side injector and the carrier gas injection.

- Boundary conditions at the axis of plasma jet and at the circular direction have been specified, stated at Sec. 2.1.5.
- The side injector is treated as a solid block that has zero diffusivity and infinitely large viscosity. The thermal conductivity of this solid block is assumed as 80 W/m-K. The meshes for the side jet nozzle exit have been refined with a grid size of 6×3 for the nozzle diameter of 1.8 mm. (see Fig. 5.1).
- The carrier gas is treated as an additional source adding to the momentum and energy at the control volumes that contain the side injector nozzle exit plane. Injected particles are also treated as momentum and energy source terms for the control volumes where the particles reside.
- The entrained particles are discretely treated in a Lagrangian coordinate and stochastically generated by sampling from the probability distributions of the particle size and its velocity at the injection nozzle. Multiple particles have size, velocity, direction, and position distributions at injection. Fig. 5.2 shows the particles stochastically generation in the simulations along with the original sampling of particle size distribution achieved from experiments, for NiCrAlY and ZrO<sub>2</sub> respectively. The velocity assigned to each particle is the measured average particle velocity at the injector exit with a random deviation within 5%; the direction with regard to injector axis is given by a random distribution from 0 to 20°. The particle positions are randomly distributed in the exit plane of the injector. About 2000-3000 particles are injected in the flow after introducing the carrier gas.



(a)



(b)

**Figure 5.2: (a) ZrO<sub>2</sub> and (b) NiCrAlY particle size distribution and the data achieved in the simulation.**

**Validation with LAVA 2D.** To validate the LAVA 3D code, we have chosen a case in which the plasma jet is symmetric about the jet axis and simulated it using both LAVA 2D and LAVA 3D. When using the LAVA 3D, zero initial velocity in the circular direction was assigned. The operating conditions are

described in Table 5.3. Should the LAVA 3D code work correctly, it is expected that the results from the LAVA 2D and LAVA 3D are the same.

**Table 5.3: Operating conditions for the DC plasma torch in 2D and 3D.**

Processing parameters	Values	
Current, Amp	500	
Voltage, Volt	61	
Power efficiency	0.64	
Primary gas flow, Ar, slm	40	
Secondary gas, H <sub>2</sub> , slm	7	
Initial particle average velocity, cm/s	980	
	LAVA 2D	LAVA 3D
Geometry	6cm × 15cm	6cm × 15cm × 2π
Grid meshes	44×53	44×53×24

LAVA 3D has been applied to the plasma jet that is axisymmetric in nature. Figs. 5.3(a)-(c) show the temperature, velocities in the radial and axial directions, respectively predicted by LAVA 2D and LAVA 3D at the spray distance of 0.5, 1.0, 2.5, 5.0 and 10.0 cm. Fig. 5.3(d) shows the distribution of the velocity component in the circular direction from the LAVA 3D. Noted that the results from LAVA 3D are only those at  $\theta = 90^\circ$ . It is seen that the predictions from the 2D and 3D configurations are almost identical except the value of circular velocity. The circular velocity in the 2-D computational domain is zero as a result of axisymmetric assumption; while a small value (order of  $10^{-5}$ ) in the 3-D computational domain is believed to be run-off error. The particle behavior in the 3-D plasma jet computational domain has also been simulated and compared with that in 2-D. Fig. 5.4 shows the trajectories of the particles, while Figs. 5.5(a)-(b) are the particle velocity and temperature. Virtually no difference is observed, indicating that the LAVA 3D with particle injection works correctly.

It should be noted that the movement of particles in 2D plasma domain is assumed to be axisymmetric about the plasma jet axis and a pseudo 3-D particle model is implied. As a result, the trajectory of the particle turns up when it passed through the axis. This is only true when the carrier gas is absent and the plasma jet is considered to be axisymmetric about the axis with single particle. In reality,

multiple particles are loaded along with carrier gas and the plasma jet exhibits strong three-dimensional behavior.

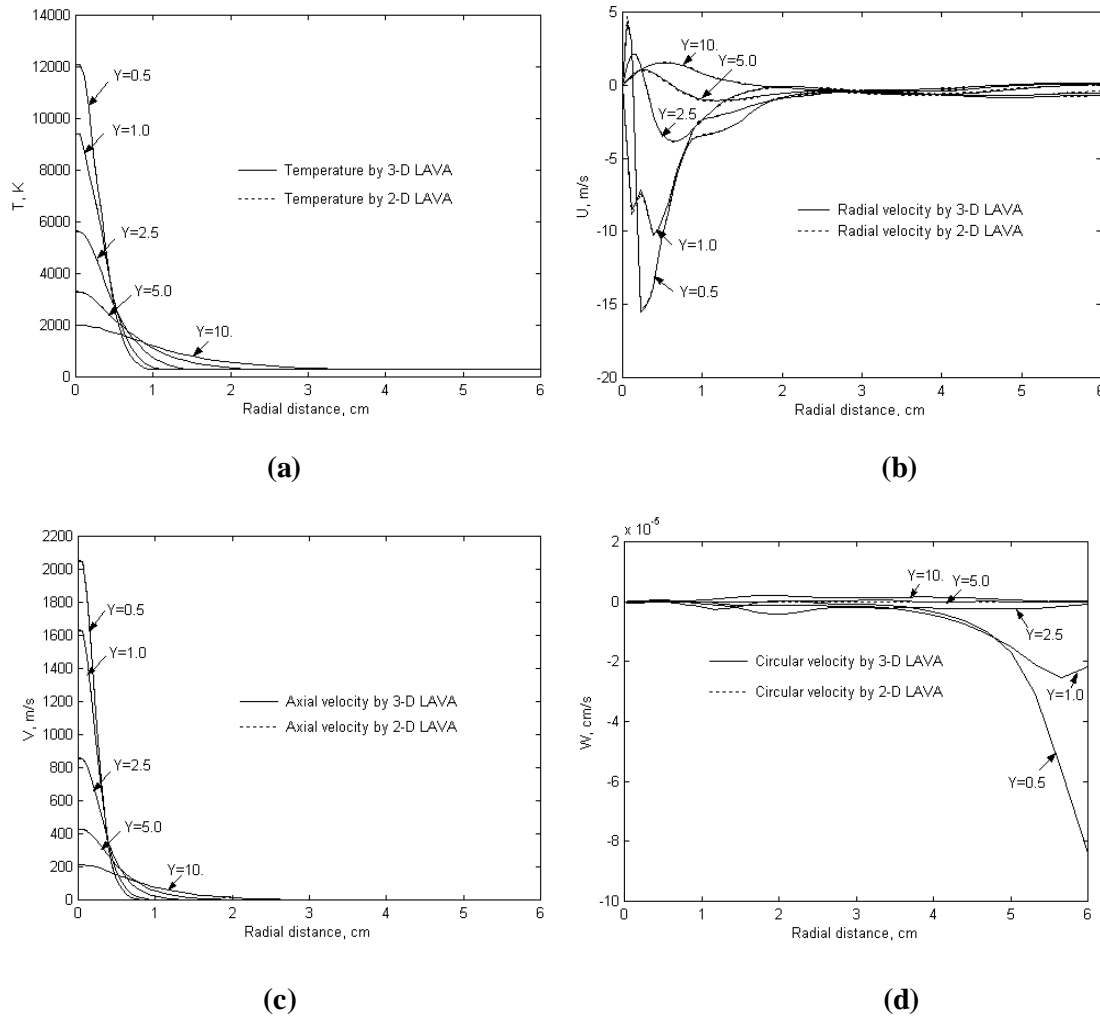


**Figure 5.3: (a) Gas temperature, (b) radial velocity, (c) axial velocity, and (d) circular velocity obtained from the LAVA 2D (dash line) and LAVA 3D at  $\theta = 90^\circ$  (solid line) at the spray distance of 0.5, 1.0, 2.5, 5.0 and 10.0 cm.**

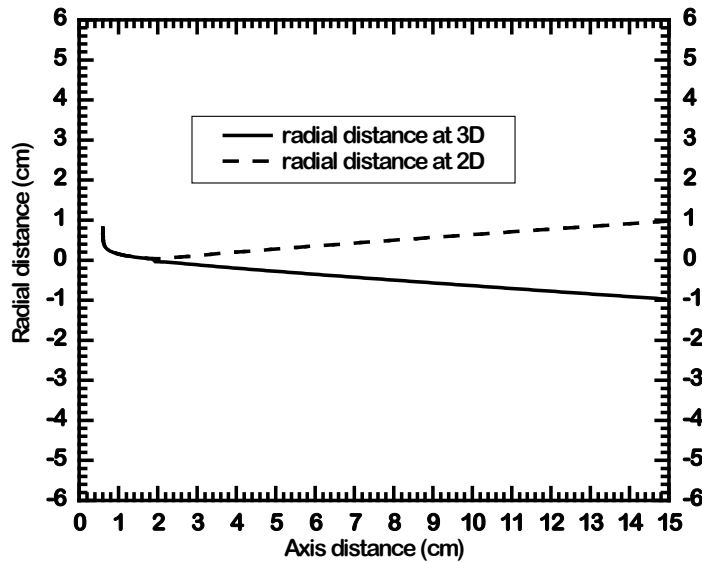


**Figure 5.4:** Trajectories of particles calculated from LAVA 2D and LAVA 3D models, respectively.

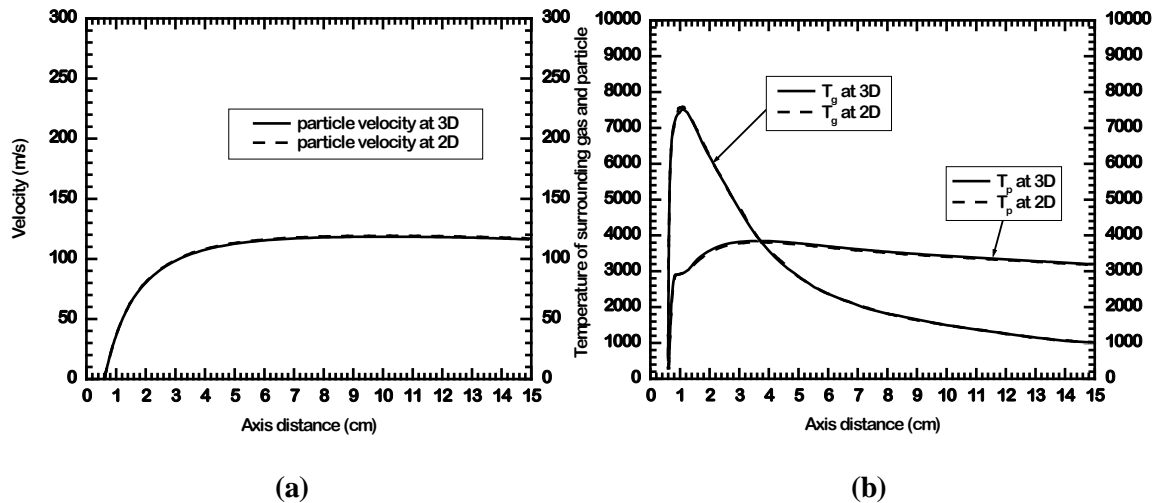


**Figure 5.5:** (a) Particle velocity and (b) temperatures of particle surface and gas surrounding the particles calculated from LAVA 2D and LAVA 3D models, respectively.

**Validation with experiments.** The numerical results have also been compared with the experiments conducted at INEEL [Fincke, 1997]. Their experiment used a Metco 9MB spray gun and Miller model

1270 powder feeders, with spray conditions as listed in Table 5.4. The powders, Praxair NiCrAlY, Ni-346-1 and Sulzer-Metco stabilized zirconia, 204NS, were roughly spherical as supplied. The particle size distributions were obtained by sieving experimentally, as shown in Fig. 5.2; such data were used for the multiple particle generation in the simulation.

In the experiment, the Torch Diagnostic System (TDS-1610) and the Inflight Particle Pyrometer (IPP-2000) were used to measure the particle trajectory information and ensemble particle temperature. Particle velocity and size were measured by the Aerometrics Phase Doppler Particle Analyzer (PDPA) system. The averaged particle injection velocity and carrier gas velocity have been measured at the 2mm downstream of the injector tip for different carrier gas flow rate; the results are used as input data for the simulation.

Due to the lack of the experimental data for plasma gas velocity and temperature, the validation of numerical model is currently restricted to the particle velocity and temperature; in this case the particle average velocity after injection is compared with the experiment results. Both experiment and simulation were conducted based on the same operating conditions, as listed in Table 5.4. The predicted particle velocity at the centerline of the injector after injection is plotted against the experimental data [Fincke, 1997] in Fig. 5.6 for zirconia and NiCrAlY particles. A good agreement between the simulation results and experimental data has been obtained; the difference between the experiment and simulation is within 10%.

**Table 5.4: Operating conditions for the benchmark case**

Processing parameters	Value
Gun nozzle exit	8mm
First plasma gas, Ar, slm	40
Secondary plasma gas, H <sub>2</sub> , slm	12
Arc current, A	600
Voltage, V	75
Thermal efficiency	75%
Carrier gas material	Ar
Carrier gas flow rate, slm	6.0
Injector position (y, z), cm	(0.6, 2.0)

Injector diameter, mm	1.8
-----------------------	-----

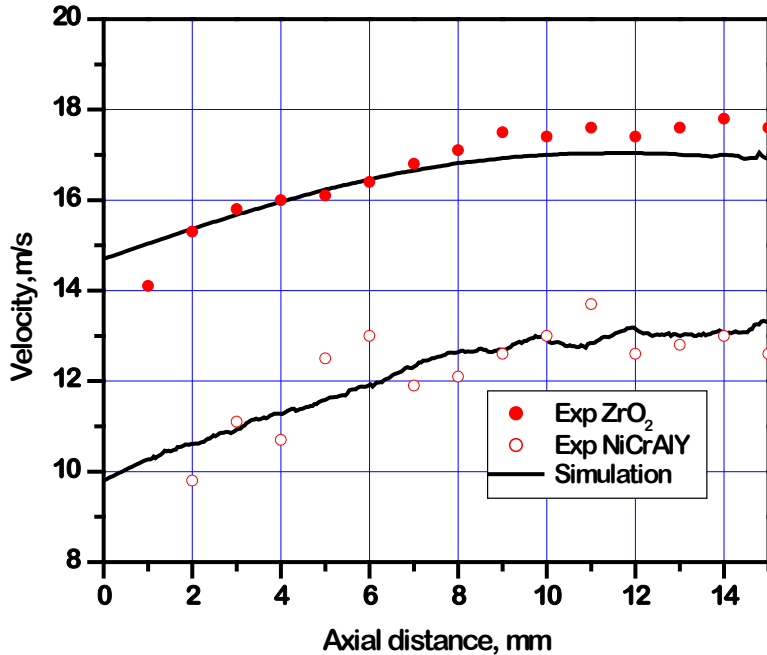


**Figure 5.6:** Particle velocity along the centerline of the side injector after particles exit from the injector, where the solid-line represents the simulation result, and symbols are experimental results [Fincke, 1997 and 2000].

#### 5.4 Results of 3-D plasma jet

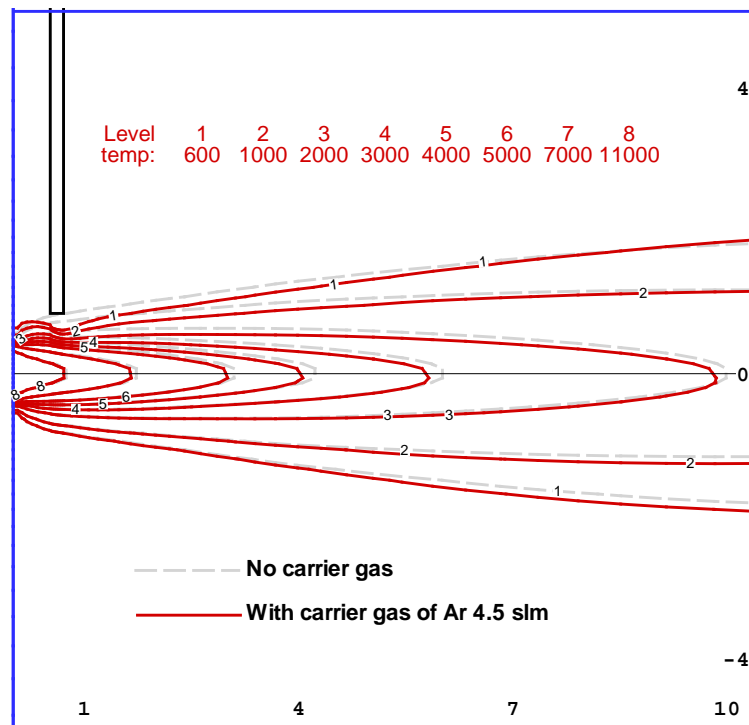
##### 5.4.1 Effects of carrier gas flow on plasma jet

To examine the side injection effect, the 3D cases based on the operating conditions of Table 5.1 have been simulated. The Ar carrier gas is injected from the side injector located at 8 mm above the plasma central axis, with gas flow rate varying from 1.5 to 15 slm. Fig. 5.7(a) shows the gas temperature contours in the plasma jet at the cross section of ABCE with carrier gas rate 4.5 slm compared to the case without carrier gas; fig. 5.7(b) shows the gas velocity vector at this plane. It is clear that the temperature contour is not symmetric about the axis of the jet, rather shifts from the centerline towards the bottom, which is believed the result of side carrier gas injection. This shift is aggravated at the downstream of the plasma jet. Shifts of temperature contour and the change of fluid pattern are also observed in the area of cross section S-S, which is shown in Fig. 5.8.

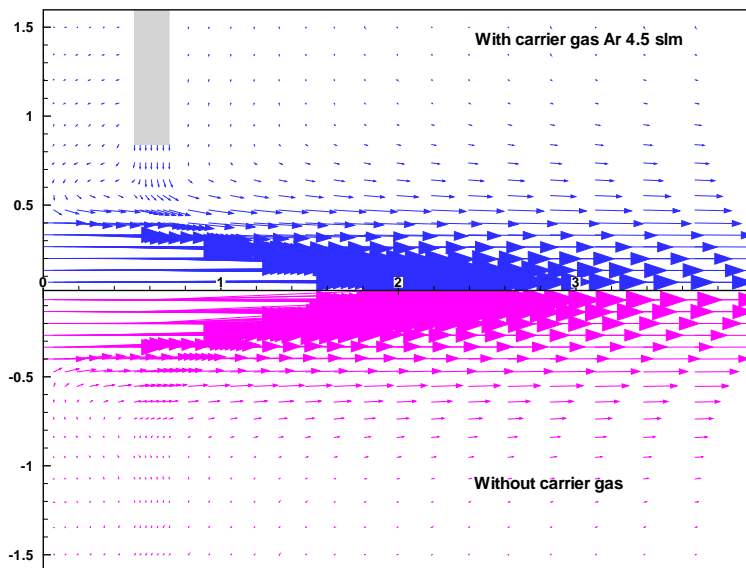
The influence of carrier gas injection on plasma jet fluid can be very large, depending on the carrier gas flow rate, injection location and plasma conditions. As an example, the case with large carrier gas flow rate, 15 slm, has been simulated. Figure. 5.9(a) shows the gas temperature contours in the plasma jet at the cross section of ABCE with carrier gas rate 15 slm; Fig. 5.9(b) shows the gas velocity vector at this plane. For this case, the flow pattern of the plasma jet is significantly influenced by the injection of carrier gas, especially at the area downstream of the injector. The vortex induced by the carrier gas flow is also present in the area adjacent to the injector, as shown in Fig. 5.9(b). For quantitative results, Figure 5.10(a) and Fig. 5.10(b) show the temperature and axial velocity profiles at the cross lines that crosses the plasma jet axis and is parallel to line AB (see Fig. 1.1) for the carrier gas flow rates of 15 slm. Solid, dashed, dotted, and dash-dot lines represent the results at the downstream distance of 0.6, 1.0, 1.5 and 5 cm, respectively, where the arrows indicate the direction of the carrier gas injection; that is from top to bottom. For the typical values of carrier gas flow rate used, *i.e.*, 1.5 to 6 slm, the angle between the plasma jet axis and the torch axis is about one degree, while for carrier gas flow rate of 15 slm it has the larger angle of 2.9 degree.

The effects of carrier gas flow rate on the plasma jet velocity and temperature are shown in Fig. 5.11, which represents the gas radial velocity at the centerline of plasma jet (line OD in Fig. 1.1) with carrier gas flow rates of 1.5, 3.0, 4.5, and 6.0 slm. By increasing carrier gas flow rate, the radial velocity increases at the centerline. The injection of carrier gas results in the deflection of the plasma jet and such deflection is aggravated by the increasing carrier gas flow rate. As a result, the flow change will directly affect the particle velocity and trajectory after leaving the injector exit.

The effects of carrier gas flow rate on the radial profile of the plasma jet velocity and temperature are shown in Fig. 5.12. Results show that the injection of carrier gas results in the deflection of the plasma jet and such deflection is aggravated by the increasing carrier gas flow rate.

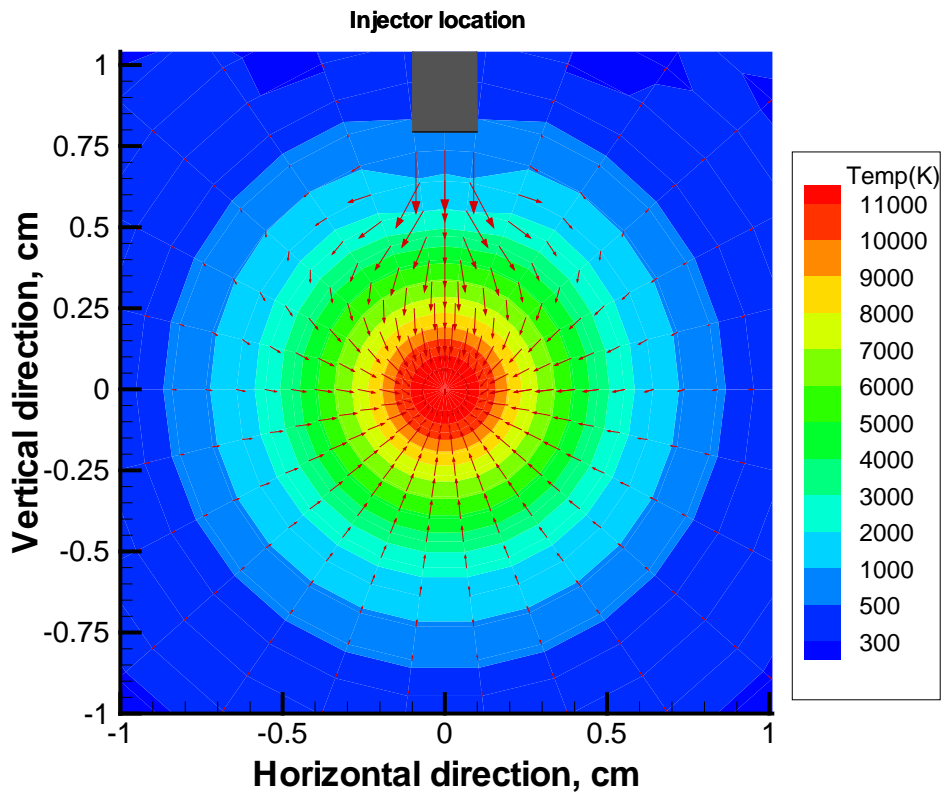


(a)

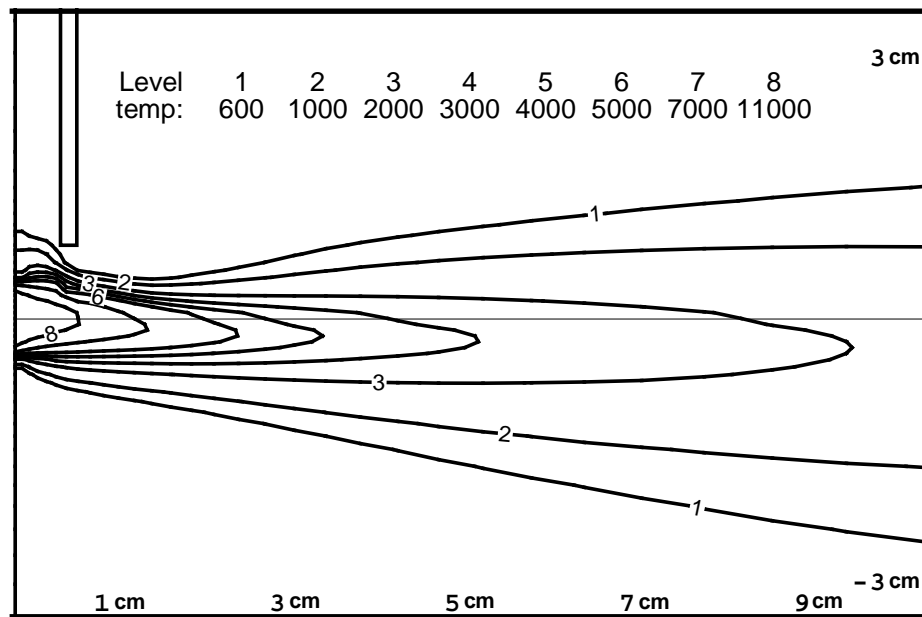


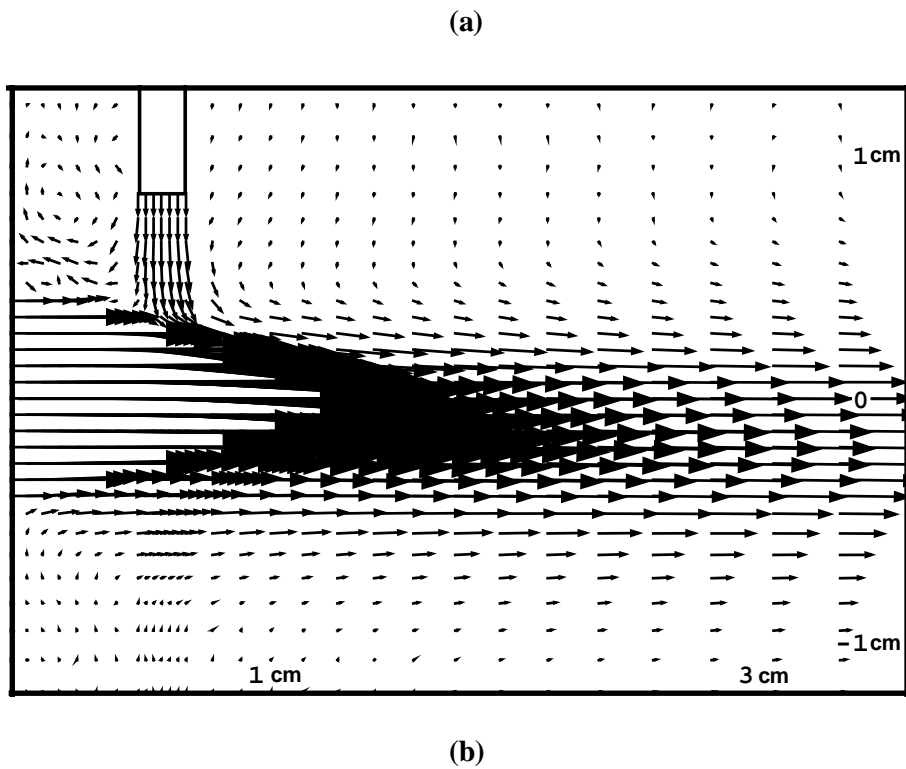
(b)

**Figure 5.7: Comparison of (a) gas temperature contours and (b) velocity vector at the ABCE plane (indicated in Fig. 1.1) with carrier gas flow rate of 4.5 slm and without carrier gas.**



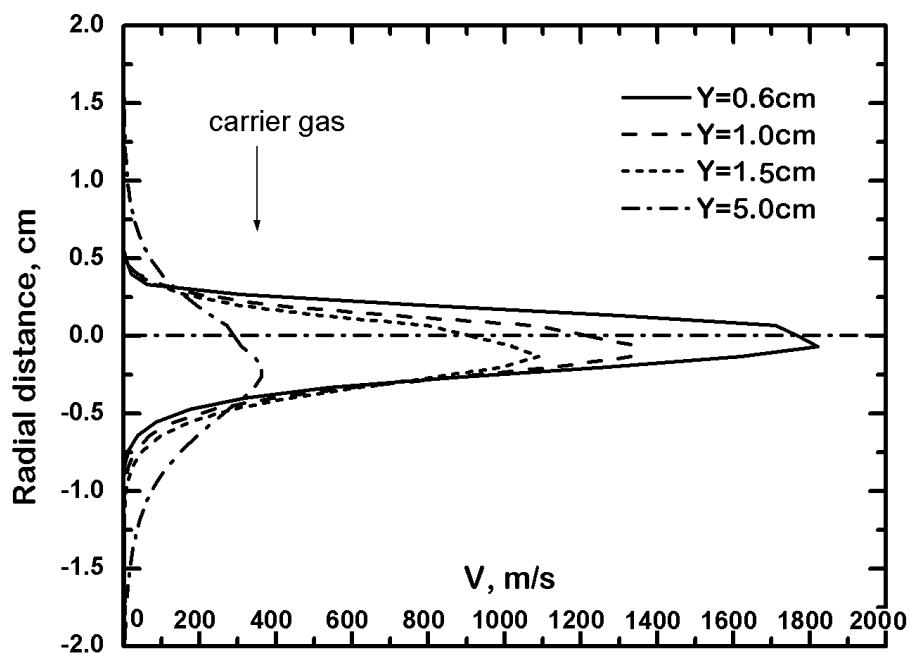
**Figure 5.8:** Temperature contour and gas velocity vector at the cross section S-S (see Fig. 1) near the injector with carrier gas flow rate of 3 slm.



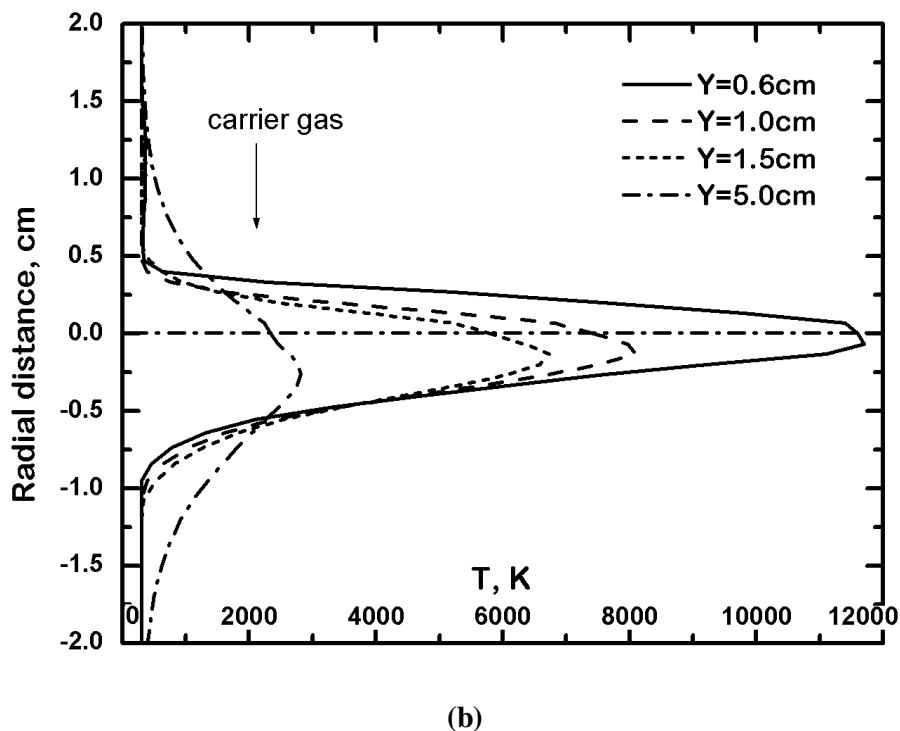


(b)

**Figure 5.9:** (a) Gas temperature contours and (b) velocity vector at the ABCE plane (indicated in Fig. 1.1) for carrier gas flow rate of 15 slm.



(a)



(b)

Figure 5.10: (a) Gas temperature profiles and (b) axial velocity profiles at the cross lines in the ABCE plane (lines parallel to AB or CE in Fig. 1.1) for carrier gas flow rate of 15 slm.

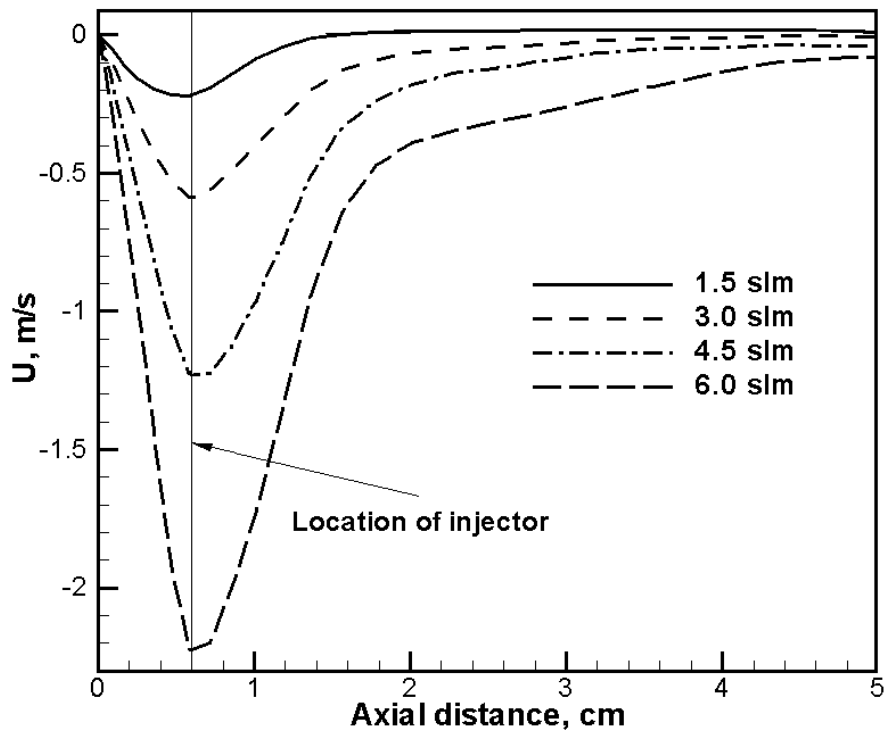
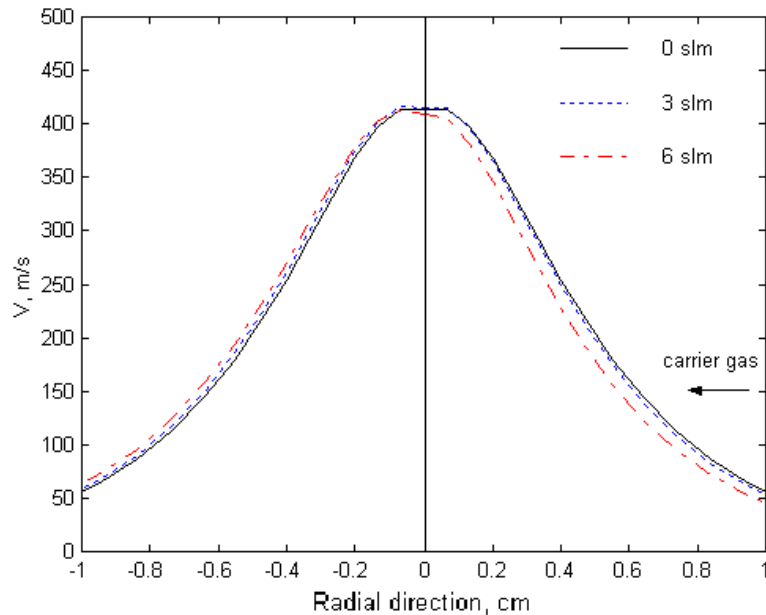
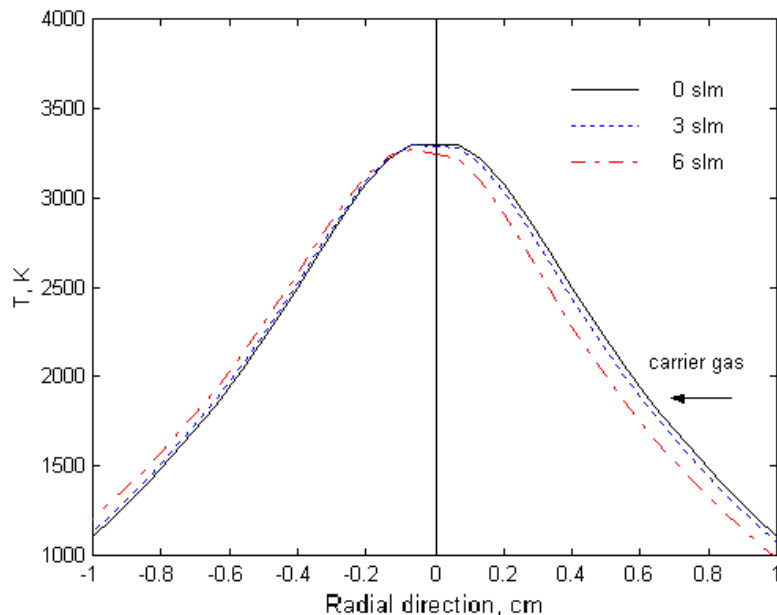


**Figure 5.11: Effects of carrier gas flow rate on gas radial velocity at the centerline of the plasma jet.**



**(a)**



**(b)**

**Figure 5.12: (a) Gas axial velocity and (b) temperature at the cross line away from nozzle 5 cm. The solid, dotted, and dash-dot lines are for cases without carrier gas and with carrier gas flow rates of 3 and 6 slm, respectively.**

### 5.4.2 Effects of multiple particles

The loading of multiple particles will also disturb the plasma jet flow, as a result of the two-way coupled particle-plasma interaction. With the injection of multiple particles, the temperature of the plasma jet decreases due to the energy transferred to the cold particles. Fig. 5.13 shows the temperature contours of the 3-D plasma jet with multiple particles injected. The molybdenum particles with diameters of  $4 \sim 60 \mu\text{m}$  are injected at  $x=0.8 \text{ cm}$ ,  $y=0.6 \text{ cm}$  with the feeding rate of  $0.5 \text{ g/s}$  at the time of  $6.0 \text{ ms}$  when the 3D plasma jet reaches the steady state. The carrier gas flow rate for this case is  $6 \text{ slm}$ . Figure 5.14, Fig. 5.15 and Fig. 5.16 show the gas radial and axial velocities, and temperature, respectively before and after particles being fed for  $2 \text{ ms}$  at the spray distance of  $y = 0.6, 1.1, 1.6, 5 \text{ and } 10 \text{ cm}$ . The solid and dashed lines represent the results just before and after particle injection for  $2 \text{ ms}$ , respectively. They show the decrease in temperature and axial velocity of the plasma jet after particle injection, indicating the influence of multi-particles in plasma jet. Same results are obtained for zirconia particles. Dashed lines in Fig. 5.17, representing the axial velocity and temperature after zirconia particle injection for  $2 \text{ ms}$  at feeding rate of  $1.5 \text{ g/s}$ , show the decrease in temperature and axial velocity of the plasma jet after particle injection, indicating the influence of multi-particles in plasma jet.

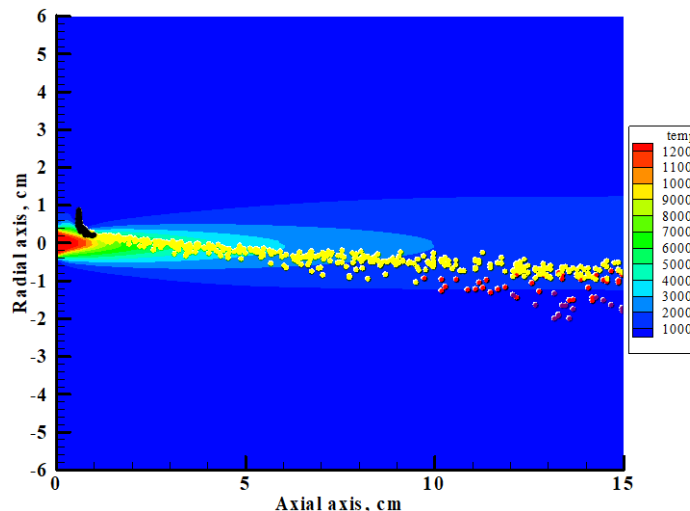


**Figure 5.13: Temperature contour of 3D plasma jet flow with multiple Mo particles injected along with carrier gas of argon.**

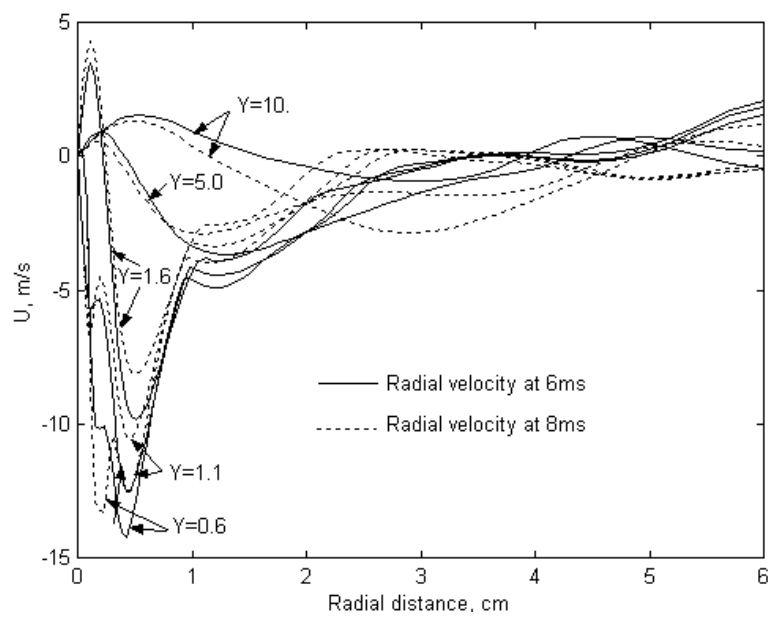


**Figure 5.14: Radial velocities at cross lines of the flow field before and after multiple Mo particles injected.**

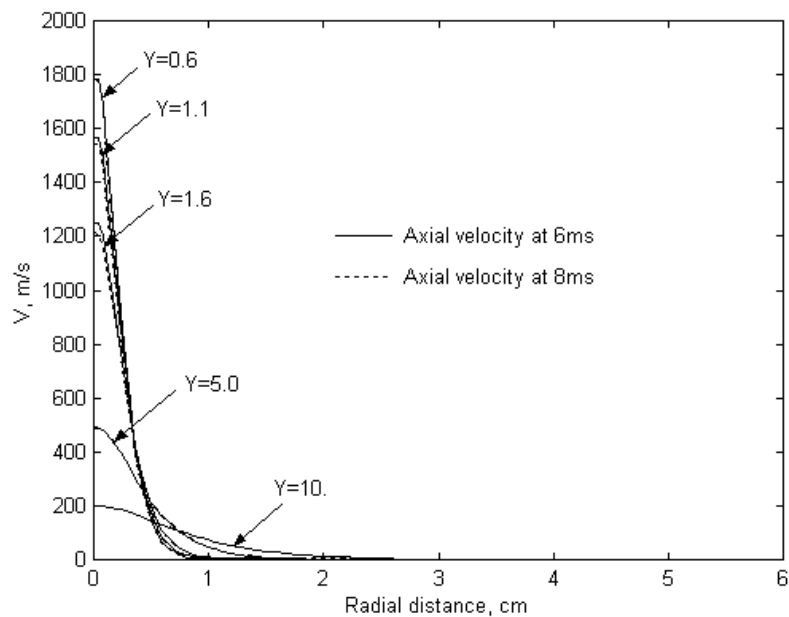


**Figure 5.15: Axial velocities at cross lines of the flow field before and after multiple Mo particles injected.**

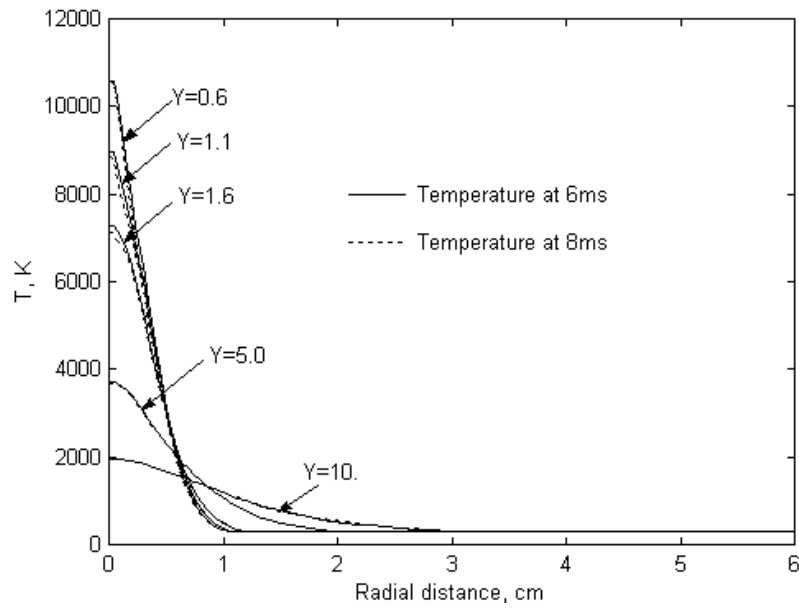
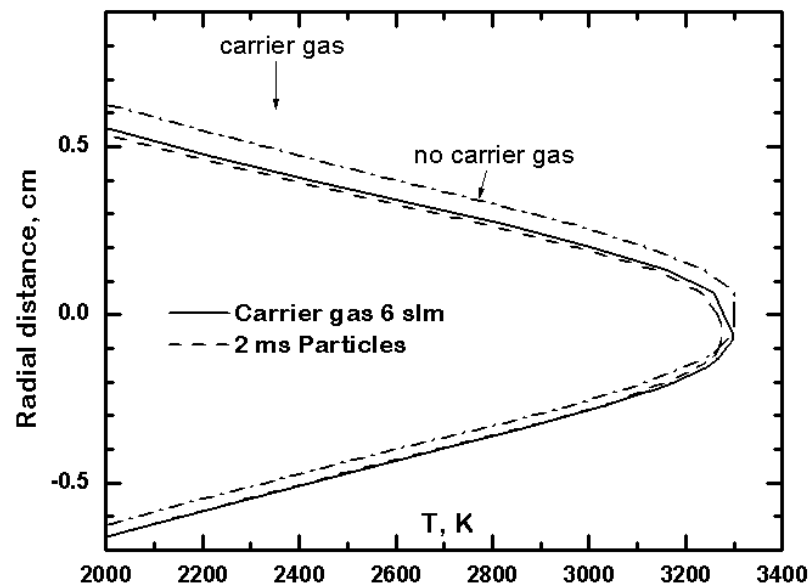
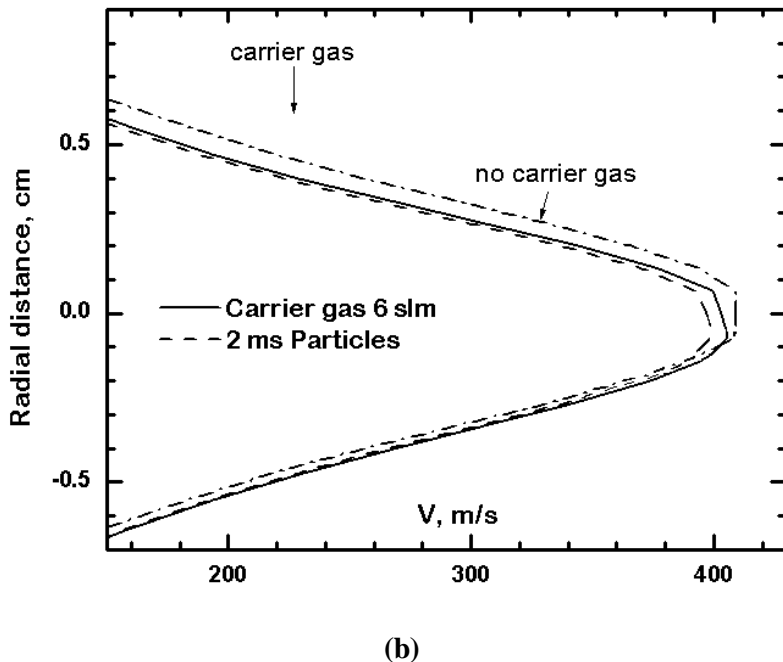


**Figure 5.16: Temperature at cross lines of the flow field before and after multiple Mo particles injected.**



(a)



(b)

**Figure 5.17:** (a) The gas axial velocity and (b) temperature at the cross line away from nozzle 5 cm.

The solid, dash, and dash-dot lines are for cases with carrier gas of 6 slm, and then with  $\text{ZrO}_2$  particles injection, and without carrier gas respectively.

## 5.5 Results of particle behavior

### 5.5.1 Comparison of single particle behavior in 2D and 3D plasma jet

Comparison of single particle behavior in 2D and 3D plasma jet is shown in Fig. 5.18, Fig. 5.19 and Fig. 5.20. The operating conditions, including particle diameter and initial injection velocity, are all the same for these two cases. The only difference is that the 2D case is axisymmetric plasma jet without carrier gas, while the 3D case calculates the carrier gas of 3 slm Ar. The low deposition location, high radial velocity, low axial velocity and temperature are observed for the particle in 3D plasma jet. These effects of carrier gas on the particle behavior can be contributed in two aspects: one is the change of the fluid pattern downstream of the injector will increase the particle traverse velocity and help it penetrate into the plasma jet; the other part is due to cooling and slowing effects of carrier gas on the plasma jet.

As a result of carrier gas, spray pattern of multiple particles will also be different after considering the carrier gas injection, which can be seen in Fig. 5.21, Fig. 5.22 and Fig. 5.23. Again, lower deposition location, lower average particle velocity and temperature are observed in 3D case. In Fig. 5.23, the higher particle temperature is observed in the center of the spray area, because more small particles are entrained in the hot core of plasma jet under the help of carrier gas effects.

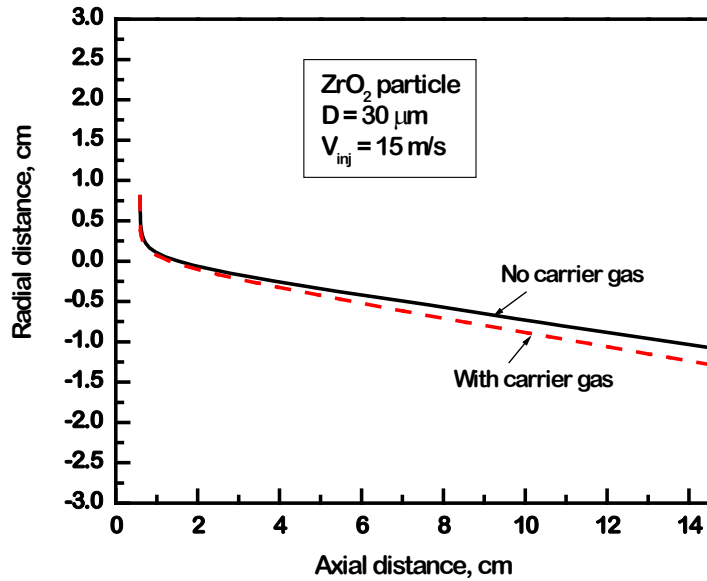


**Figure 5.18:  $\text{ZrO}_2$  Particle trajectories with and without carrier gas effects.**

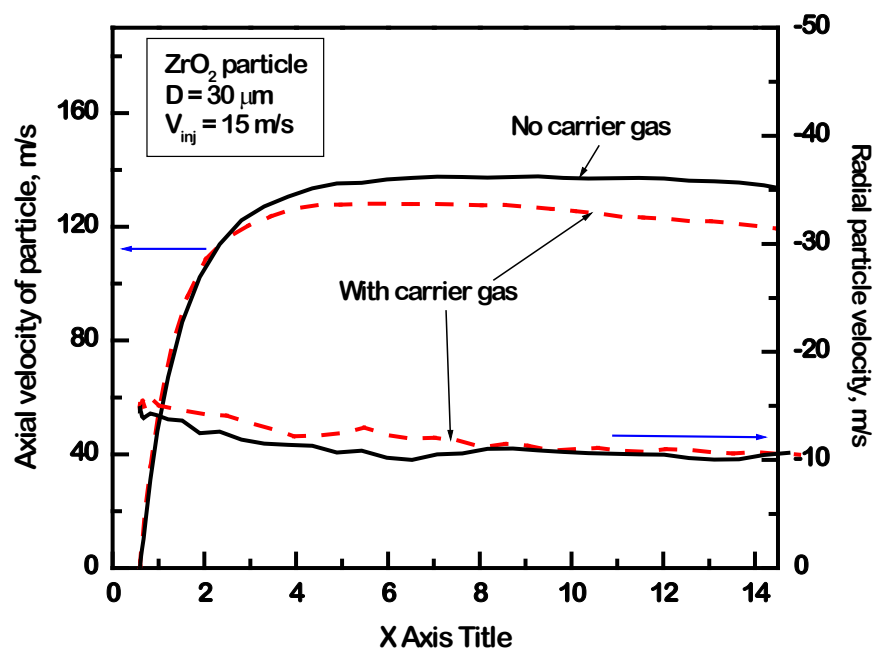


Figure 5.19:  $\text{ZrO}_2$  Particle velocities with and without carrier gas effects.

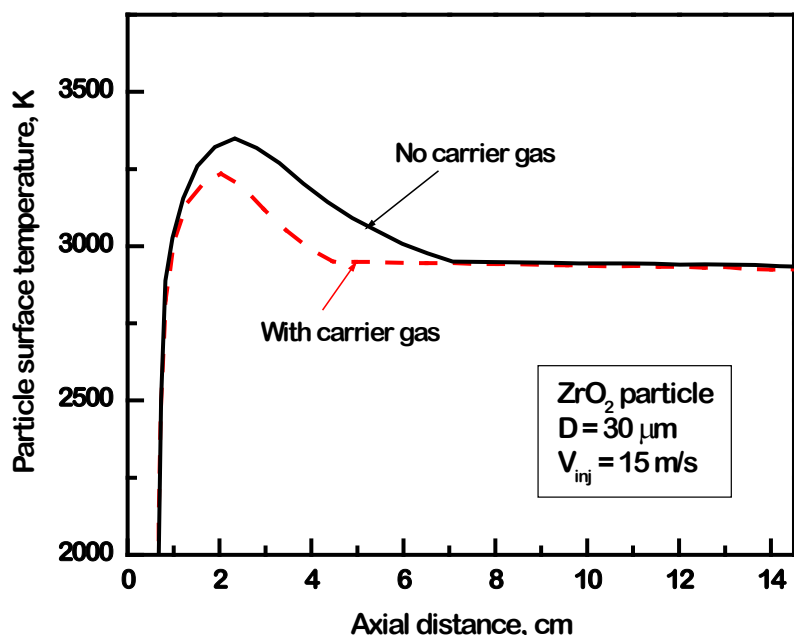
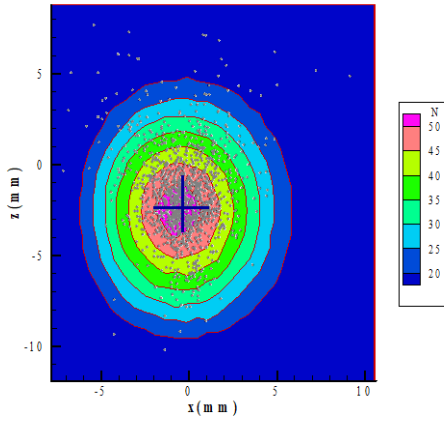
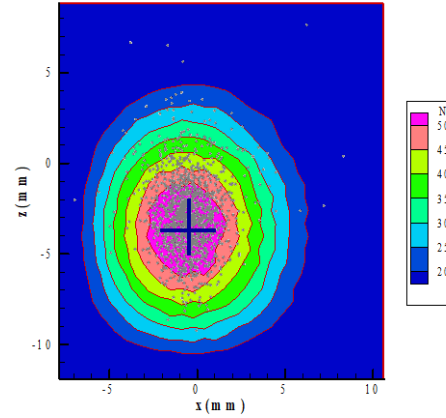


Figure 5.20:  $\text{ZrO}_2$  Particle temperatures with and without carrier gas effects.

Particle deposition location w/o carrier gas

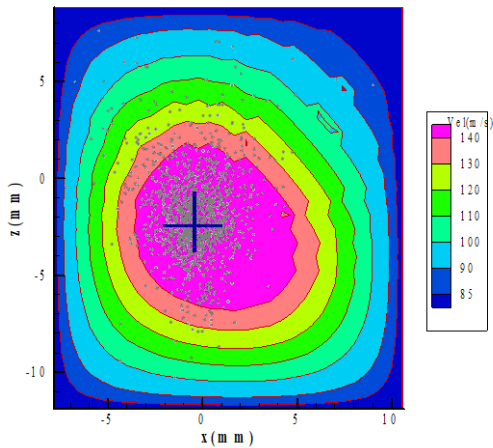


Particle deposition location with carrier gas



**Figure 5.21: Deposition location of ZrO<sub>2</sub> Particles with and without carrier gas of Ar 3 slm.**

Particle velocity w/o carrier gas



Particle velocity with carrier gas

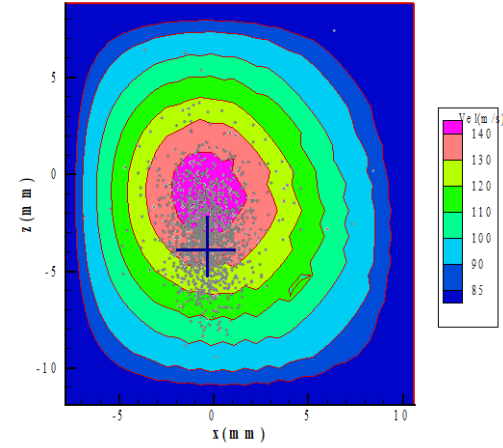


**Figure 5.22: Velocity of ZrO<sub>2</sub> Particles with and without carrier gas of Ar 3 slm.**

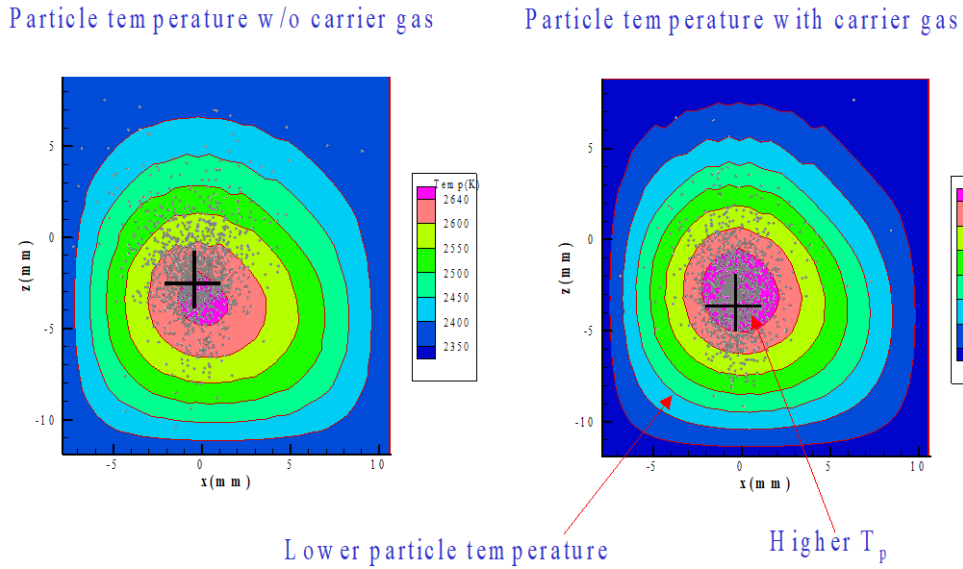


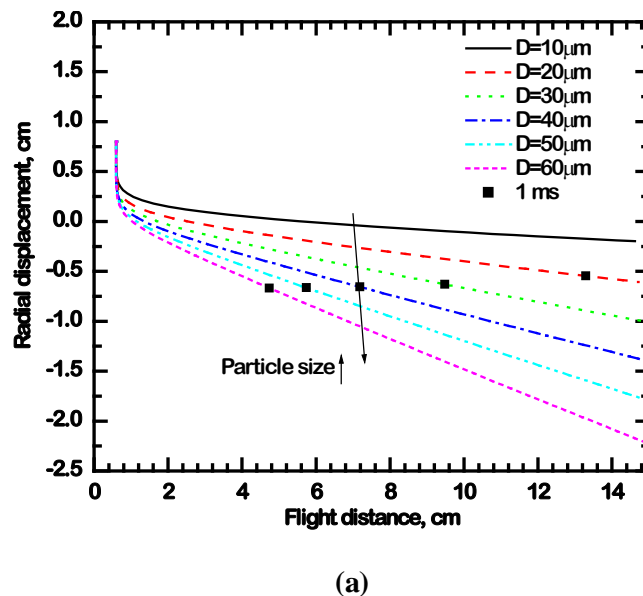
**Figure 5.23: Surface temperature of  $\text{ZrO}_2$  Particles with and without carrier gas of Ar 3 slm.**

### 5.5.2 Effects of particle size

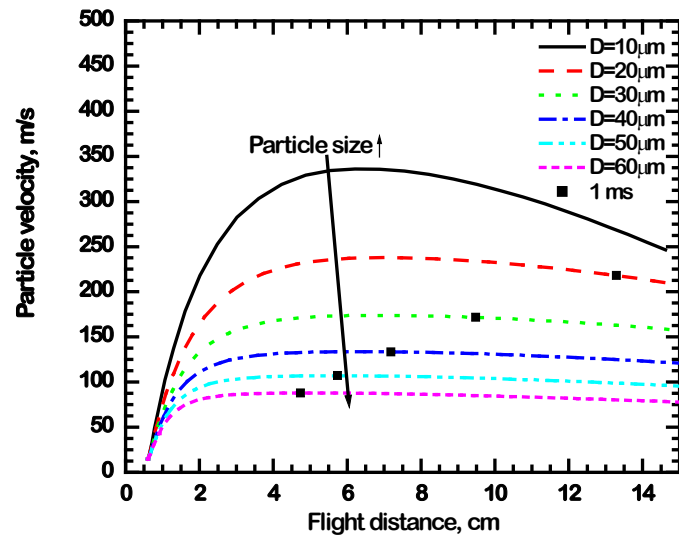
Since particle has different behavior after considering carrier gas effects, we performed the study of the single particle with different sizes in LAVA-P-3D. The simulation results for  $\text{ZrO}_2$  and Mo particles with different size are shown in Figs. 5.24 and Fig. 5.25 respectively. The particle size plays an important role on particle trajectory, melting, acceleration, evaporation and oxidation. From the results, we can see that larger particles traverse further away in the powder injection direction from the plasma central axis, and have lower velocity than smaller ones. Smaller particles display superheating while larger particles just reach the melting point with some of them only partially melted and/or re-solidified, e.g. most  $\text{ZrO}_2$  particles larger than 40  $\mu\text{m}$  under current heating condition. One reason is that the larger particle has higher total heat capacity and requires more time to be heated. Second reason is that the larger particles deviate from central axis of plasma jet, and travel quickly away from the hottest core of plasma and enter the peripheral region with lower temperature gas cooled by entrained air. The larger the particle, the earlier it begins to cool down. And smaller particles cool more rapidly.

Evaporation occurs only in a short distance when the particles are heated up to the boiling point. For the same thermal environment, the evaporation rate for a small particle is larger than that of large particle, since a small particle can be heated up more easily and it also has large mass transfer coefficients.

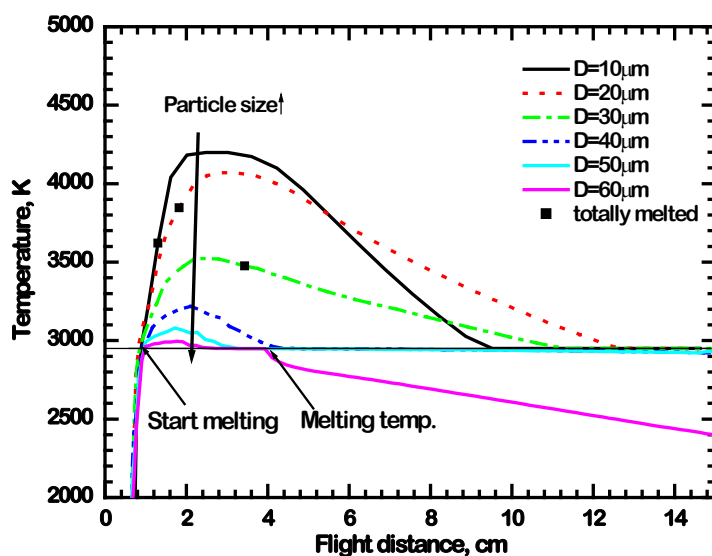
Results also show that the primary oxidation mechanism for in-flight Mo particle is the third mechanism: the adsorption of oxidant diffused from the gas to the surface when the particle is melted. Smaller particle has larger oxidation rate. One reason is that the small particle has higher oxygen concentration around it while passing through the hot core of plasma, because its trajectory is closer to the ambient air due to its less momentum to penetrate the core. The second and main reason is that small particle has much larger mass transfer rate due to its small size and relatively high temperature that results in high viscosity of plasma gas around the particle.



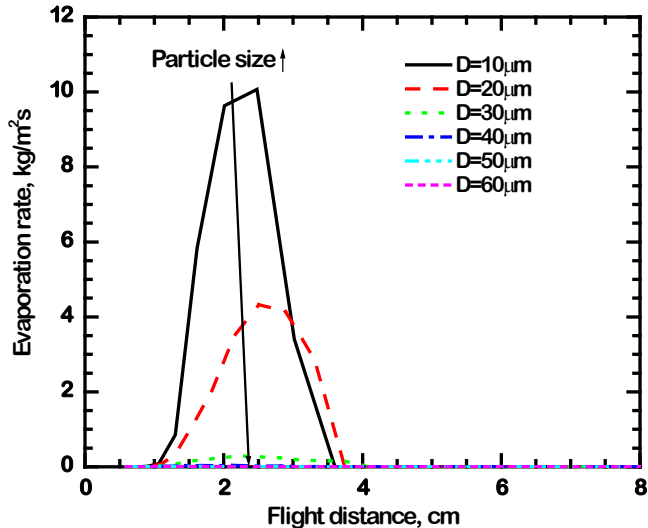
(a)



(b)

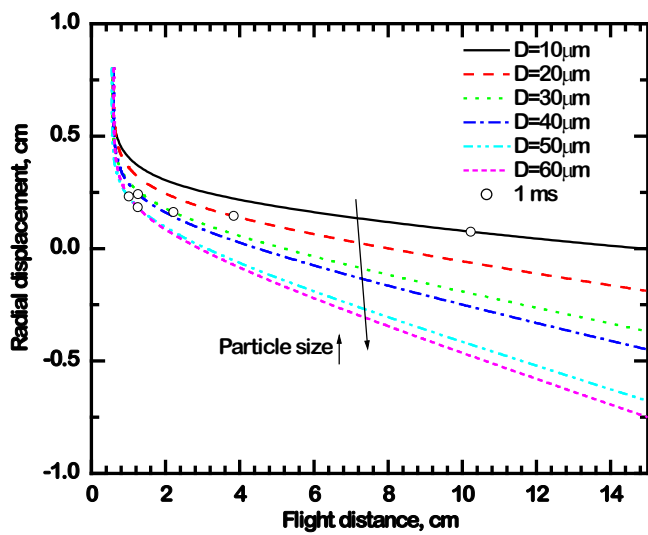


(c)

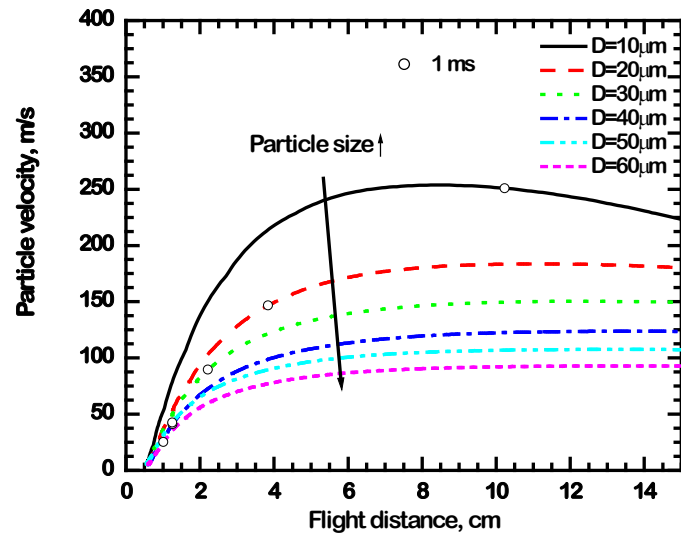


(d)

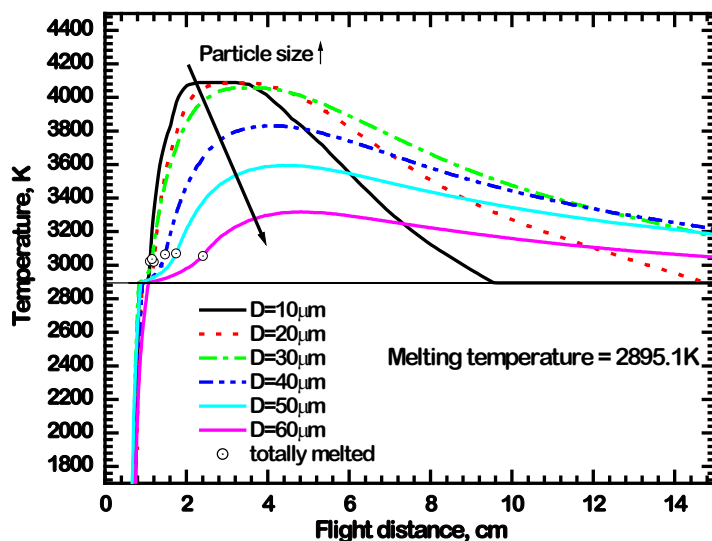
**Figure 5.24:** Effects of particle size on ZrO<sub>2</sub> particle behaviors: (a) trajectories, (b) velocity, (c) temperature, and (d) evaporation rate. The carrier gas flow rate is 6 slm.



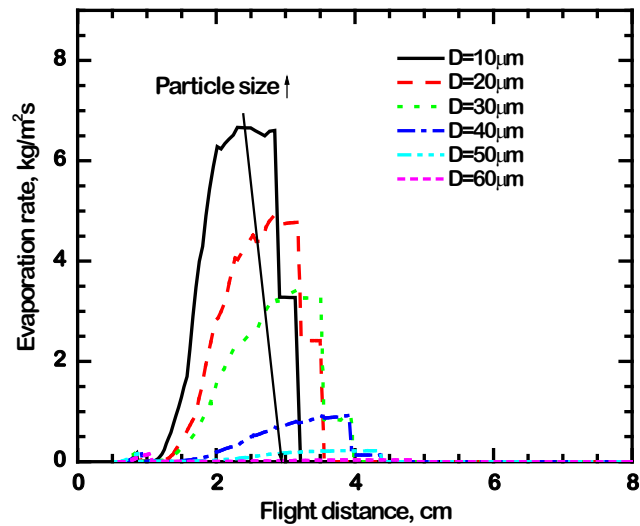
(a)



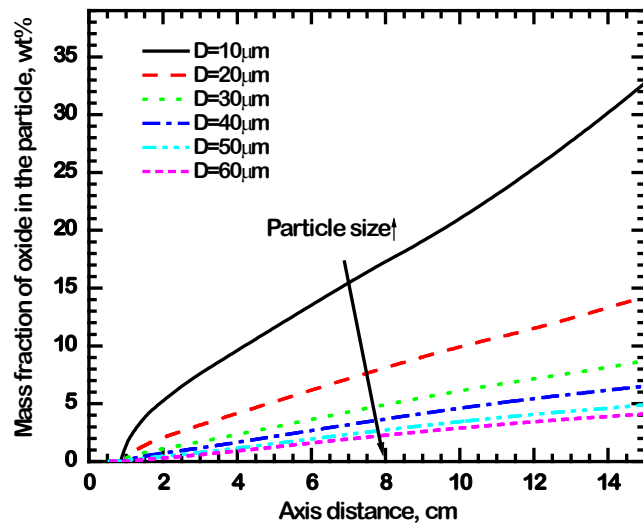
(b)



(c)



(d)



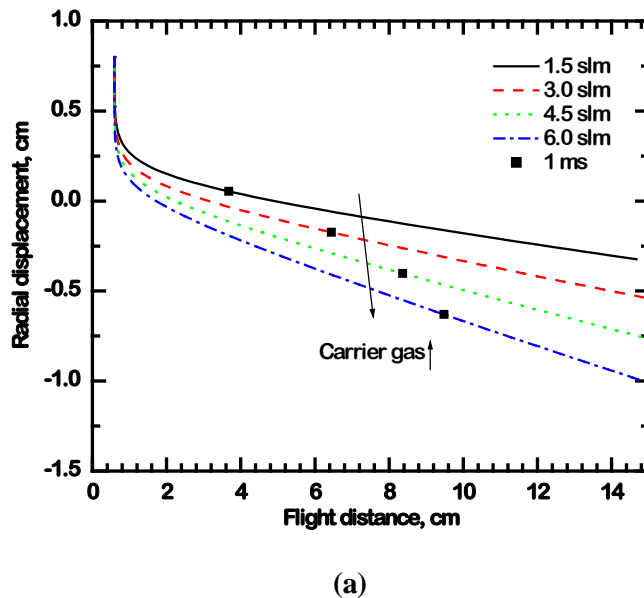
(e)

**Figure 5.25: Effects of particle size on Mo particle behaviors:** (a) trajectories, (b) velocity, (c) temperature, (d) evaporation rate and (e) oxide content. The carrier gas flow rate is 3 slm.

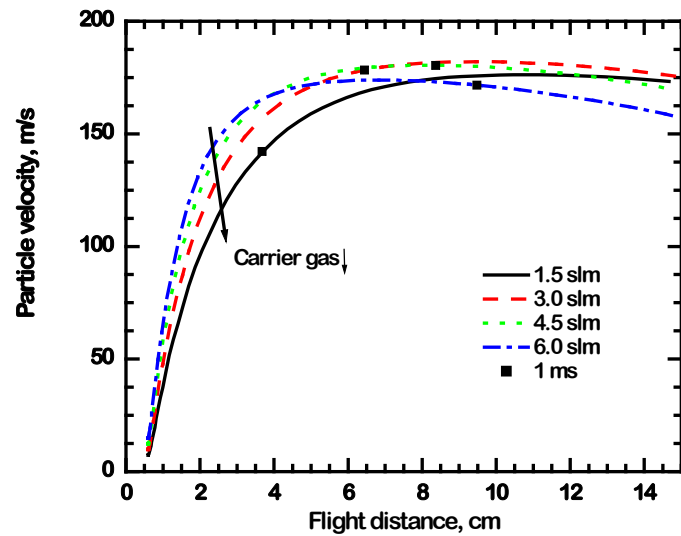
### 5.5.3 Effects of carrier gas flow rates

The effects of carrier gas flow rates on single particle behaviors are shown in Fig. 5.26. In the case of high carrier gas flow rate, the particle exhibits a higher traverse velocity and penetrates further down toward the plasma jet. Different particle velocity and temperature histories are obtained for the same size of  $\text{ZrO}_2$  particle with the diameter 30  $\mu\text{m}$ .

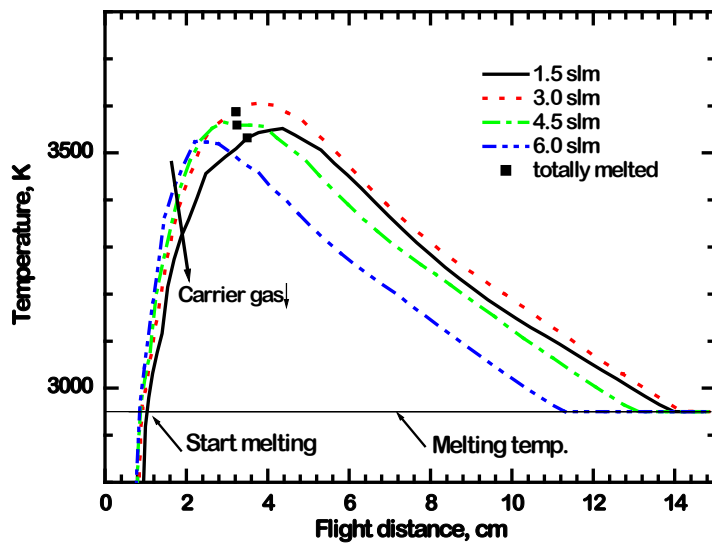
Figure 5.27 and Fig. 5.28 show the spray pattern of multiple particles at the spray distance 8 cm for carrier gas rates of 1.5 and 3 slm respectively. Although the injection statistical distribution is the same, e.g. average particle injection diameters of  $32.3 \pm 17.8 \mu\text{m}$  and  $32.4 \pm 17.5$  for the cases with carrier gas flow rate of 1.5 and 3 slm respectively, the spray pattern are significantly different. The average particle temperatures upon impact for these two cases are 2837 K and 2889 K, respectively, while velocity 169.5 m/s (1.5 slm) and 181.6 m/s (3 slm), respectively. We believed that for higher carrier gas flow rate, more small particles (20~30  $\mu\text{m}$ ) penetrate into the plasma jet and stay in the densest area on the deposition substrate, and their high velocity and high temperature contribute to the higher average particle velocity and temperature for the case with carrier gas flow rate of 3 slm.



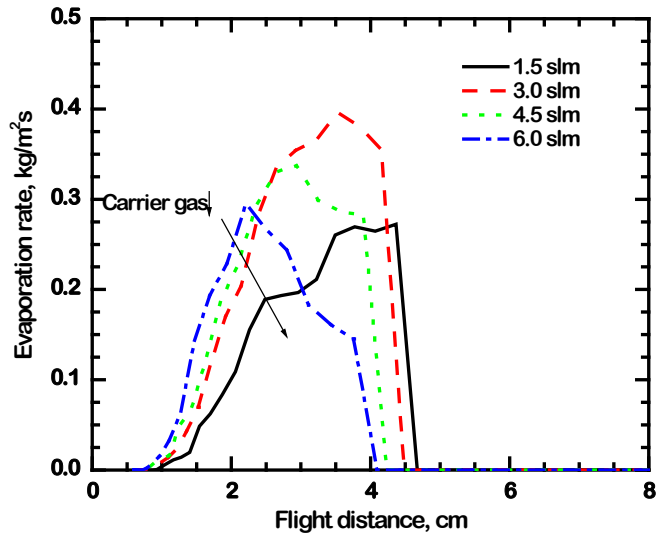
(a)



(b)

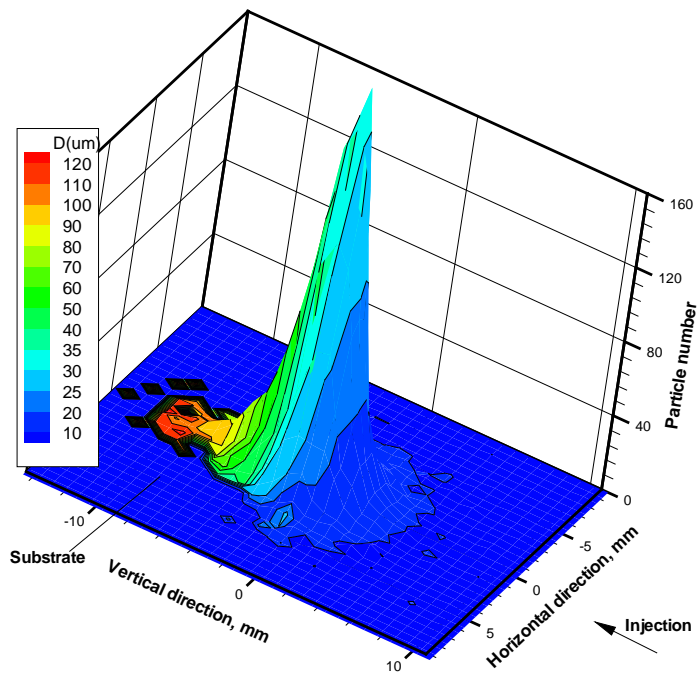


(c)



(d)

**Figure 5.26: Effects of carrier gas flow rate on ZrO<sub>2</sub> particle behaviors:** (a) trajectories, (b) velocity, (c) temperature, and (d) evaporation rate.



(a)

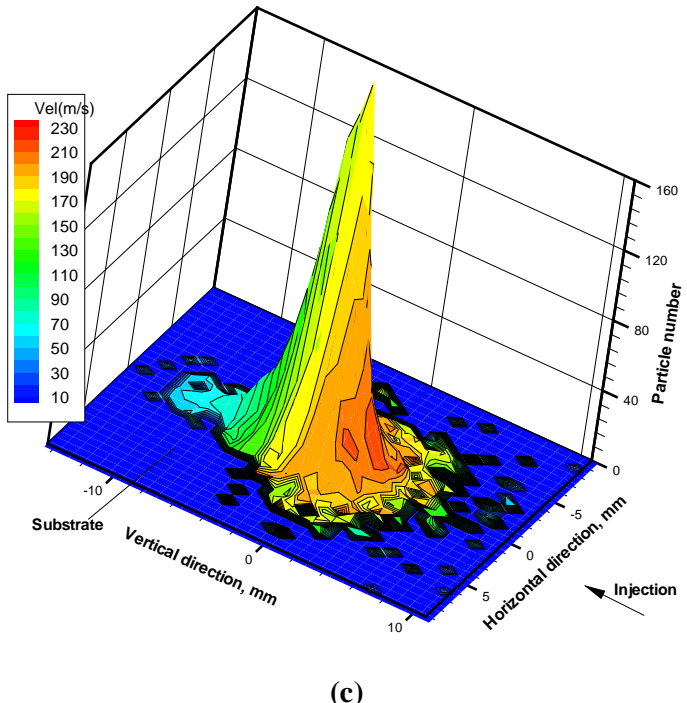
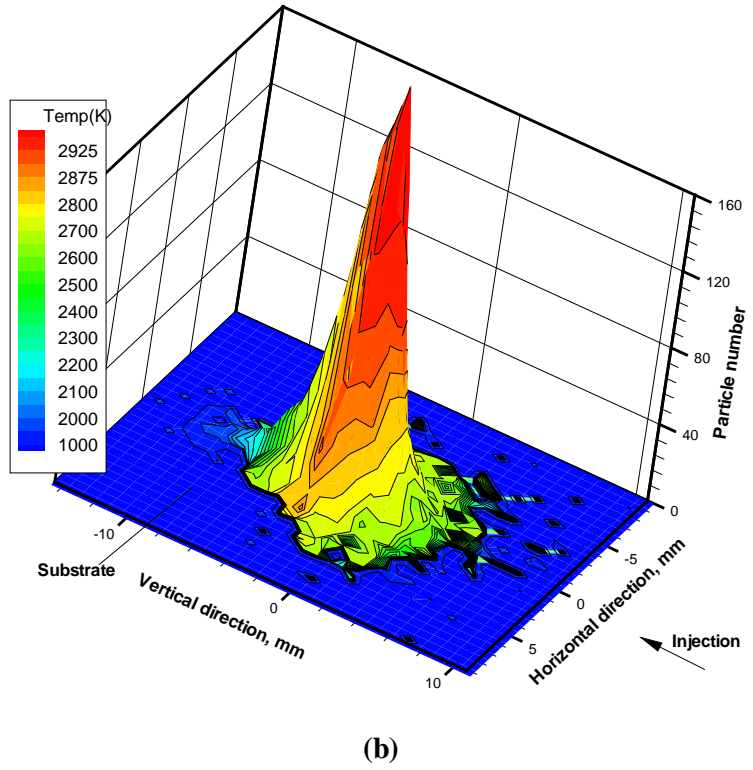
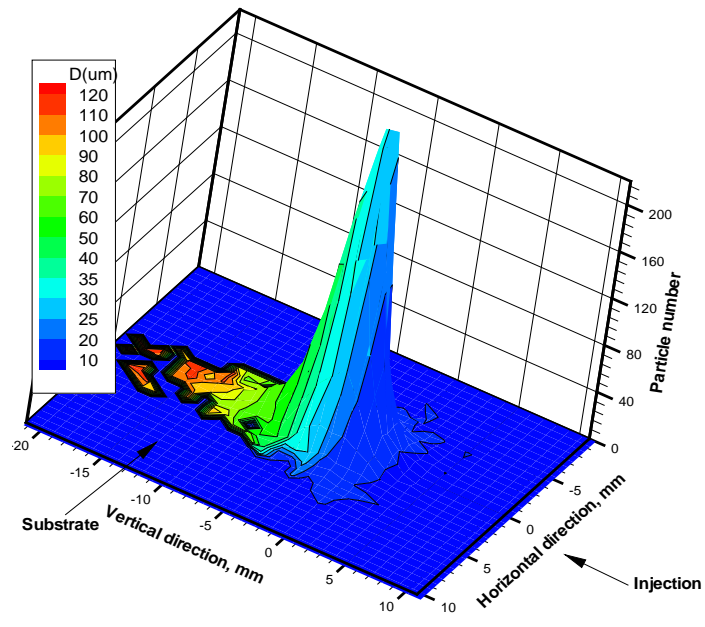
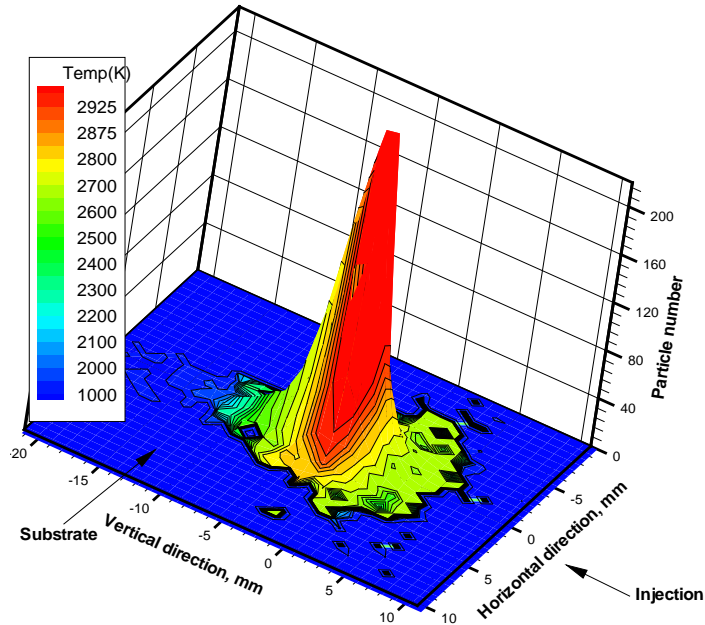


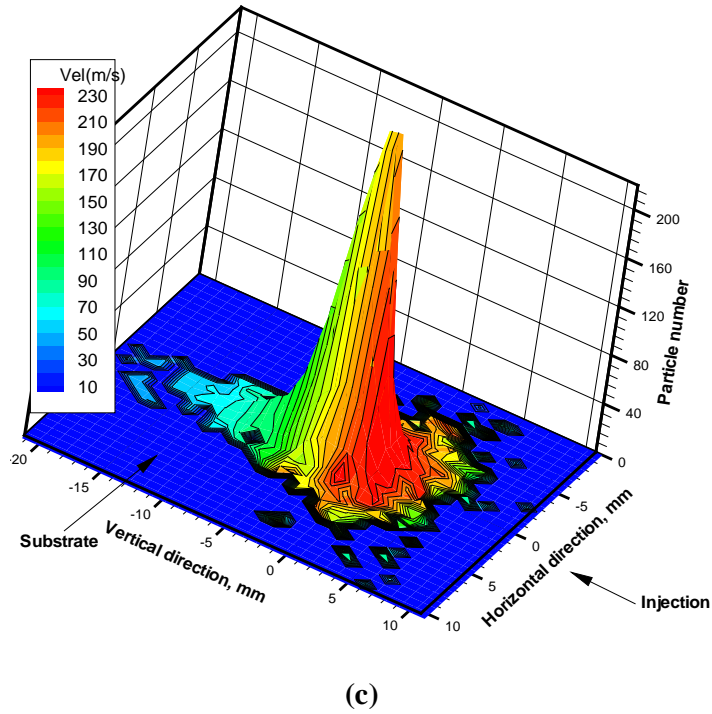
**Figure 5.27: (a) Diameter, (b) temperature and (c) velocity distributions of multiple  $\text{ZrO}_2$  particles on the substrate. The carrier gas flow rate is 1.5 slm.**



(a)



(b)



(c)

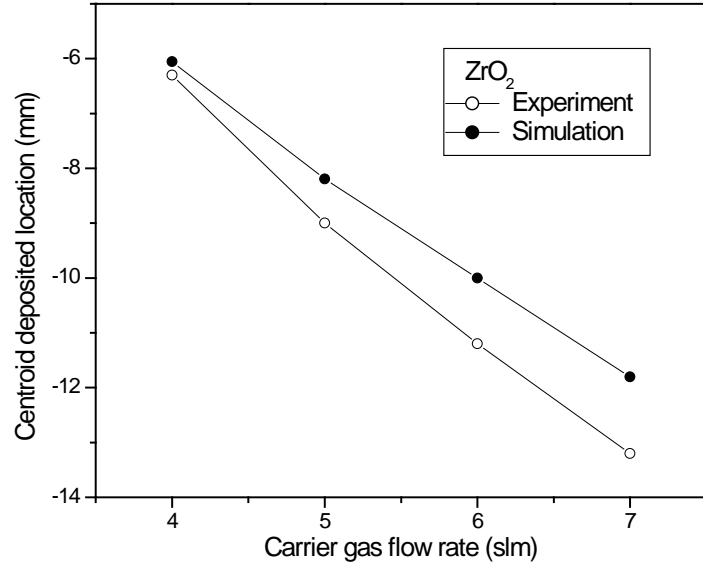
**Figure 5.28: (a) Diameter, (b) temperature and (c) velocity distributions of multiple  $\text{ZrO}_2$  particles on the substrate. The carrier gas flow rate is 3 slm.**

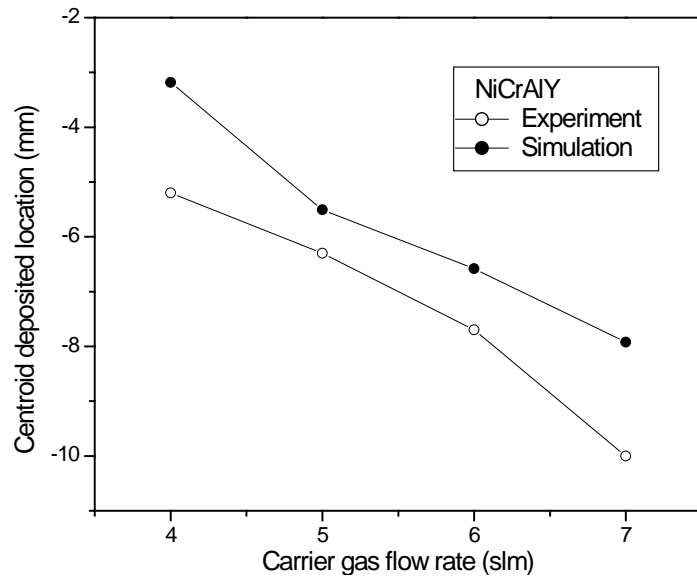
#### 5.5.4 Multiple particle spray pattern and the comparison with experiments

The multiple particle spray pattern has also been studied under different carrier gas flow rates, with concerns of pixel deposition position and spray width of the particles upon impact. Pixel position, or centroid position is the peak of the particle radial distribution. Spray width is defined as the width of the spatial distribution of particles with particle number intensities greater than 10% of the maximum intensity observed at the pixel position of spray pattern. The pixel position and spray width from experiment and simulation are shown in Figs. 5.29(a) and 5.29(b) for NiCrAlY and  $\text{ZrO}_2$  particles, respectively with spray distance of 10 cm. For both the NiCrAlY and  $\text{ZrO}_2$  particles, the spray pattern pixel position decreases with carrier gas increase, and the spray width monotonically increases.

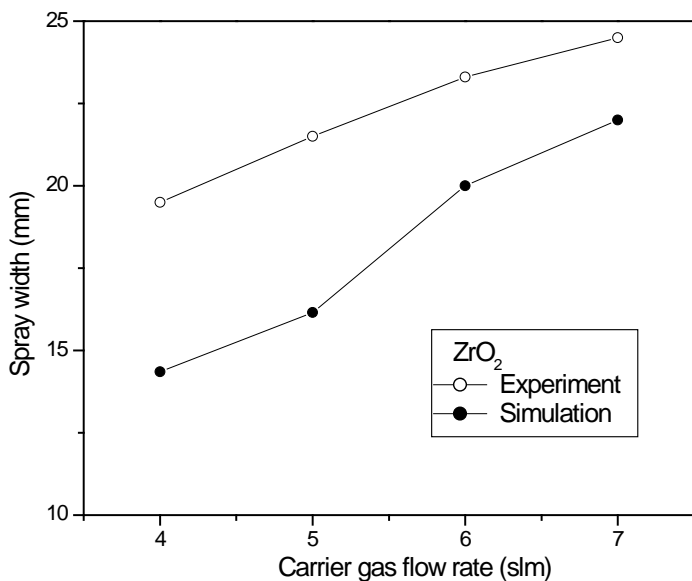
The average particle velocity and temperature for different carrier gas flow rates are also investigated. Since IPP measures a large number of particles simultaneously based on their radiance, and

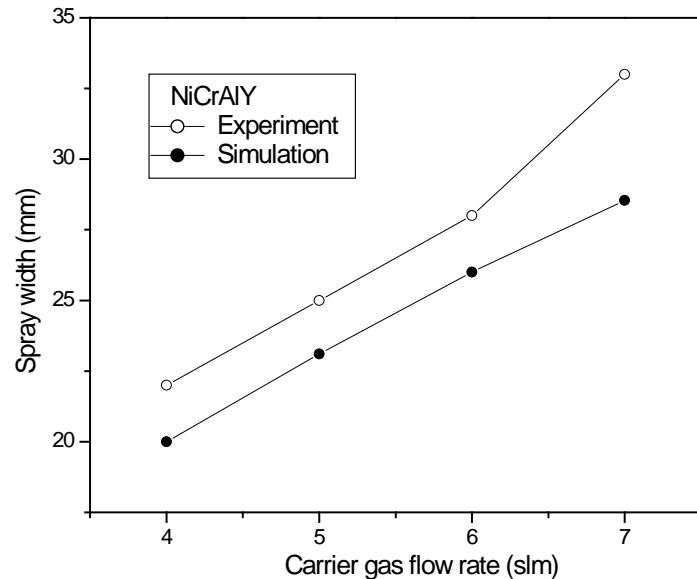
yields an estimated mean particle temperature. This ensemble temperature is related to the distribution of particle size and temperature. As particle radiance is approximately proportional to particle surface area and particle temperature's fourth power, the simulated averaged particle temperature is also weighted by  $D_P^2$  and  $T_P^4$ . The effects of carrier gas flow rates on the average particle temperature and velocity at the spray distance of 10 cm are depicted in Figs. 5.30(a)-(c). Both experiment and simulation show that the particle temperature is not so sensitive to carrier gas, with difference range within 100 K, although the spray pattern is greatly changed. Simulation data also show that the average particle velocities, which are algebraic average based on all the particles collected, vary in a short range of 10 m/s for the carrier gas flow rates ranging from 4 to 7 slm. Compared with experimental data (see Figs. 5.29 and 5.30), the simulation results fit well with the experiment, except that the spray width is less than experiment. Noted that in the simulation, we did not consider the fluctuation of arc root within the anode. In fact, the fluctuation of arc root causes the fluctuations of spray particles and thus a wider distribution of particle trajectories, velocities and temperatures upon impact. Therefore a smaller spray width from prediction is expected without considering arc fluctuation.





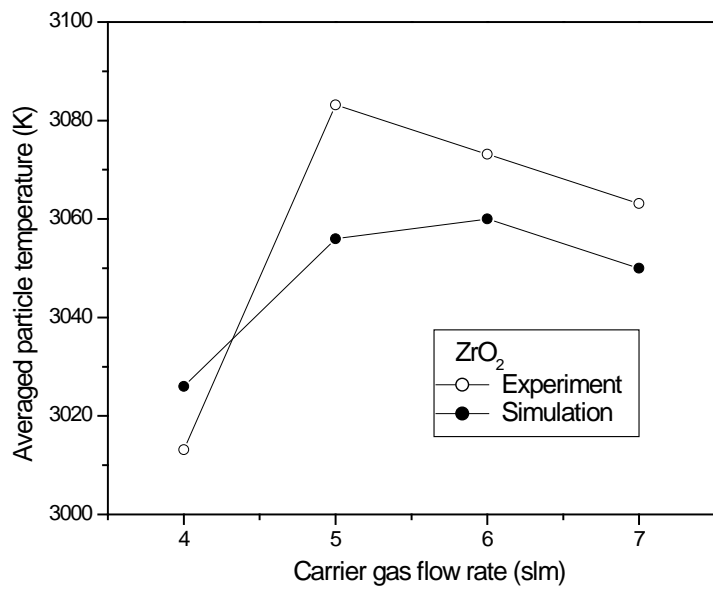
(a)

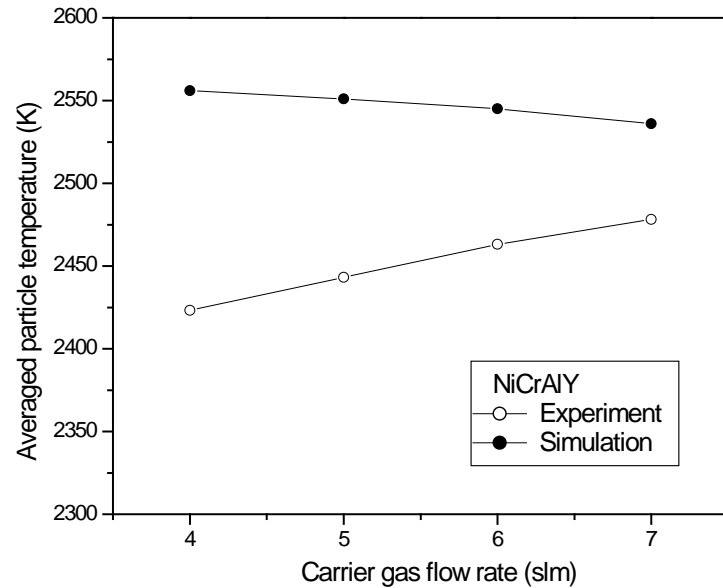




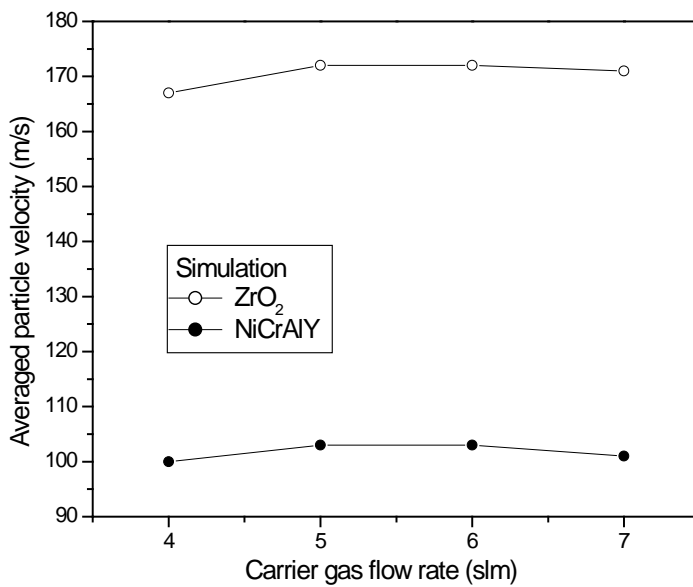
(b)

**Figure 5.29:** (a) Spray pattern centroid position and (b) width for  $\text{ZrO}_2$  and NiCrAlY as a function of carrier gas flow rate.





(a)



(b)

**Figure 5.30:** (a) Average particle temperature and (b) velocity for ZrO<sub>2</sub> and NiCrAlY as a function of carrier gas flow rate.

### **5.5.5 Statistical distribution of particle size, velocity and temperature**

This statistical distribution of particle size, velocity and temperature on the substrate is of great concern for coating quality control. In order to predict the size, velocity and temperature distributions, numerical simulations are performed using the stochastic scheme of multiple particle generation as detailed in Section 4.2. The case with operation conditions as listed in Table 5.1 is calculated, and ZrO<sub>2</sub> particles with the diameters ranging from 10 to 60 μm are studied. The simulation results are presented in Fig. 5.31 and Fig. 32 for different spray distances of 8 and 10 cm. The results show that the particle size distribution does not change significantly at different spray distances. Particle velocity increases a little when traveling from 8 cm to 10 cm, while the particle surface temperature decreases due to the particle cooling, with the average particle temperature of 3370 K and 3277 K at spray distance of 8 and 10 cm, respectively. It is also noted that at the spray distance of 8 cm, about 400 large particles with diameter of 50 ~ 60 μm are still in melting process, which result in the first peak of the particle temperature distribution at melting point, 2950 K. At the spray distance of 10 cm, this peak is smaller with 200 large particles in melting.

The particle size has great effects on the particle velocity and temperature distributions. Figure 5.33 shows the contributions of small particles with diameters less than 25 μm and large particles with diameters larger than 38 μm on the particle velocity and temperature distributions. Obviously, the small particles have large velocities. The effects of particle size on the particle temperature distributions are complicated by the cooling stages of the particles. As shown in Fig. 5.33 (b), the small particles have high temperatures at spray distance of 6 cm; while at spray distance of 15 cm, these particles are cooled rapidly and have low temperature distribution.

In order to eliminate the particle size effects, the numerical simulations are also conducted for the single size particles. Figure 5.34(a) shows the particle surface temperature distribution for ZrO<sub>2</sub> particles with diameter of 50 μm. The melting peak in the melting temperature can be eliminated if the particle

enthalpy is plotted instead of particle temperature, as shown in Fig. 5.34(b). The particle enthalpy is calculated as:

$$E = m_p \bar{C}_p T_p + f m_p L_m, \quad (5.1)$$

where  $\bar{C}_p$  is the averaged particle heat capacity,  $f$  is the melt fraction. When the particle is totally melted ( $f=1$ ),  $\bar{C}_p$  equals to the liquid heat capacity; while for the solid particle ( $f=0$ ),  $\bar{C}_p$  equals to the solid heat capacity.

The experiments are also conducted and the temperature distribution is measured. Experimental results for plasma densified particles with averaged size of 39  $\mu\text{m}$  is illustrated in Fig. 5.35. The results show that a particle temperature peak occurs around the melting point of 2677°C, due to the large latent heat fusion. Large particles have low temperature and results in the peak at 2500°C. The third peak at the high temperature (2850°C in this case) may be caused by the small and media size particles with highest temperature.

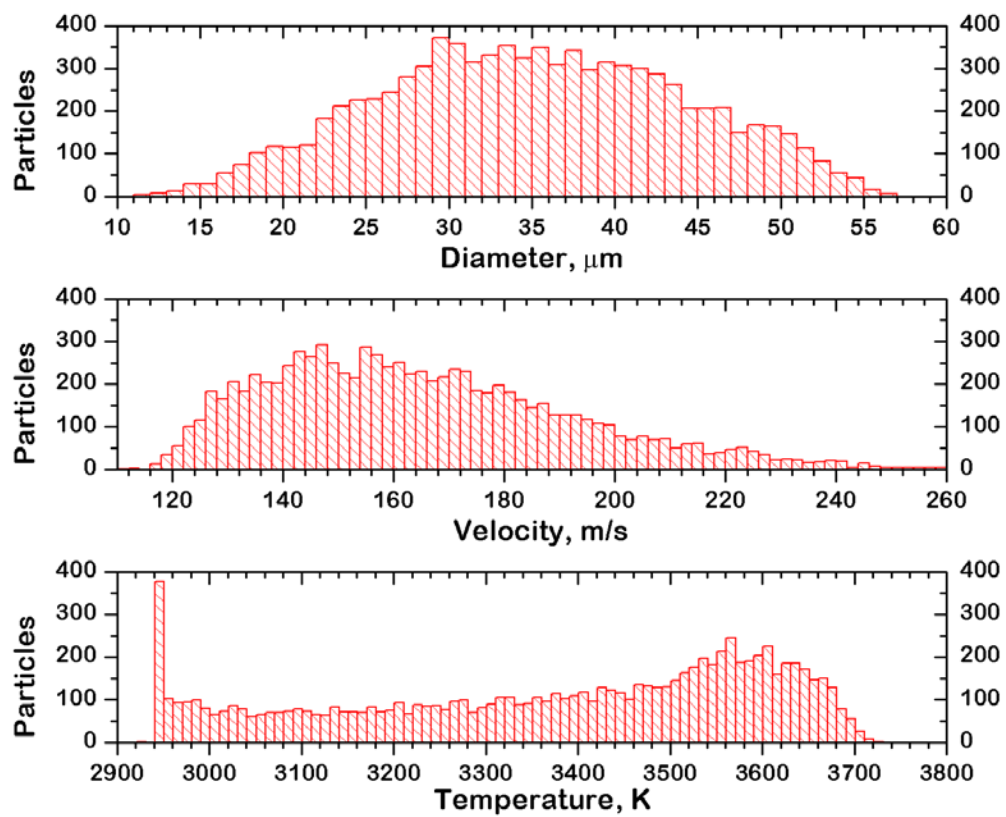


**Figure 5.31: Histograms for particle size, velocity and temperature of  $\text{ZrO}_2$  particles with diameter of 10~60  $\mu\text{m}$  at the spray distance of 8 cm.**

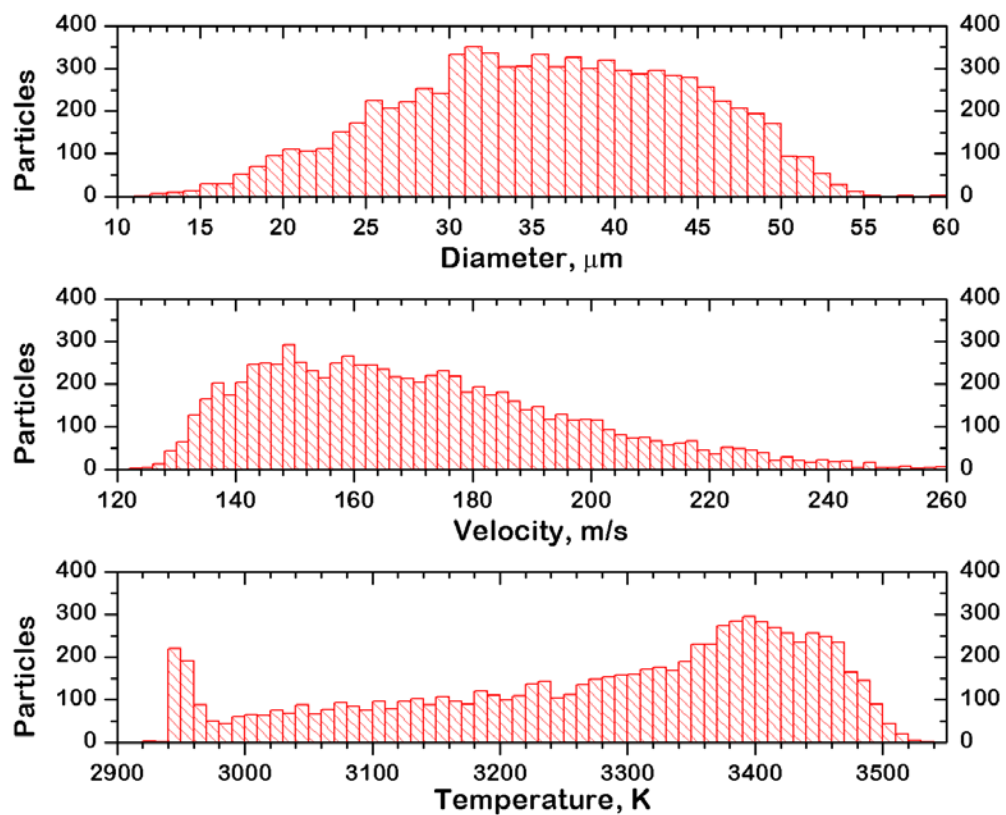


**Figure 5.32: Histograms for particle size, velocity and temperature of  $\text{ZrO}_2$  particles with diameter of 10~60  $\mu\text{m}$  at the spray distance of 10 cm.**

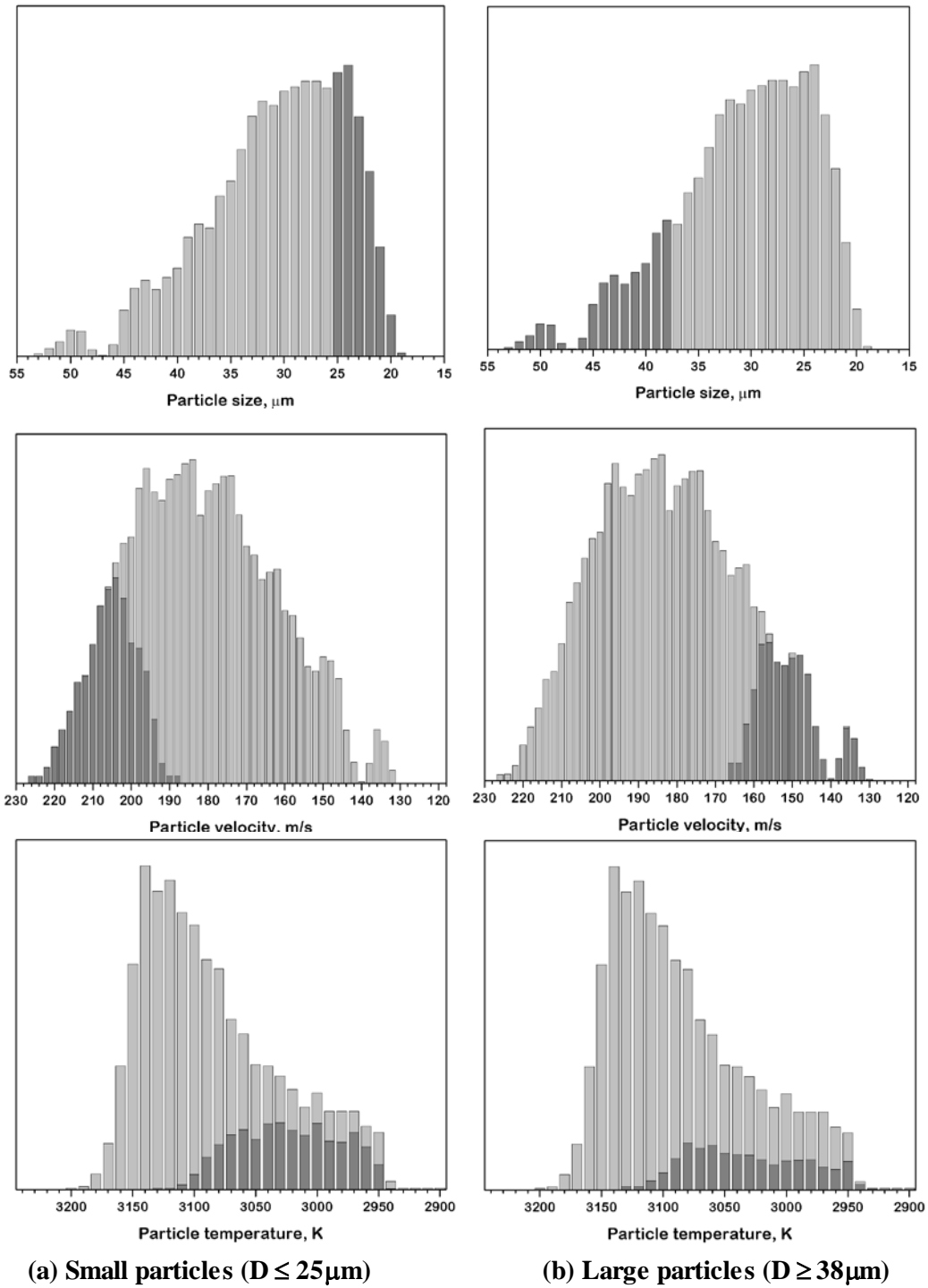
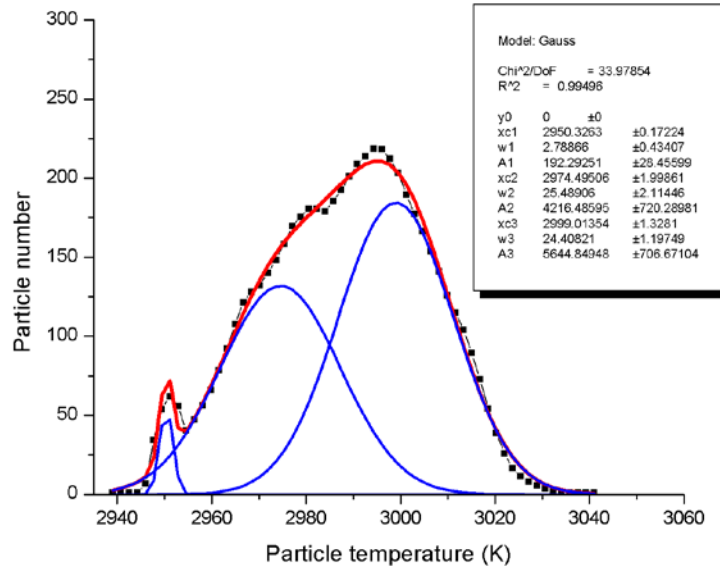
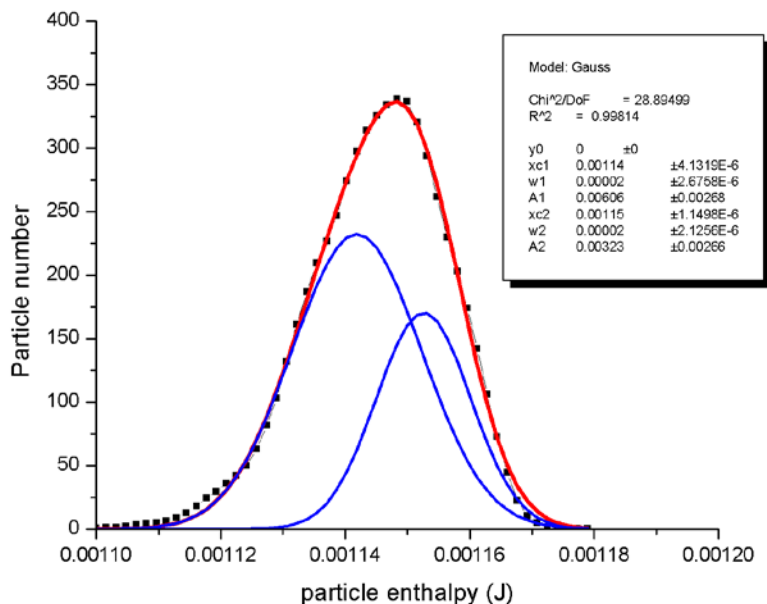


**Figure 5.33: Histograms for particle size, velocity and temperature of  $\text{ZrO}_2$  particles with diameter of 10~60  $\mu\text{m}$  at the spray distance of 15 cm (light gray), with the dark gray histograms indicating the distributions of specified size particles: (a) small particles and (b) large particles.**



(a)



(b)

**Figure 5.34: Distributions of (a) particle temperature and (b) particle enthalpy at spray distance of 8 cm for the  $\text{ZrO}_2$  particles with diameter of 50  $\mu\text{m}$ .**

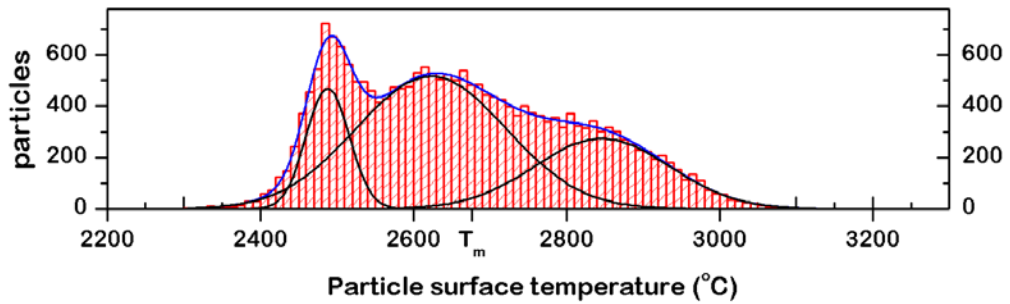


Figure 5.35: Experimental result of  $\text{ZrO}_2$  particle temperature distributions.

## **Chapter 6 Melting Index and Simulation Guided Diagnostic of Particle Behavior**

The particle melting status has great influence on the splat formation and coating properties. A thermal network analysis is employed in this chapter to identify the particle melting status. A dimensionless number, melting index, is defined and correlated with the experimentally measurable parameters to estimate the melting fraction of the particles. Numerical results and experimental data are used to validate the melting index. Oxidation index is also derived from the mass transfer analysis and used to estimate the oxide content for the metal particles during in-flight.

### **6.1 Introduction**

Thermal spray is such a process in which a large amount of powders are injected into a hot flame jet, being heated and accelerated to the substrate. This process has been widely used to produce metallic and ceramic coatings. The particle motion and heating is of vital importance for process control and design, since the in-flight particle characteristics greatly influence the splat formation and coating properties. A number of models have been developed on this subject that requires considering many special effects under plasma conditions. However, most of these models used lumped thermal analysis and ignored the phenomena of mass transport and chemical reaction. Particle melting and oxidation behavior were not fully understood.

The melt fraction of the particles upon impact will affect the splat morphology and coating properties significantly, especially for low-thermal-conductivity materials, such as ceramic in thermal barrier coating (TBC). Although it has not fully proved theoretically, the role of partially melted particle in molten droplet spreading and solidification are expected to be in two folds [Zhang, 2003], the unmelted part may enhance the dissipation of the kinetic energy and thus slow down the spreading process; and the unmelted part may also bounce away from the substrate and then introduce the disturbance that favors particle splashing. Therefore, the presence of partially melted particle may result in a high fragmented splat, low deposition efficiency and high coating porosity.

The oxidation of atmospheric sprayed metal particles can also greatly influence the coating property and performance, which is detrimental for many applications [Volenik, 1999]. Such degradation may be caused by the unwanted physical and chemical properties of the oxides. For example, the brittleness and the thermal expansion coefficient of the oxide reduce the coating corrosive resistance; and the lower wettability of the oxide layer is responsible for the poor intersplat cohesion in the metal coatings. Therefore, a reliable description of the melting and oxidation behavior of the sprayed particle is essential to improve the understanding of the relationship between the in-flight particles characteristics and the coating properties; this will certainly help develop an effective control of the coating efficiency and quality.

Some research has been conducted to understand the in-flight particle melting in various thermal spray processes [He, 2001; Wan, 1999]. The effects of the melt fraction on the splat morphology, however, are not fully understood. Vaidya *et al.* [2001] conducted an experimental investigation of the splat morphology over a wide range of particle conditions. They defined a “melting index” to indicate the particle melting state based on the in-flight temperature, velocity and diameter, and correlated this parameter with the splat morphology after impact. This index was further refined by Zhang *et al.* through energy analysis [Zhang, 2003]. Efforts have also been made to investigate the in-flight particle oxidation and its influences on coating property. The amount and distribution of the oxide formed in the particles in-flight have been observed by different researchers [Espie, 1999; Neiser, 1998; Sobolev, 1999]. To interpret this oxidation behavior, Wan *et al.* [2001] and Ahmed *et al.* [2001] studied the oxidation mechanisms based on the mass transport and chemical reaction during particle in-flight.

This chapter presents analysis and characterization of the melting and oxidation behavior of in-flight particles. Two practical parameters, melting and oxidation indices, are proposed to estimate the melt fraction and the oxide content, respectively. Values of these two indices will be validated by the three-dimensional simulation results for two common materials, ZrO<sub>2</sub> and Mo. In particular, the melting index of ZrO<sub>2</sub> particles and its relationship with the deposition efficiency and splat morphology will be discussed in terms of experimental data from literatures.

## 6.2 Melting index

Coating is an assemble of splats formed on the substrate and the splat morphologies are directly related to the coating properties. Figure 6.1 is a SEM picture showing splats formed by partially and fully melted ceramic particle. The experimental data revealed that the particle melting status before impact affects the splat morphology. For a partially melted particle, splat is formed in such a way - only melted part of particle is stuck to the substrate. To qualitatively identify the melting status of the particle, the scaling analysis is conducted to the heat and mass transfer for particles in a plasma heated environment as shown in Fig. 6.2. The analysis is based on the assumptions such that the particle is spherical, and heat transfer inside particles is by conduction and heat transfer by convection within the molten part of the particle is negligible; the particle is primarily heated up by the surrounding plasma gas by convection. It shall be noted that once the particle is entrained into the plasma hot core, the particle surface is heated up rapidly and reaches the melting point in a short time (approximately 0.1 ms) [Wan, 1999]. And this heating time is negligible compared with the melting time required for the latent heat dissipating from the surface to the center. From the thermal network analysis, the relationship between the surface temperature,  $T_s$ , the melting temperature,  $T_m$ , and the flame temperature,  $T_f$ , can be obtained as follow,

$$\frac{T_f - T_m}{T_s - T_m} = \frac{R_1 + R_2}{R_1} \quad (6.1)$$

where  $R_1$  and  $R_2$  are the thermal resistances by conduction and convection. Based on spherical particle geometry,  $R_1 = \frac{1}{4\pi k_l} \left( \frac{1}{r} - \frac{1}{r_p} \right)$  and  $R_2 = \frac{1}{4\pi r_p^2 h}$ . If  $T_f - T_m = 1000\text{K}$  is assumed,  $T_s - T_m = 60\text{ K}$  and  $3.2\text{ K}$

are derived for in-flight  $\text{ZrO}_2$  and Mo particles, respectively, using heat transfer coefficient,  $h = 1500\text{ W/m}^2\text{K}$ , particle diameter of  $50\text{ }\mu\text{m}$ , and unmelted core diameter of  $10\text{ }\mu\text{m}$ . Different values for  $(T_s - T_m)$  are attributed to a high thermal conductivity of Mo,  $46\text{ W/mK}$ , compared to a low thermal conductivity of  $\text{ZrO}_2$ ,  $2.32\text{ W/mK}$ . A large temperature difference between the surface and the melt front is an important characteristic for melting a ceramic particle.

**Table 6.1: Operating conditions for plasma spraying of ZrO<sub>2</sub> and Mo.**

Processing parameters	ZrO <sub>2</sub>	Mo
Current, Amp	600	500
Voltage, Volt	69	65
Primary gas flow, Ar, slm <sup>1</sup>	32	40
Secondary gas flow, H <sub>2</sub> , slm	8	8
Carrier gas flow, slm	3	3

<sup>1</sup> slm means standard liter per minute; 1 slm =  $16.67 \times 10^{-6} \text{ m}^3/\text{s}$ .

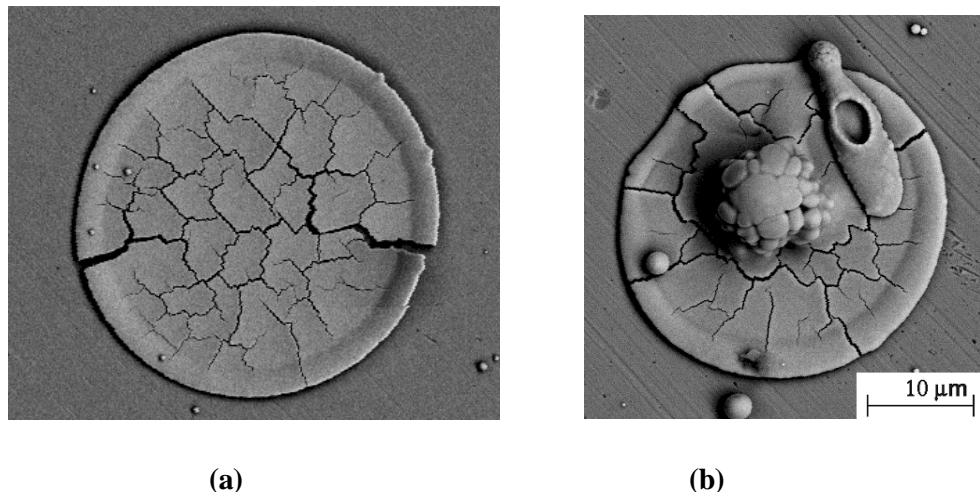


**Figure 6.1: SEM picture of the splat formed (a) by a totally melted ZrO<sub>2</sub> particle and (b) by a partially melted ZrO<sub>2</sub> particle.**

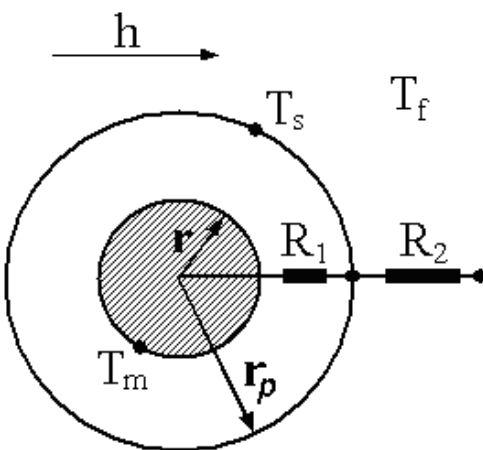


**Figure 6.2: Schematic of the in-flight particle melting process**

For a metal particle, the temperature is virtually uniform inside the particle due to its high thermal conductivity. Thus the particle surface temperature can be used to identify the phase status of the particle. Also due to the high thermal diffusivity of a metal particle, it is easy for a particle to be heated up in the plasma jet to the melting temperature and being melted. For a ceramic particle, the particle temperature changes from a high value at its surface to a low value at its center; and high temperature at the particle surface does not guarantee the particle being fully melted. Thus, in a case of ceramic material that is often of low thermal conductivity and high melting point, the particle being injected into a plasma flame may not be melted completely even if the surface temperature of the particle is much higher than the melting temperature. The melting percentage of the particle depends on its size, thermal conductivity, latent heat, and residence time in the plasma flame. A melting index is therefore needed to determine the melting behavior of a particle.

Defining a dimensionless parameter - melting index M.I. as a ratio of the time for particle in-flight,  $\Delta t_{fly}$ , to the time required for a particle fully melted,  $\Delta t_{melt}$ . Based on the thermal resistance analysis, the total time required for a particle being fully melted, is estimated analytically. For most plasma spray conditions, the Biot number for powder particles is small. The temperature distribution in the solid phase

is negligible. Thus, the total heat transferred to the particle melt and solid interface shall be balanced with the latent heat absorbed by particle for melting. This is described mathematically as follows,

$$\frac{T_f - T_m}{R_1 + R_2} = \frac{1}{4\pi k_l} \left( \frac{1}{r} - \frac{1}{r_p} \right) + \frac{1}{4\pi r_p^2 h}, \quad (6.2)$$

where  $L$  is the latent heat of fusion, and  $\rho \cdot 4\pi r^2 \frac{dt}{dt} \cdot L = \frac{T_f - T_m}{4\pi k_l} \left( \frac{1}{r} - \frac{1}{r_p} \right) + \frac{1}{4\pi r_p^2 h}$ . Substituting  $\dot{m}$  into Eq. (6.2),

$$\dot{m} = -4\rho\pi r^2 \frac{dr}{dt} \quad (6.3)$$

is obtained. It shall be noted that the convection heat transfer coefficient  $h$  varies with the particle location. Nevertheless its variation along the particle trajectory in the regular plasma spray conditions is not significant for the given gun power condition. Eq. (6.3) can then be integrated and the total melting time is derived as follows,

$$\Delta t_{melt} = \frac{r_p^2}{6} \left( 1 + \frac{2}{Bi} \right) \cdot \frac{\rho L}{k_l (T_f - T_m)} \quad (6.4)$$

in which  $Bi = hr_p/k_l$ . The melting time for  $ZrO_2$  particles with radius of 25 and 50  $\mu m$  are estimated as 2.1 ms and 30 ms, respectively; while the melting time for Mo particles with these two radii are about 0.028 ms and 0.11 ms, respectively. In this estimation,  $h = 1500 \text{ W/m}^2\text{K}$  and  $T_f - T_m = 3000\text{K}$  are used along with the particle properties listed in Table 5.2. Apparently, a metal particle melts much faster than a ceramic particle of equivalent size. With Eq. (6.4), the melting index can be formulated as follows,

$$M.I. = \frac{\Delta t_{fly}}{\Delta t_{melt}} = \frac{6k_l}{\rho L} \cdot \frac{1}{1 + 2/Bi} \cdot \frac{(T_f - T_m) \cdot \Delta t_{fly}}{r_p^2}. \quad (6.5)$$

### 6.3 Oxidation index

The plasma spraying of metals in atmospheric environment inevitably leads to oxide formation. Different oxidation mechanisms should be considered for different material and in different stage of particle temperature. For example, Wan et al. [2001] considered three oxidation mechanisms for molybdenum

(Mo) particle: diffusion in an oxide thin film at a surface temperature lower than 450 °C, chemical reactions at temperature higher than 500 °C, and adsorption of oxidant diffused from the gas to the surface when the particle is melted. Their Results show that the primary oxidation mechanism for in-flight Mo particle is the adsorption after particle melting since the reaction rates of the two former mechanisms are very small, usually below  $10^3 \text{ kg(O)/m}^2\text{-s}$ , and the oxidation time is short due to rapid heating of Mo particles toward melting point. Therefore we only considered the primary oxidation mechanism that the oxidant diffuses from the gas to the melted surface and reacts with the metal particle. This mechanism can be represented by:

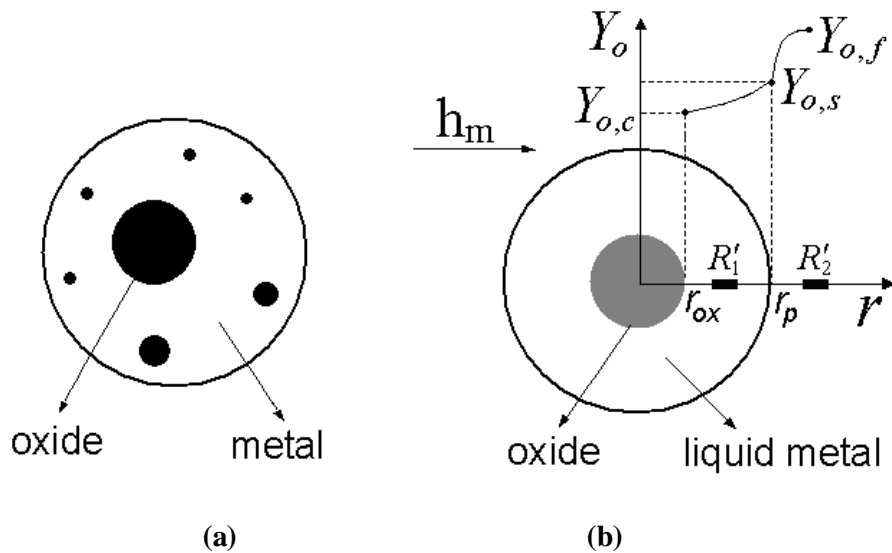


**Figure 6.3: Schematic of the in-flight particle oxidation process: (a) cross section of an oxidized particle, (b) mass transfer and diffusion of oxidant through the particle.**

The oxide phase will be formed and separated from the metal phase due to the difference of the surface tension. SEM experiments conducted by Espie [2001] in the atmospheric plasma spray showed that the collected in-flight iron particles have distinguishable oxide granules,  $Fe_{0.95}O$ . Typically, a large oxide grain is formed within the particle, and some small oxide grains are distributed around it, as

indicated in Fig. 6.3 (a). To reduce the complexity of the problem, we assume that all the oxides form a large grain and is located at the particle center, as shown in Fig. 6.3 (b). From the resistance network analysis, the relationship of the oxygen concentration on the particle surface,  $Y_{o,s}$ , in the particle center,  $Y_{o,c}$ , and in the gas phase,  $Y_{o,f}$ , can be obtained as follows,

$$\frac{Y_{o,f} - Y_{o,c}}{Y_{o,f} - Y_{o,s}} = \frac{R'_1 + R'_2}{R'_2} = 1 + Bi_m \left( \frac{r_p}{r} - 1 \right), \quad (6.7)$$

where  $R'_1$  and  $R'_2$  are the mass transfer resistances by diffusion and convection, respectively.  $Bi_m$  is the mass transfer Biot number,  $Bi_m = r_p h_m / \rho_l D_{o,l}$ . Based on spherical geometry,

$R'_2 = \frac{1}{4\pi r_p^2 h_m}$ . If  $Y_{o,f} - Y_{o,c} \approx Y_{o,f} = 0.4$  is assumed,  $Y_{o,s} = 0.04$  and  $0.2$  are derived for  $Bi_m = 0.025$  and

0.25 respectively, using particle diameter of  $50 \mu\text{m}$  and oxide grain diameter of  $10 \mu\text{m}$ . The concentration of oxygen at the particle surface strongly depends on the mass transfer Biot number, and this in-flight oxidation process is either diffusion-in-melt control for the case of large  $Bi_m$ , or mass-transfer-in-gas control for the case of small  $Bi_m$ . Note that for large mass transfer Biot number, e.g. larger than 1, the concentration of oxygen in the melted surface might reach the solubility of oxygen in the liquid Mo.

The oxidant flux at the particle surface can then be expressed as follows:

$$m''_o = \frac{Y_{o,f} - Y_{o,c}}{R'_1 + R'_2} = m''_{ox} \frac{W_o}{W_{ox}}, \quad (6.8)$$

where  $W_o$  and  $W_{ox}$  are the atomic weights of the oxidant and the oxide product, and  $m''_{ox} = \rho_{ox} 4\pi r^2 \frac{dr}{dt}$ .

Substituting  $m''_{ox}$  into Eq. (6.8)  $4\pi r^2 \frac{dr}{dt} = \frac{Y_{o,f} - Y_{o,c}}{\frac{1}{4\pi \rho_l D_o} \left( \frac{1}{r} - \frac{1}{r_p} \right) + \frac{1}{4\pi r_p^2 h_m}} \cdot \frac{W_{ox}}{W_o}$ .

is obtained. Assuming constant mass transfer coefficient  $h_m$  and gas oxygen concentration  $Y_{o,f}$ , Eq. (6.9) can be integrated and the oxide grain size,  $r_{ox}$ , can be obtained as such,

$$\frac{r_{ox}^2}{2} + \frac{r_{ox}^2}{3r_p} \left( \frac{1}{Bi_m} - 1 \right) = (Y_{o,f} - Y_{o,c}) D_{o,l} \frac{W_{ox}}{W_o} \frac{\rho_l}{\rho_{ox}} t . \quad (6.10)$$

Oxidation index,  $O.I.$ , is then defined as the mass fraction of the oxide in the particle as follows,

$$O.I. = \frac{m_{oxide}}{m_{particle}} = \frac{W_{ox}}{W_o} \cdot \frac{t}{r_p^2 \left[ \frac{r_p}{2r_{ox}} + \frac{1}{3} \left( \frac{1}{Bi_m} - 1 \right) \right]} . \quad (6.11)$$

For the case in which mass transfer Biot number is much larger than one, the resistance of the diffusion resistance in the liquid droplet will be dominant, and  $Y_{o,f} \approx Y_{o,s} \gg Y_{o,c}$ . Eq. (6.11) can then be simplified

to:

$$O.I. = (Y_{o,f} - Y_{o,c}) D_o \frac{W_{ox}}{W_o} \frac{t}{r_p^2 (B/2 - 1/3)} , \quad (6.12)$$

where  $B$  is the ratio of the particle radius to the oxide grain radius,  $r_p/r_{ox}$ .

For the case in which mass transfer Biot number is much smaller than one, the resistance of the mass transfer in the gas phase will be dominant, and  $Y_{o,f} \gg Y_{o,s} \approx Y_{o,c}$ . Eq. (6.11) can then be simplified

to:

$$O.I. = 3h_m (Y_{o,f} - Y_{o,c}) \frac{W_{ox}}{W_o} \frac{t}{\rho_l r_p} = 3 \frac{W_{ox}}{W_o} \cdot Bi_m \cdot (Y_{o,f} - Y_{o,c}) \cdot Fo_m . \quad (6.13)$$

Therefore, more oxide will be formed if the convective mass transfer resistance is smaller (larger  $Bi_m$ ), flight time longer (larger  $Fo_m$ ), and/or the oxygen concentration larger in the environment (larger  $Y_{o,f}$ ).

#### 6.4 Determination of the heat and mass transfer coefficients

In the formulations of melting index and oxidation index, the heat and mass transfer coefficients between the particle surface and the environment,  $h$  and  $h_m$ , are unknown. These parameters depend on plasma jet conditions, particle size and trajectory. Thus numerical simulations have been performed to determine

their average values using a well-tested and validated code – LAVA for plasma spray. The details of this numerical model have been presented in Chapter 2 and Chapter 4. A DC plasma spraying process, as displayed in Fig. 1.1, has been simulated using the experimental operating conditions listed in Table 6.1, with the powder materials of ZrO<sub>2</sub> and Mo, respectively. Particle sizes ranging from 20 to 60 µm have been investigated.

## 6.5 Experimental process

In present study, experiments using a PTF 4 MB DC plasma gun have been carried out to investigate the melting index of ZrO<sub>2</sub> particles and their relationship with deposition efficiency and splat morphology. The experimental operating conditions are listed in Table 6.1, same as in the simulation. Partially stabilized zirconia (PSZ) AE7592 from Sulzer-Metco, which is a plasma densified hollow spherical powder (HOSP), with a mean size of 36 µm was used as the feedstock. The particle injector is located at 0.6 cm away from the torch exit. Information for in-flight particles and splats are collected at the spray distance of 6, 8, 10 and 12 cm, respectively. The Tecnar DPV 2000 diagnostic system was used to measure the in-flight particle size, velocity and surface temperature. Splats were collected on mirror polished 304 stainless steel (roughness < 0.1µm). A large number (70) of splats were scanned by means of scanning white light interferometry (SWLI), and Zygo New Viewer 200.

## 6.6 Results and discussion

### 6.6.1 Melting index

To evaluate the particle heat transfer coefficient, numerical results have been obtained and compared with the experimental data. Figure 6.4 shows the numerical results of axial velocity, surface temperature and melting status for ZrO<sub>2</sub> particles. It reveals that a small particle has a high axial velocity and a high surface temperature. All particles start melting virtually at the same location, regardless of the size. They are totally melted after a flight distance of 1.1, 1.8, 3 and 5.5 cm for particles with diameters of 20, 30, 40,

and 50  $\mu\text{m}$ , respectively. The latent heat of fusion and thermal resistance accounts for the different flight time to be fully melted for particles with different sizes. A 60  $\mu\text{m}$  diameter particle has never been fully melted.

Averaged particle velocity and temperature from the DPV2000 measurement are also shown in Fig. 6.4. The simulation results agree reasonably well with the experiment in consideration of the uncertainty in the measurements. Note that the measured velocity decreases significantly between the spray distance of 6 cm and 12 cm, while the simulation shows that the particle velocity are almost constant after certain spray distance. The reason is that the DPV2000 tends to see the large and hot particles better. After spray distance of 6 cm, the DPV2000 is not sensible to the small particles that cool down rapidly.

To interpret the particle melting process analytically, we need to estimate the particle flight time, the flame temperature and the heat transfer coefficient using the simulation results. The flight time is approximated as  $\Delta t_{\text{fly}} = 2S / V_p$  by assuming the particle motion with constant acceleration, where  $S$  is the axial flight distance and  $V_p$  is the particle axial velocity. The simulation results in Fig. 6.4 (a) justified this assumption at the particle melting stage.

Figure 6.5 shows heat transfer coefficient  $h$  and the flame temperature  $T_f$  during the melting process of  $\text{ZrO}_2$  particles. The heat transfer coefficient is related to the particle size, Reynolds number and the flame thermal conductivity. The results show that  $h$  varies within a small range during melting for a given size and the averaged values are obtained, *i.e.*,  $h = 3.5, 3.2, 2.6, 2.2$ , and  $2.1 \times 10^4 \text{ W}\cdot\text{m}^{-2}\text{K}^{-1}$  for particles with diameters of 20, 30, 40, 50 and 60  $\mu\text{m}$ , respectively. These values will be used to calculate the melting index.

The particles with different sizes will experience different flame temperature, since each particle undergoes its own trajectory. Small particles experience low flame temperature since they cannot penetrate the flame center easily, as shown schematically in Fig. 1.1. On the contrary, a large particle reaches the center of the plasma flame but moves away from the hot core of the plasma jet.. Since the flame temperature is related to the particle surface temperature (see Eq. (6.1)), we introduce a

dimensionless temperature  $A = (T_f - T_m) / (T_s - T_m)$  to estimate the flame temperature. As shown in Fig. 6.5 (c), this dimensionless temperature behaves similarly during the melting process for particles with different sizes. Substituting  $\Delta t_{fly}$  and  $A$  to Eq. (6.5),

$$M.I. = A \frac{12k_l}{\rho L} \cdot \frac{1}{1 + 2/Bi} \cdot \frac{(T_s - T_m)S}{r_p^2 V_p} \quad (6.14)$$

is obtained. Note that in experiments, particle surface temperature and velocity are measurable. The properties such as  $k_l$ ,  $L$ ,  $\rho$ , and  $T_m$  are also known for the selected powder material. However, the values of  $A$  and  $h$  are unknown and have to be estimated either from experiments or simulations.

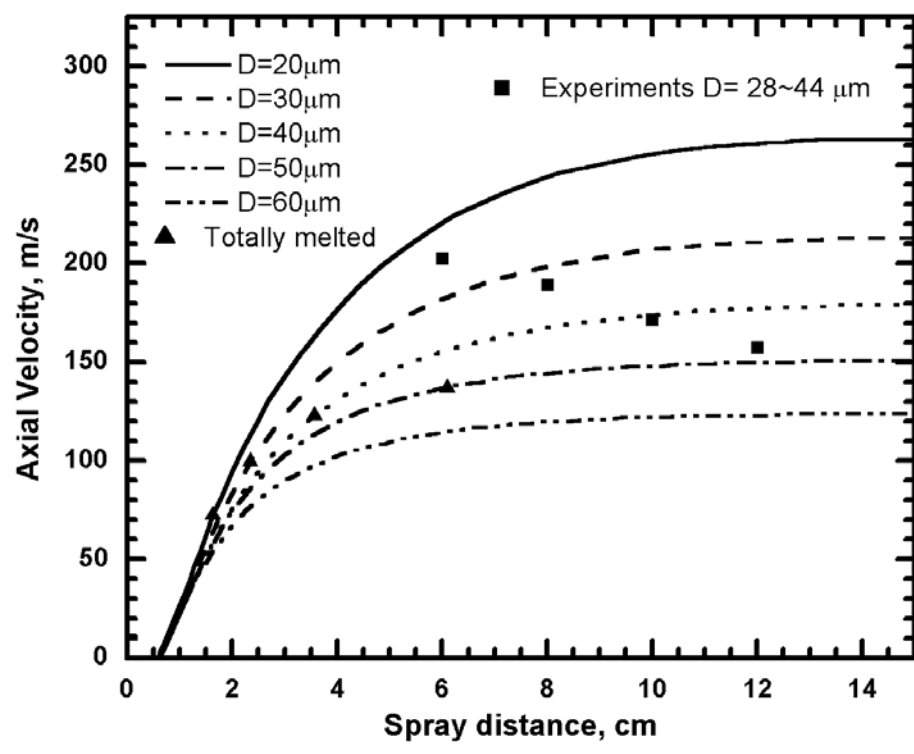
The melting index of  $ZrO_2$  particle calculated by Eq. (6.14) is shown in Fig. 6.5 (d) along with the simulation results of melting fraction,  $f$ . The analytical melting index agrees well with the particle melt fraction. When the particles are fully melted ( $f = 1$ ), the melting index,  $M.I.$ , ranges from 0.8 to 1.2 for the particles of  $D = 20\text{-}40 \mu m$ . The results of melting index deviate more from the melting fraction for large particles of  $D = 50\text{-}60 \mu m$ , since their surrounding flame temperature changes dramatically during the in-flight (see Fig. 6.5 (c)). Therefore, the steady-state assumption for heat transfer analysis becomes questionable. This can be improved in the future by considering the transient heating and cooling process.

If the  $ZrO_2$  particle diameter is smaller than 1  $\mu m$ , the Biot number will be much smaller than one, even with an extreme high heat transfer coefficient of  $10^4 \text{ W m}^{-2} \text{ K}^{-1}$  under the plasma conditions. For this case, the melting index can be further simplified as such,

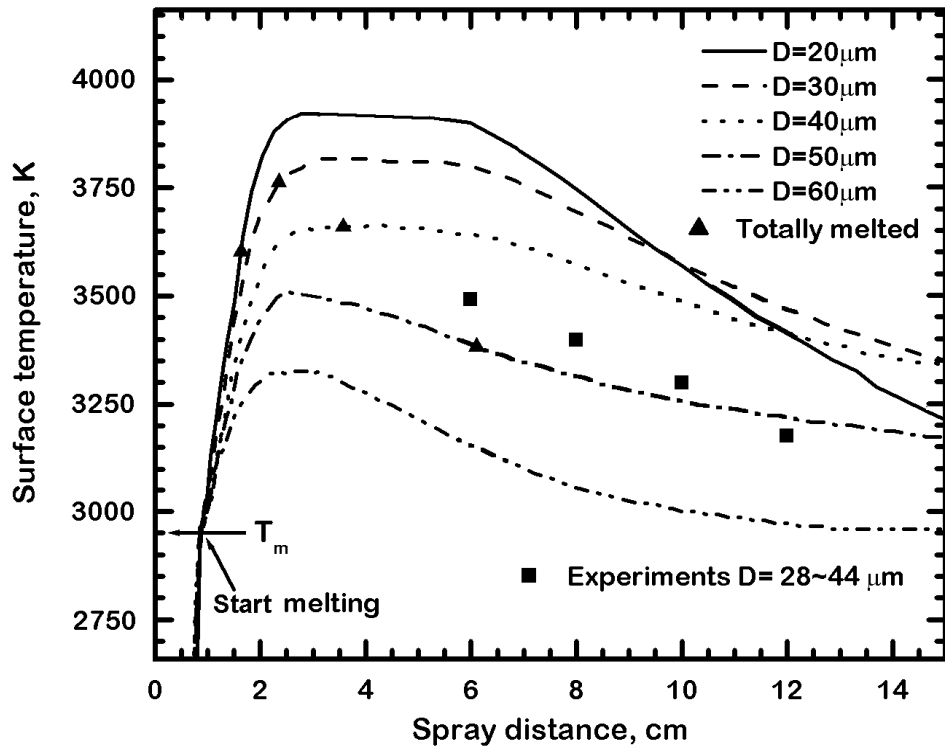
$$M.I. \approx A \frac{3h}{\rho L} \cdot \frac{(T_s - T_m) \cdot \Delta t_{fly}}{r_p} = 3A \cdot Bi \cdot Ste \cdot Fo \quad . \quad (6.15)$$

Eq. (6.15) revealed that the melting status of particle is proportional to the product of Biot, Stefan and Fourier numbers if the convection is dominant. Better melting will be expected in the case that more heat is convectively transferred from the surface to the particle. In general, the particles are more difficult to be melted in the high-velocity-oxy-fuel spray process due to its short residence time in the flame that prevents particle from receiving large amount of heat. The formulations derived in Eq. (6.14) and (6.15)

will be helpful for determining the melting behavior of the particles. Eventually, it can be used for control and optimization of spraying process.

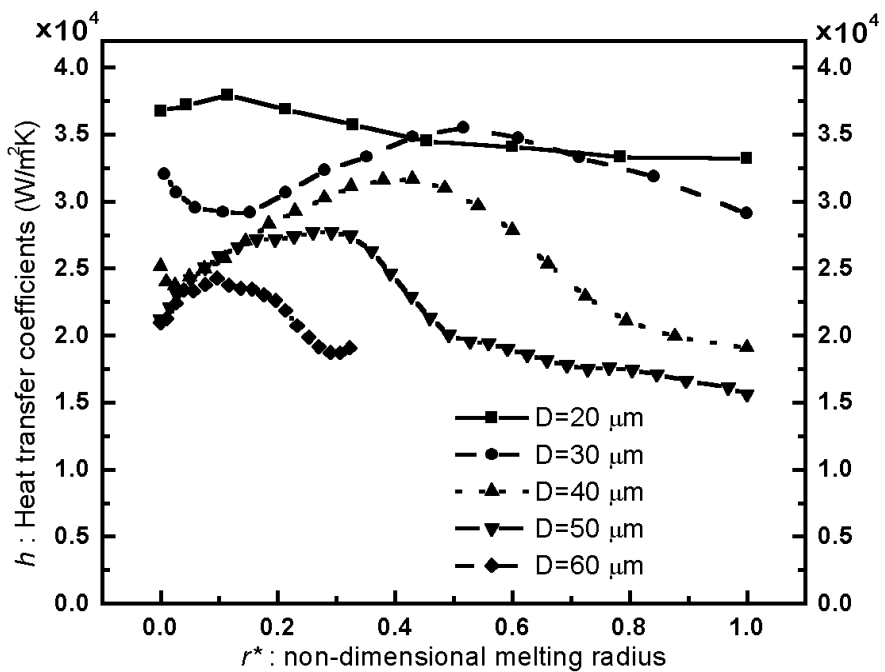


(a)

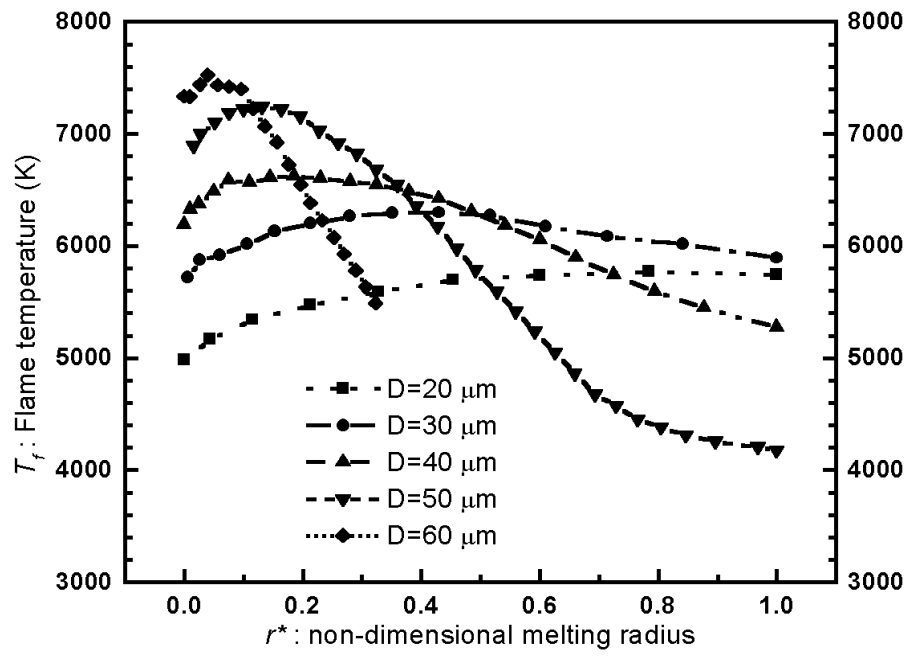


(b)

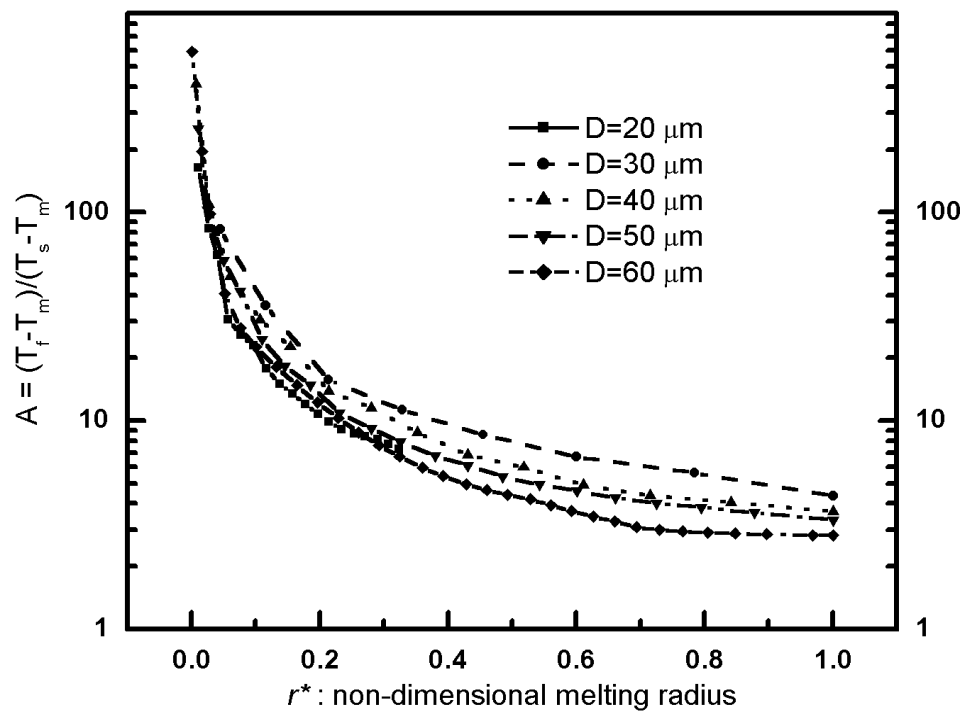
**Figure 6.4:** (a) Particle velocity, and (b) surface temperature for different sizes of  $\text{ZrO}_2$  particles, with experimental data (in courtesy of L. Li, A. Vaidya and S. Sampath).



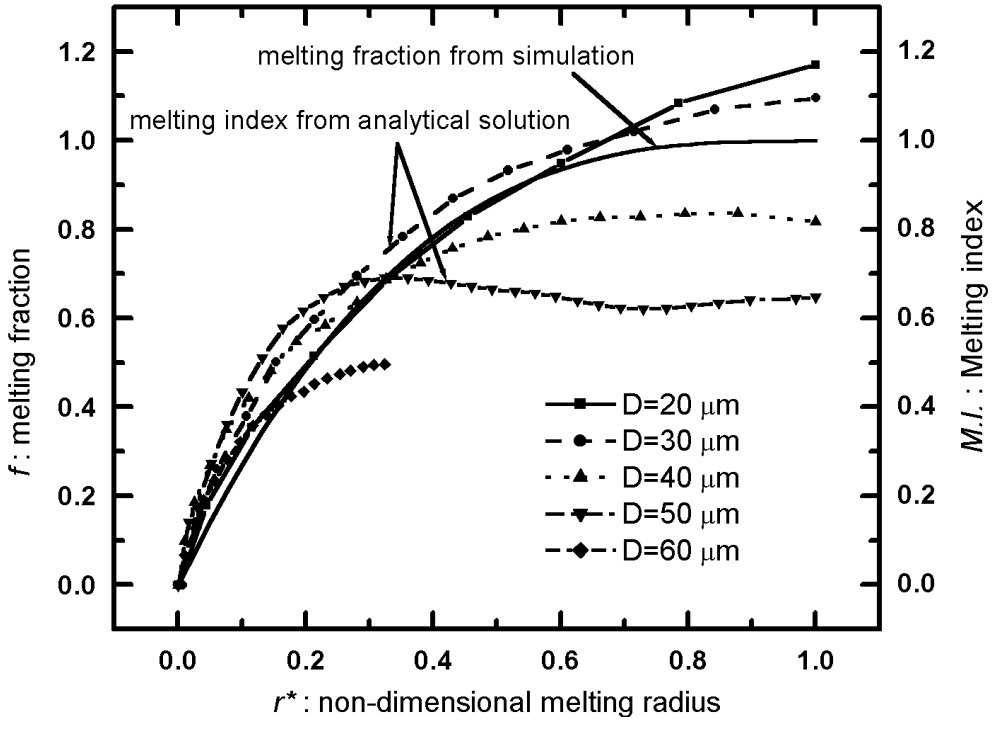
(a)



(b)



(c)



(d)

**Figure 6.5:** (a) Heat transfer coefficient, (b) flame temperature, (c) dimensionless temperature  $A=(T_f-T_m)/(T_s-T_m)$  and (d) melting index vs. the non-dimensional melting radius,  $r^*=(r_p-r_m)/r_p$ , for  $\text{ZrO}_2$  particles.

## 6.6.2 Melting index for experiments

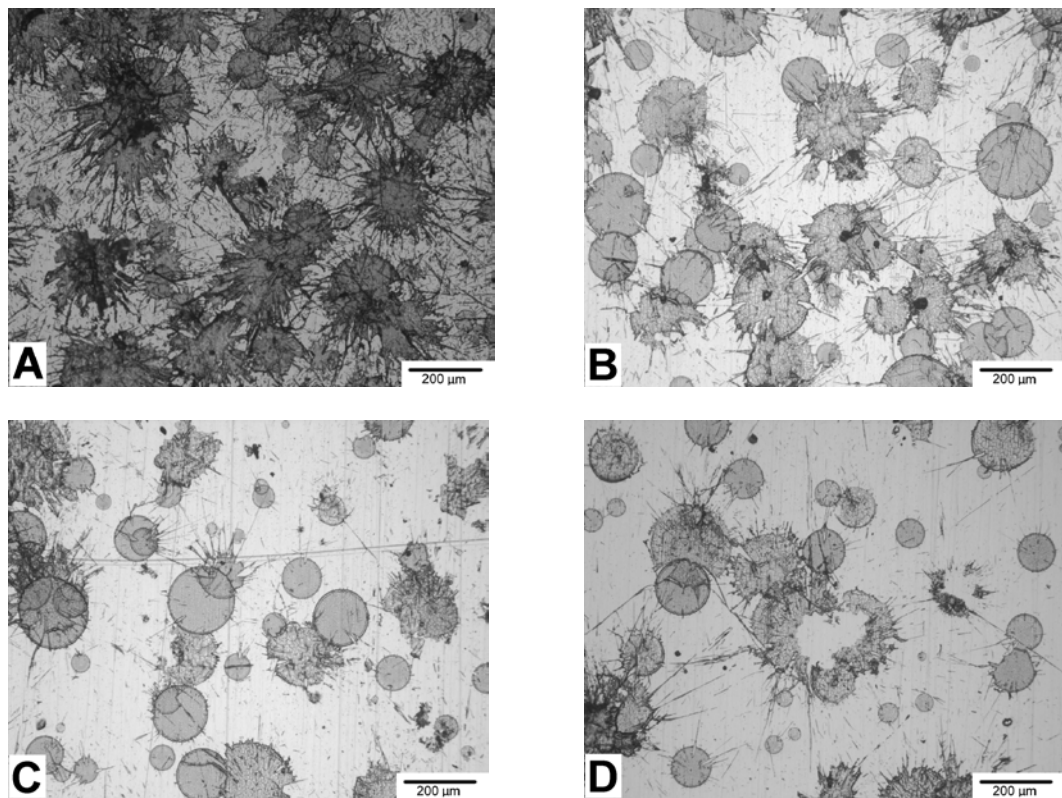
After validating with simulation, melting index can be used to characterize the melting status of the in-flight particles in plasma spraying. Previous experimental studies have shown that the melt fraction of the in-flight particle has a great influence on the deposition efficiency and the splat morphology [Vaidya, 2001]. Since a better particle melting status will increase the deposition efficiency, the prediction of the melting is important for experiments. Melting index is used in our study for this purpose. For experiment of plasma sprayed  $\text{ZrO}_2$  particles with diameter  $36 \mu\text{m}$ , melting index is calculated by Eq. (6.14) with numerically estimated heat transfer coefficient ( $h = 3 \times 10^4 \text{ W m}^{-2} \text{ K}^{-1}$ ) and dimensionless flame temperature ( $A = 3.3$ ).

Figure 6.6 shows the SEM pictures of the collected splats, melting index and the deposition rate at different spray distances. At the fixed powder feeding rate of 0.15 g/min, the deposition rate ( $\leq 0.15$  g/min) is a convenient parameter to represent the deposition efficiency. The results show a good correlation between the melting index and the splat deposition rate. This indicates that melting index can be used to characterize the melting fraction of the ceramic particles upon impact, and therefore can be used as a control parameter to improve the spray yield. Note that the highest particle temperature is at spray distance of 6 cm (see Fig. 6.4 (b)), which corresponds to a low deposition rate of 0.06. The reason is that the flight time is not long enough and the particle melting index is small.

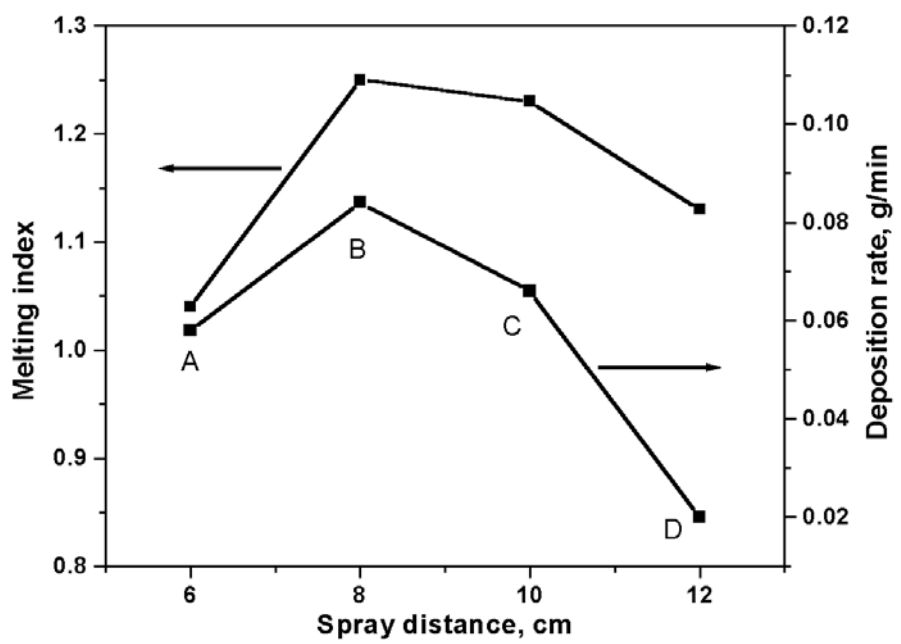
The effects of the melting index on the splat morphology are also observed. The splat morphology is characterized by fragmentation degree  $DS$ , which presents the extent of the break up of a splat, and is defined as:

$$DS = P^2/(4\pi A), \quad (6.16)$$

where the peripheral length  $P$  and the splat area  $A$  is measured from the Zyglo Viewer.  $DS$  equals to unit for a rigid disk-like shape splat. The splat fragmentation degree at different particle melting index and particle Reynolds number are shown in Fig 6.7. The splat fragmentation degree is found to be dependent primarily on the particle Reynolds number,  $2\rho_p V_p r_p / \mu_{p,l}$ , which refers to the particle kinetic energy before impact. For the same particle Reynolds number, particle with a larger melting index will have less possibility to form fragmentation.



(a)



(b)

Figure 6.6: (a) SEM pictures of collected splats and (b) effects of melting index on deposition rate at different spray distances of 6, 8, 10 and 12 cm (in courtesy of L. Li, A. Vaidya and S. Sampath).

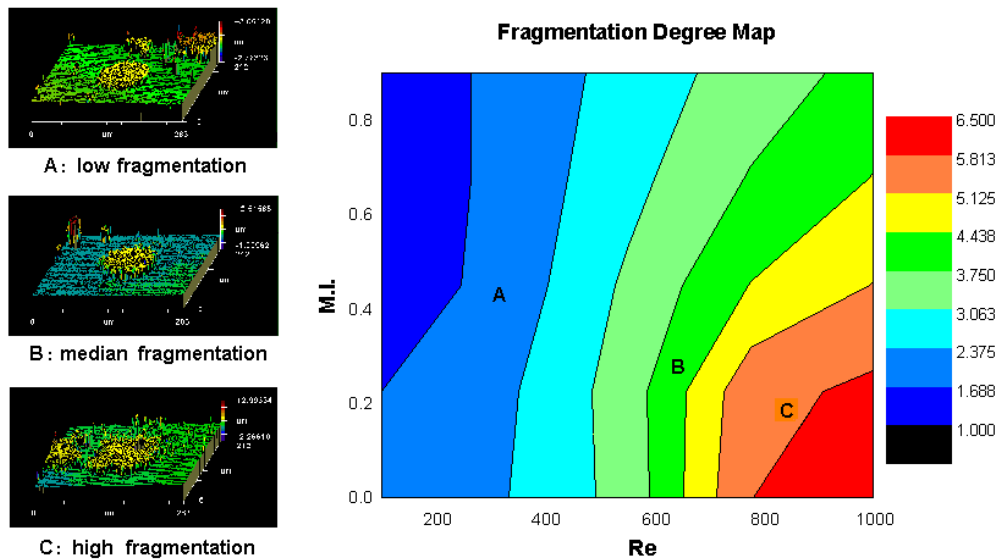


Figure 6.7: Effects of melting index and particle Reynolds number on splat fragmentation degree  
(in courtesy of L. Li, A. Vaidya and S. Sampath).

### 6.6.3 Oxidation index

The oxidation index, a dimensionless parameter for the metal particle oxidation behavior, is discussed in this part using Mo as an example. The mass transfer coefficient and the oxygen concentration surrounding the particles, which are critical in the oxidation index calculation, are estimated from numerical simulation results as shown in Figs. 6.8 (a) – (b). The mass transfer coefficient increases as the particle size decreases. The oxygen concentration is related to the particle trajectory and the ambient air

entrainment. The oxygen concentration is small before the particle reaches the centerline, since both the molecular oxygen ( $O_2$ ) from air entrainment and the atomic oxygen (O) from dissociation are small. The oxide content formed during particles in-flight, where  $MoO_3$  phase is assumed to be formed, is shown in Fig. 6.8 (c). Smaller particles contain more oxide, which results from the large mass transfer coefficient and the large surface to volume ratio.

The analytical results of the oxidation index for Mo particles, which are calculated from the averaged mass transfer coefficient and oxygen concentration  $h_m$  and  $Y_{o,f}$ , are shown in Table 6.2. The oxidation index at the spray distance of 15 cm is calculated using Eq. (6.13), since the mass transfer Biot number is much smaller than one, e.g., 0.025 if using  $r_p = 25 \mu m$ ,  $h_m = 5 \text{ kg/m}^2\text{s}$ , and  $D_{o,l} = 5 \times 10^{-7} \text{ m}^2/\text{s}$ . The results show that the oxidation index agrees well with the oxide mass fraction predicted from the numerical simulations, indicating that the analytical oxidation index interprets the oxide content correctly.

If the oxidation time  $t$  can be estimated as the flight time  $\Delta t_{fly}=2S/V_p$ , Eq. (6.13) can be rewritten as such,

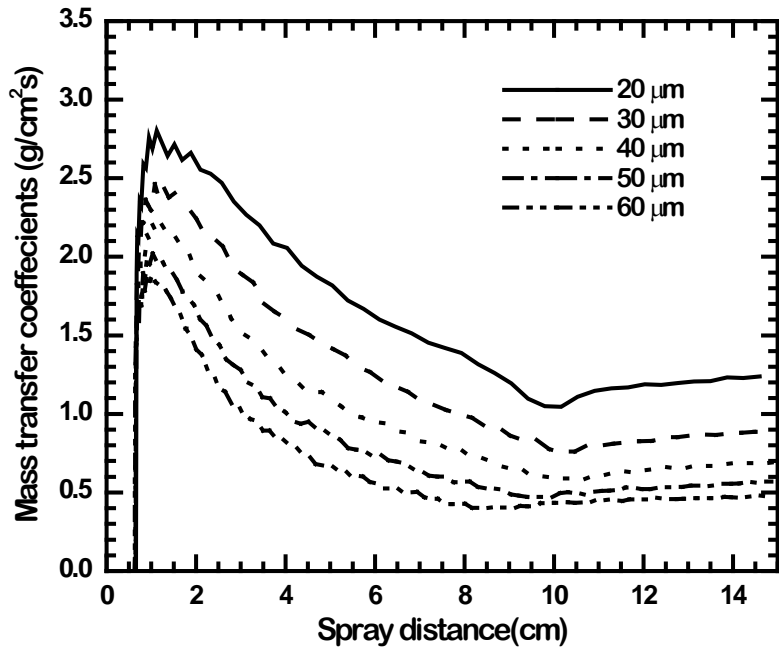
$$O.I. \approx \frac{6(Y_{o,f} - Y_{o,c})}{\rho_l} \frac{W_{ox}}{W_o} \frac{Sh}{d_p} \frac{\rho_f D_{o,f}}{V_p d_p} \propto \frac{S}{V_p d_p^2} \quad (6.17)$$

where  $Sh$  is defined in Eq. (3.31),  $D_{o,f}$  is the diffusion coefficient of the oxygen in the plasma flame, and  $\rho_f$  is the Favre-averaged gas density around the particle [Williams]. It reveals that the oxide content increases monotonically with the spray distance, and decreases with the particle size and velocity. This analytical conclusion is validated by the numerical simulation results (see Fig. 6.9). The oxide content at the spray distance of 10 cm is proportional to  $(V_p d_p)^{-1}$ , which agrees well with the prediction of Eq. (6.17). Currently we have no experimental data regarding to the metal particle oxidation in the plasma spray. However, such experiments have been conducted by other groups, and similar results have been achieved. For example, in Ref. [Espie, 2001], experiments with iron particles in atmospheric plasma spraying showed that the oxide content increased with the spray distance monotonically. This result agrees well with our simulation result depicted in Fig. 6.8 (c), as well as the analysis of the oxidation index. The

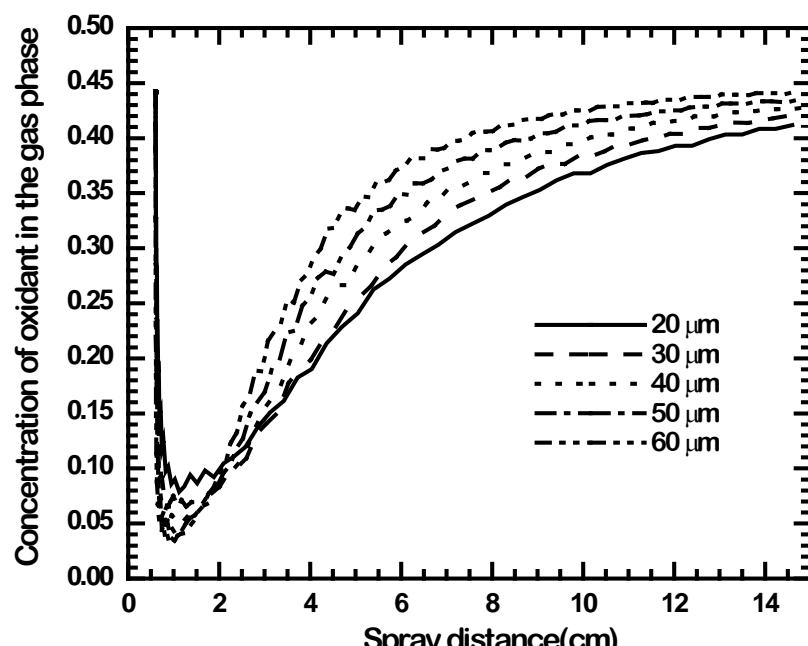
oxidation index, Eq. (6.17), also shows that in-flight particles oxidation can be reduced if proper measure is taken, such as to shorten the spray distance, to reduce the number of small particles in the feedstock, or to minimize the oxygen entrainment by low pressure plasma spray or inert plasma spray.

**Table 6.2: Simulation results of the oxidation index of Mo at spray distance of 15 cm.**

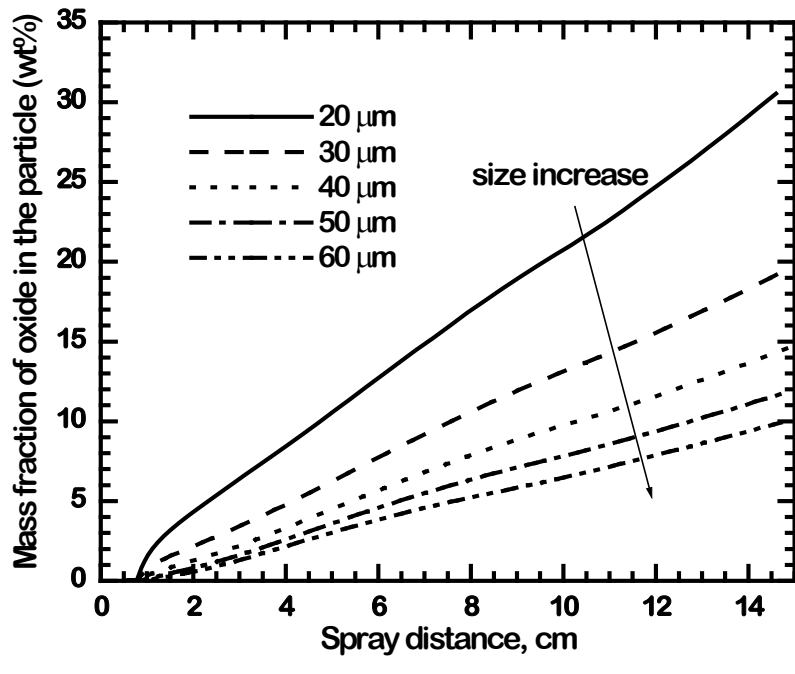
$r_p, \mu\text{m}$	10	15	20	25	30
Ave. $Y_{o,f} - Y_{o,c}$	0.24	0.25	0.27	0.29	0.30
Ave. $h_m, \text{kg}\cdot\text{m}^2\text{s}^{-1}$	18.0	14.3	11.6	9.6	8.1
Flight time, ms	0.9	1.0	1.3	1.5	1.8
Oxide fraction by simulation	0.32	0.20	0.15	0.12	0.11
Oxidation Index by Eq. (6.13)	0.36	0.22	0.18	0.15	0.13



(a)



(b)



(c)

**Figure 6.8: (a) Mass transfer coefficient, (b) mass fraction of oxygen in the gas phase, and (c) oxide content vs. the spray distance for Mo particles with diameters of 20, 30, 40, 50 and 60 μm.**

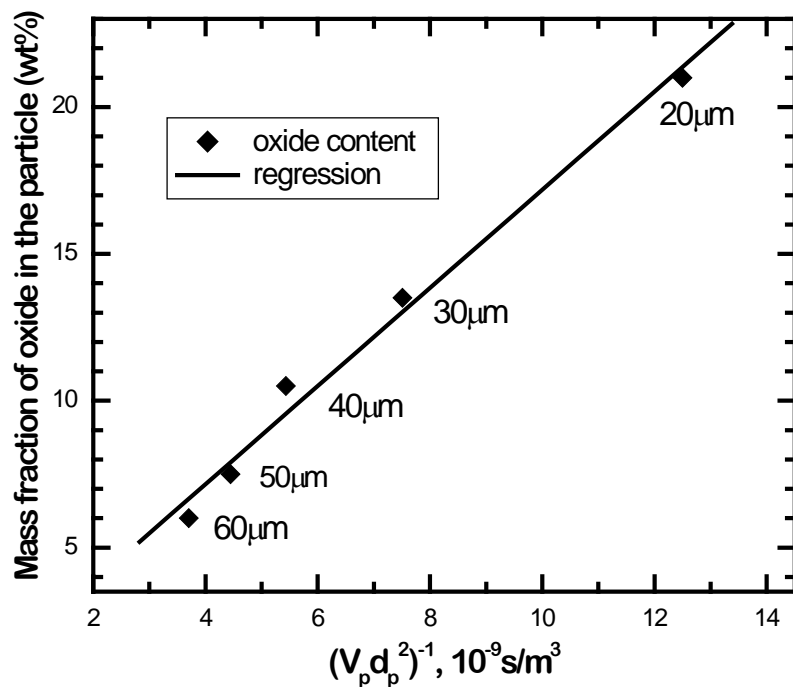


**Figure 6.9: Oxide content at the spray distance of 10 cm vs.  $(V_p d_p^2)^{-1}$ , for Mo particles with diameters of 20, 30, 40, 50 and 60  $\mu\text{m}$ .**

## **Chapter 7      Parametric Studies of RF Induction Plasma Spray**

The integrated model developed in Chapter 2 and Chapter 3 for the RF plasma flame and the particle-plasma interaction is applied to simulate the RF plasma spray process. The electromagnetic field, plasma velocity and temperature, and the particle behaviors are predicted numerically. Effects of the operating conditions on the particle behaviors are also investigated.

### **7.1 Introduction**

The process of RF plasma spraying is highly integrated, including several complicated steps such as coupling of the electromagnetic field and the plasma generation, atomization of the solution mixture, rapid heating, drying and evaporation of the droplets, chemical reactions during in-flight and on the substrate, et al. There are a number of operational problems that must be solved before successful application of this technique. One of the problems is that, some injected particles have a tendency to be repelled from the hot plasma core and to have a low heating rate [Chase, 1971]. Such effects are caused by the complex flow inside the torch and by the strong coupling between the electromagnetic field and the temperature field through an electrical conducted media, the plasma. The splat formation and the coating microstructure will strongly depend on the particle behaviors, such as velocity, temperature and melting. As shown in Fig. 7.1, experiments found that both faceted equiaxed grain and lamellar structure are present in the RF plasma sprayed zirconia coatings, as well as the irregular voids produced by the unmelted particles [Margolis, 1998]. This indicated that the operating conditions require optimization, in order to obtain the specified coating structure. Therefore, to increase the productivity and explore the new capability of RF plasma spraying, it is essential to understand the plasma generation, thermo-fluid field and the injected particles behavior in RF plasma spray process.

Numerical simulations have been used to investigate the complex RF induction plasma spray process. Boulos and his colleges have conducted numerous researches for the electromagnetic field, heat

mass and momentum transport phenomena in RF plasma [Boulos, 1997]. Non-equilibrium chemical reaction has also been studied by Tanaka [2002]. Recently, Xue has proposed a more comprehensive model with considering the axial electric field induced by the axial component in the coil current [2003] and Shigeta has studied the RF induction plasma with seeded metal vapor, potassium [2004]. However, less attention has been paid to the particle behavior in the induction plasma spraying.

In this chapter, an integrated model is developed for the induction plasma torch and the particle physics, *i.e.*, particle heating, melting, and evaporation during in-flight. The studied phenomena include the electromagnetic field, the thermo-fluid flow, the plasma physics and chemistry, and the interaction between the plasma gas and the injected particles.

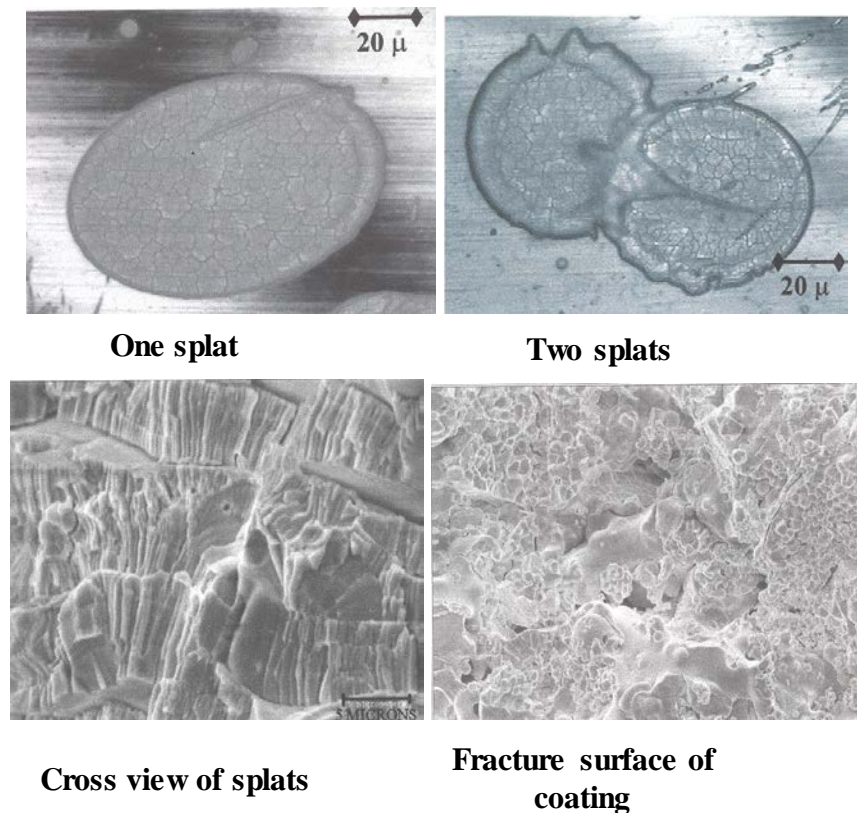


**Figure 7.1: SEM pictures of RF sprayed  $\text{ZrO}_2$  splats and coatings.**

## 7.2 Basic description of the problem

The schematic of the RF induction plasma torch for the spraying system has been shown in Fig. 1.2. The torch is composed of three coaxial nozzles for distributing the carrier gas, central gas and sheath gas

respectively. A long quartz tube wall is used to confine the plasma. The particles along with the carrier gas ( $Q_1$ ) are injected from the center nozzle, called feeder. The central gas ( $Q_2$ ) is the main gas source of the plasma, while the sheath gas ( $Q_3$ ) is provided to prevent the plasma from contacting and damage the inner tube wall (see Fig. 1.2). Cooling water is also used to keep the feeder and the outer tube wall from overheating.

A benchmark case has been studied for the radio frequency induction plasma spray process. The operating conditions listed in Table 7.1.

**Table 7.1: Operating conditions for RF induction plasma spraying.**

Processing parameters	Values
$\Phi_1$ , inner diameter of nozzle 1 (feeder), mm	6
$\Phi_2$ , inner diameter of nozzle 2, mm	38
$\Phi_3$ , inner diameter of nozzle 3, mm	50
$\Phi_c$ , diameter of coil, mm	66
$Z_1$ , torch length, mm	203
$Z_2$ , axial coil position, mm	103
$Z_3$ , coil length, mm	66
$Q_1$ , carrier gas, Ar, slm <sup>1</sup>	2
$Q_2$ , central gas, Ar, slm	3
$Q_3$ , sheath gas, Ar, slm	31
Inlet temperature, K	300
Torch pressure, Torr	300
Coil input power, kW	65
Coil current frequency, kHz	333

<sup>1</sup> slm means standard liter per minute; 1 slm = 16.67 cm<sup>3</sup>/s.

### 7.3 Validation of the electromagnetic model

To validate the electromagnetic model, simulations have been performed for a cylindrical metallic load with constant electrical conductivity. The load, 38 cm in diameter (same as the inner diameter of nozzle 2), was centrally placed inside the coil. Four electric conductivities are used: 0 (as in vacuum), 600, 1000 and  $1500 \Omega^{-1} m^{-1}$ . The distributions of the vector potential for the case with constant electrical conductivity of  $1500 \Omega^{-1} m^{-1}$  are plotted in Fig. 7.2 (a) and (b). Other than the cylindrical region of the metallic load, the electrical conductivity is set as zero. Therefore, the electromagnetic field is almost symmetrical about the fourth-turn coil.

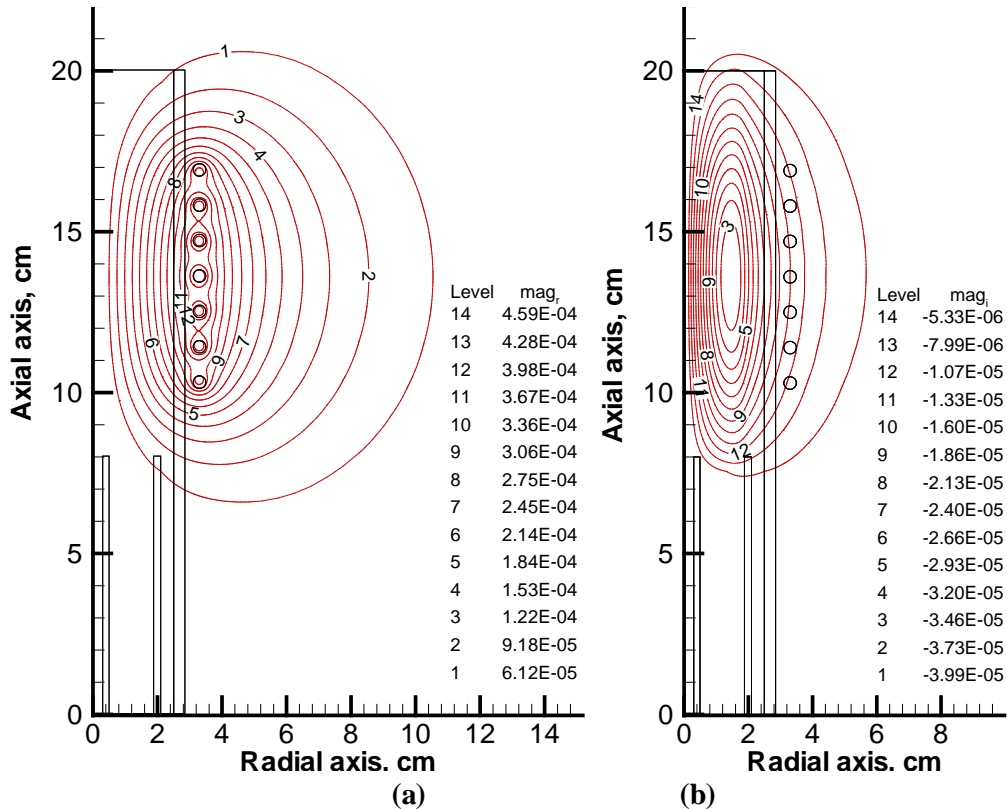


**Figure 7.2:** Contour of the vector potential ( $A H m^{-1}$ ) for the constant electrical conductivity load  $\sigma = 1500 \Omega^{-1} m^{-1}$ : (a) the real part, and (b) the imaginary part.

The radial profiles of the real parts of the axial magnetic field  $H_x$  and the induced current  $J_{ind}$  at the axial position  $x = 136$  mm for different electrical conductivity are shown in Fig. 7.3 (a) and (b), respectively. As expected, the results show that the magnetic field intensity in the center decreases with the increase of electrical conductivity. In Fig. 7.3 (b), there is no curve for the case of zero electrical conductivity because there is no induced current in the load. The radial profiles of the magnetic field and the induced current of argon plasma at the same axial position are also shown in Fig. 7.3 (a) and (b) for the purpose of comparison. It is noted that the curve for the plasma is similar to the curve of  $\sigma = 1500 \Omega^{-1} m^{-1}$ , which corresponds to the electrical conductivity of argon plasma at temperature of 8565K. It is also noted that for the case of argon plasma, the intensity of the axial magnetic field near the torch wall region ( $19 < r < 25$  mm) are slightly less than that in the cases with constant electrical conductivity loads. This is because in the plasma, small amount of current is also induced in this region (see Fig. 7.3 (b)), which generates the magnetic field with the opposite direction to that by the primary coil current. From Fig. 7.3 (b), the induced current density peak for the constant electric load occurs at the outer edge of the load ( $r = 19$  mm), while for the argon plasma, the peak occurs at  $r = 12$  mm.

The calculated axial magnetic field was then compared with the skin depth obtained from the analytic solution for semi-infinite slab load, which can be calculated from [Davises, 1979]:

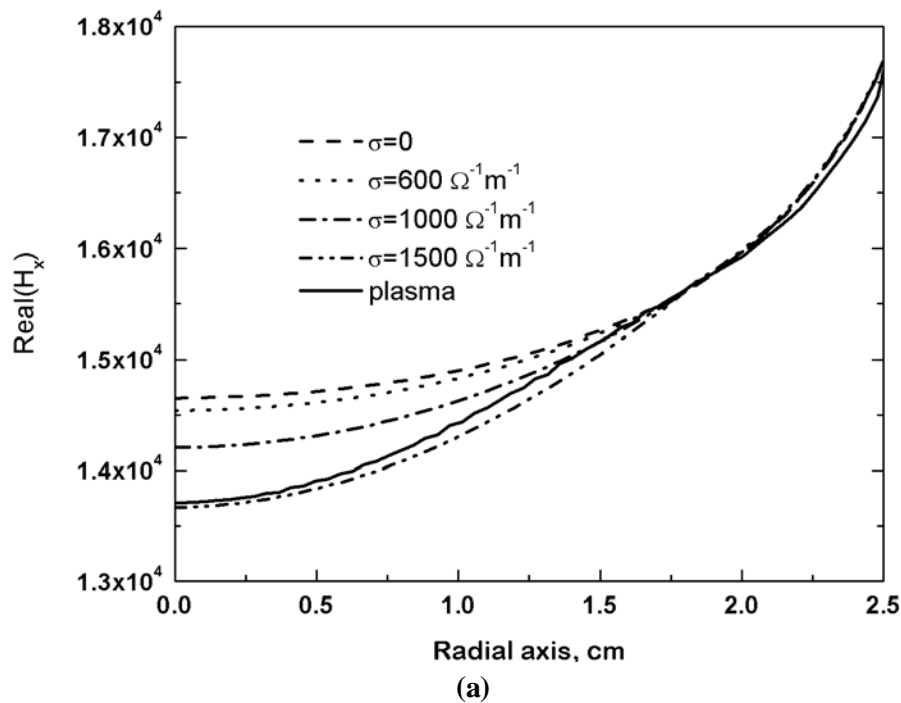
$$\delta = \sqrt{\frac{2}{\mu_0 \omega \sigma}} . \quad (7.1)$$

With an operating frequency of 333 kHz, the skin depths are 35.6, 27.6 and 22.5 mm when  $\sigma$  equals to 600, 1000 and  $1500 \Omega^{-1} m^{-1}$ , respectively. The profiles of the magnetic field as shown in Fig. 7.3 (a) are consistent with these values of the skin depth.

The computational result with zero electrical conductivity load (vacuum) is also compared with the analytic results. As shown in Fig. 7.3 (a), the axial magnetic field (imaginary part of the magnetic field is zero for this case) at the point of  $r = 0$  and  $x = 136$  mm, is  $1.47 \times 10^4 \text{ A m}^{-1}$ . The analytical result of  $H_x$  can be calculated from [Davises, 1979]:

$$H_x = \sum_{i=1}^7 \frac{I_i}{2} \frac{r_c^2}{r_i^3} = 1.56 \times 10^4 (\text{Am}^{-1}) \quad . \quad (7.2)$$

assuming that the seven-turn coil is infinitely thin, where  $I_i$  is the current in the coil,  $r_c$  and  $r_i$  are the coil radius and the distance from the field point to the ring respectively. The 6% error is reasonable and may come from the assumption of infinitely thin ring. This result proves that our electromagnetic model is quite accurate.



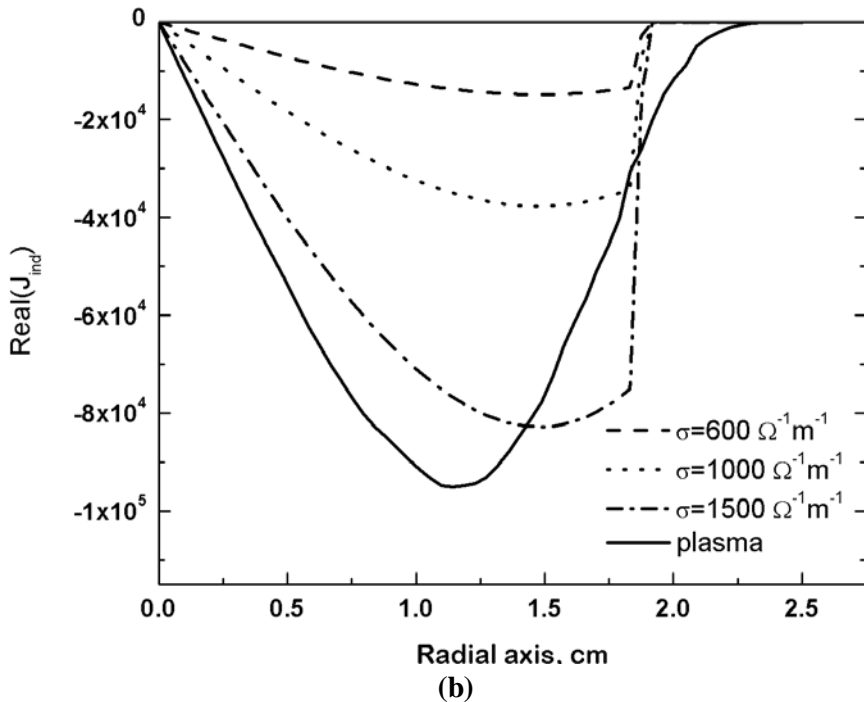


**Figure 7.3: Radial profiles at  $x = 136$  mm of (a) real part of the axial magnetic field  $H_x(\text{A m}^{-1})$ , (b) real part of the induced current density  $J_{\text{ind}}(\text{A m}^{-2})$ , for different electrical conductivities of the load.**

#### 7.4 Results of magnetic, flow and temperature fields of argon plasma

The information of the flow and temperature fields inside the plasma is of great importance for the particle behavior and the coating quality control. For plasma by RF induction heating, the electromagnetic field is the first concern, since it will characterize the plasma flow and temperature distribution. Using Eq. (2.36), the magnetic vector potential is solved for the argon plasma and the results are shown in Fig. 7.4 (a) and (b). The real part of the vector potential has the maximum magnitude near the current carrying coil; while the maximum magnitude of the imaginary part occurs at the plasma core since the induced current is largest in this region. The distribution of the imaginary part of the vector potential has only one peak, and this is due to the small pitch of the induction coil used. In comparison with Fig. 7.4, the distribution of vector potential is not symmetrical, especially for the imaginary part, because of the non-uniform electrical conductivity distribution (dependent on the plasma temperature field).

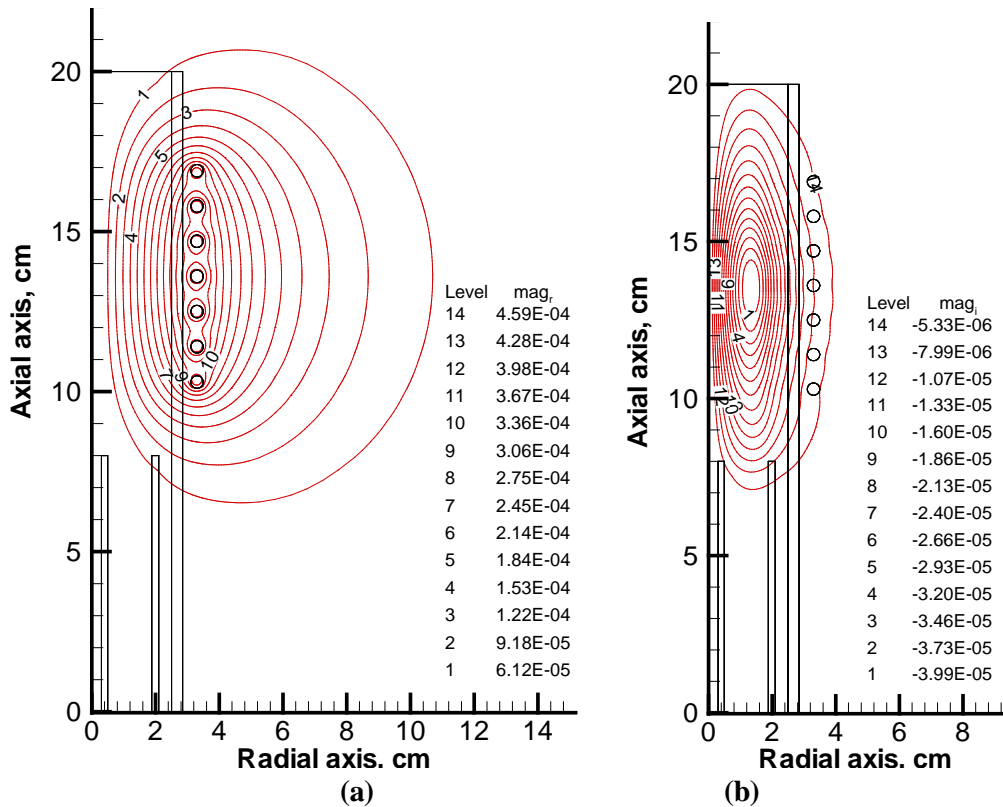


**Figure 7.4: Contour of the vector potential ( $A \text{ H m}^{-1}$ ) for the argon plasma: (a) the real part, and (b) the imaginary part.**

The operating conditions, such as power input, have great influence on the plasma behavior. As an example, two cases with different power input, 65 kW and 85 kW have been computed (other operating conditions are the same as listed in Table 7.1). The results of temperature and flow field are shown in Fig. 7.5 (a) and (b). Because of the small operating frequency and the resulting large skin depth, the flow is strongly affected by the Lorentz force and the recirculating flow is present in the torch. The temperature in the plasma core with the higher power input is larger, as a result of the increased Joule heating effect. Noted that at the downstream of the torch, the plasma temperature is lower for the higher power input case. This is attributed to that the stronger Lorentz force intensifies the recirculating flow in the torch (see Fig. 7.5 (b)). Figures 7.6 (a) and (b) show the contours of Joule heating and Lorentz force in the plasma of

65 kW and 85 kW. For the higher power, the magnitudes of Joule heating  $Q_J$  and radial Lorentz force  $F_r$  are larger.

It is noted that the temperature distributions in the torch have off-axis peak with the maximum temperature occurring at 11 mm and 13 mm for case of 65 kW and 85 kW respectively. This is due to the skin depth effect. The skin depths calculated from Eq. (7.1) are 22.5 mm and 19.5 mm, with the given  $\sigma = 1500 \Omega^{-1} \text{ m}^{-1}$  for 65 kW and  $\sigma = 2000 \Omega^{-1} \text{ m}^{-1}$  for 85 kW, respectively. According to Eckert [1974], the coupling efficiency is better if  $R/\delta \leq 1.75$ , where  $R$  is the torch radius. For these two cases, values of  $R/\delta = 1.1$  and 1.3 assure the good coupling of the magnetic field and the plasma field.

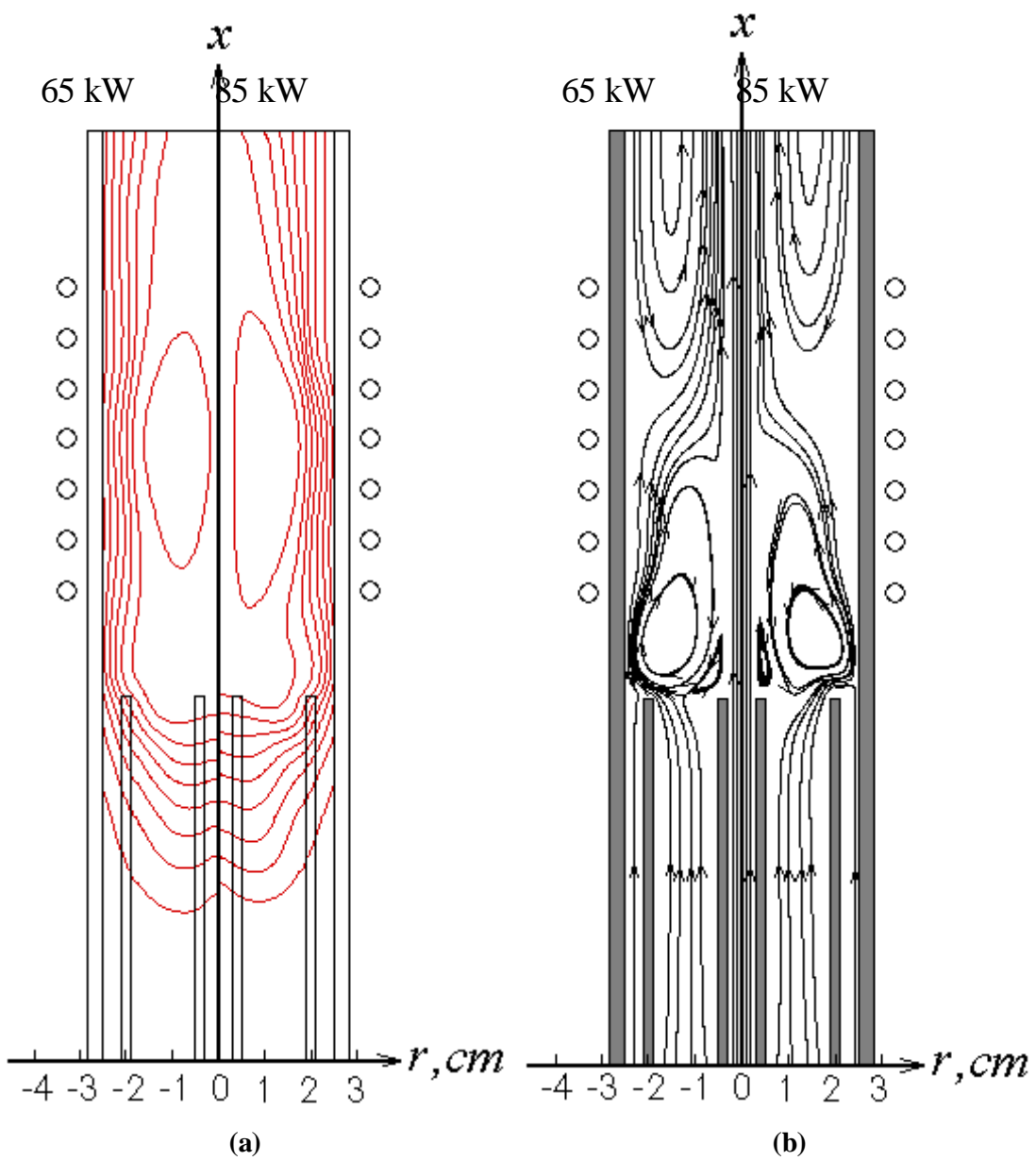


**Figure 7.5:** (a) Temperature contours of argon plasma with different power input: (Maximum = 10192 K, minimum = 1030 K, incremental value = 1018 K and operating conditions are given in Table 7.1); (b) Streamlines of the plasma flow fields with different power input.

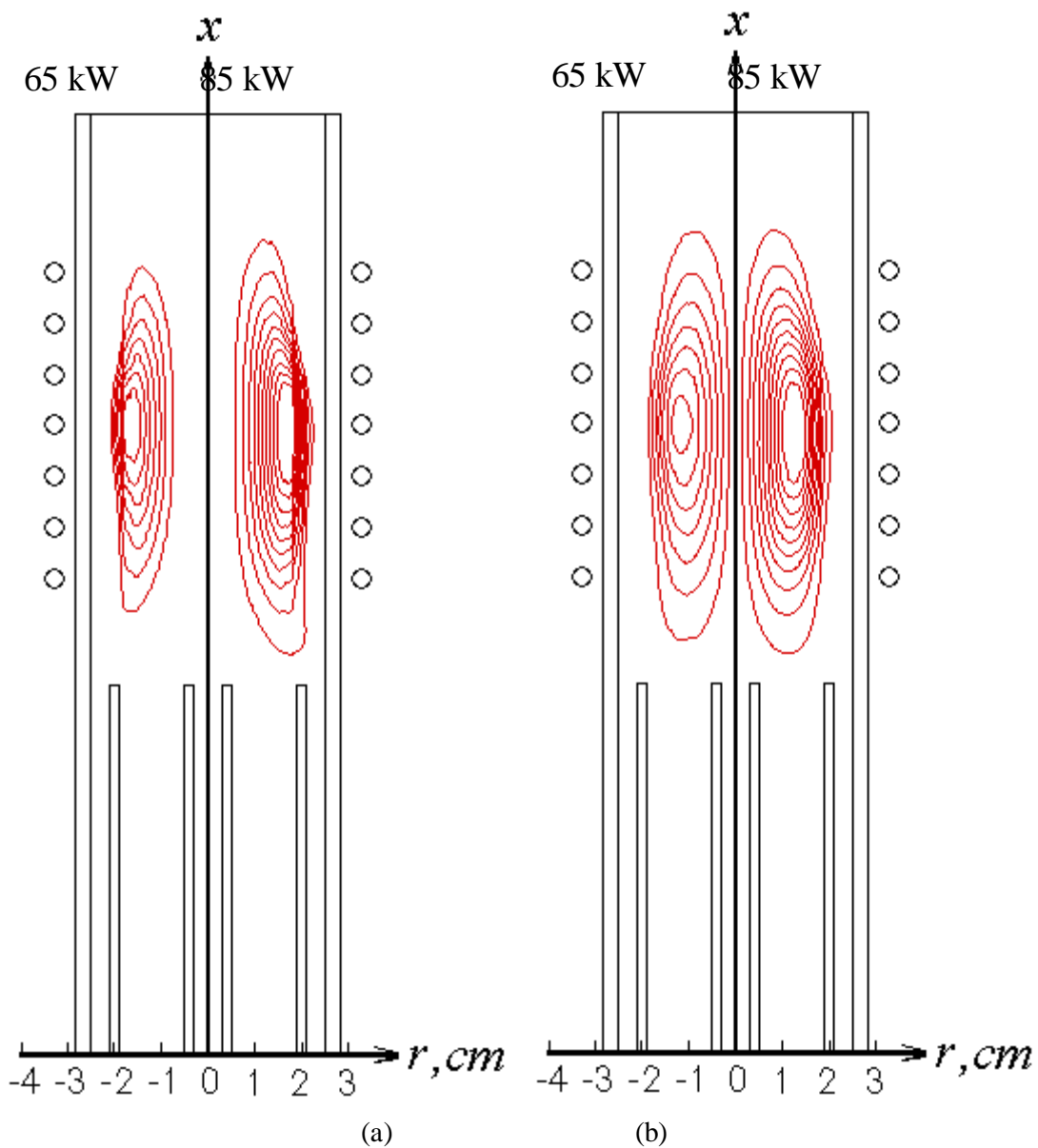


**Figure 7.6: (a) Contours of the Joule heating  $Q_J$  ( $\text{W m}^{-3}$ ) in the plasma for argon plasma with different power input: (Minimum =  $4.5 \times 10^7$ , incremental value =  $4.5 \times 10^7$ ); and (b) Contours of the radial Lorentz force  $F_r$  ( $\text{N m}^{-3}$ ): (Maximum = -600, incremental value = -600).**

## 7.5 Results of particle behaviors

### 7.5.1 Effects of particle injection position

The particle characteristics during flight, such as velocity and temperature, are very important to the coating property and quality. Figure 7.7 shows the ZrO<sub>2</sub> particle trajectory, velocity, surface and center temperatures during its flight in the induction plasma spray torch. Two particle injection positions are used: 8 cm and 10 cm. It is seen in Fig. 7.7, the initial injection position has strong effects on the particle trajectory, velocity and temperature. When the particle injection nozzle is located at the same level of the other two nozzles,  $x_{inj} = 8$  cm, the particles are entrained well directly into the hot core of the plasma region and being heated rapidly towards the melting point. At the downstream of their flight, the particles are dragged towards the axis by the recirculating flow in the plasma core. For the other injection position  $x_{inj} = 10$  cm, the particles flow more close to the axis and absorb less heating from the plasma, since the plasma temperature near the axis is low (see Fig. 7.5 (a)). As a result, the final particle diameters for these two cases are quite different. For example, the final particle sizes of 32 and 51  $\mu\text{m}$  are obtained for injection nozzle located at 8 cm and 10 cm respectively, with the same initial size of 60  $\mu\text{m}$ . Therefore, the particle injected at the position of 8 cm is overheated and 75 % of the mass is vaporized; and the particle injected at the position of 10 cm is a better condition for the economic consideration. Noted that in this case, the particles are injected at the nozzle center with an initial velocity of 11.8 cm/s and an injection cone angle of 15°. However, in the real case, the injected multiple particles have some stochastic distributions of injection position, velocity and angle. Some particles with small injection velocity and injection angle may not be able to be entrained into the plasma core, and may suffer from low heating and partially melting.

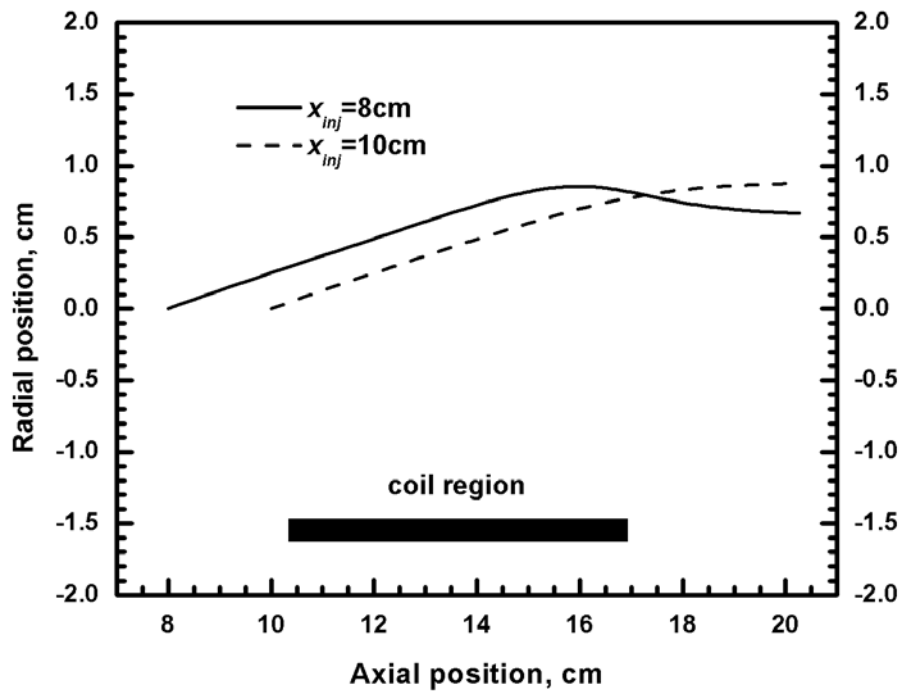
### 7.5.2 Effects of particle size

In the RF plasma spray, the particle size also plays an important role in the particle in-flight characteristics. Figure 7.8 shows the trajectory, velocity, surface and center temperatures of ZrO<sub>2</sub> particles with diameters of 60 and 80  $\mu\text{m}$ . These two particles are injected at axial location of 10 cm. As

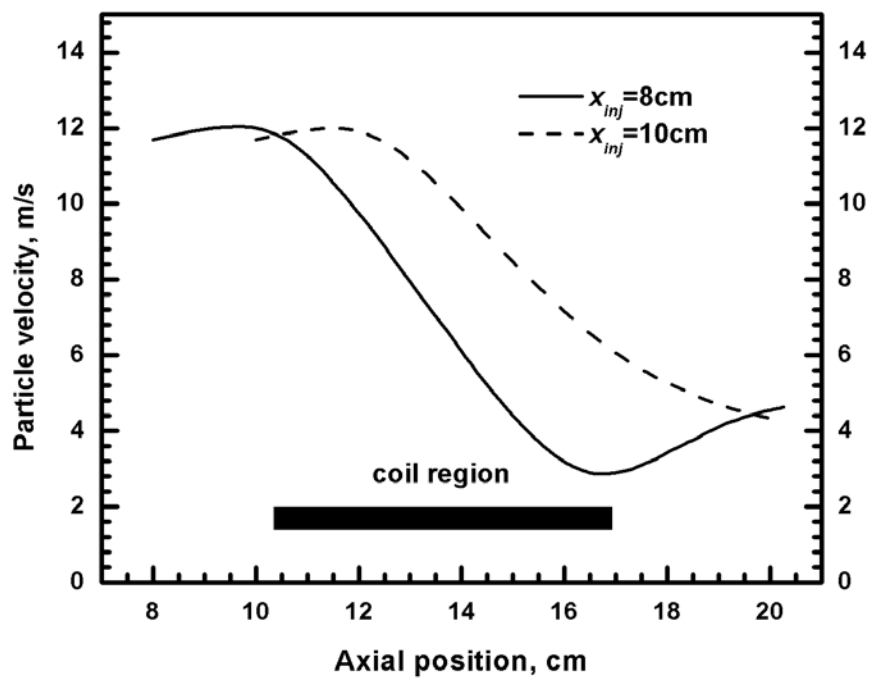
shown in Fig. 7.8(a), the particle size influences the particle trajectories significantly for the axial injection method of feedstock. Small particles tend to have less radial displacement due to its small inertia. Therefore, particles with different sizes will experience different thermal environment and will have different velocity and temperature. The results show that the large particle has lower temperature because of its large latent heat; while its velocity is higher, since they can be entrained better into the hot core of the plasma jet.

### 7.5.3 Multiple particles behavior

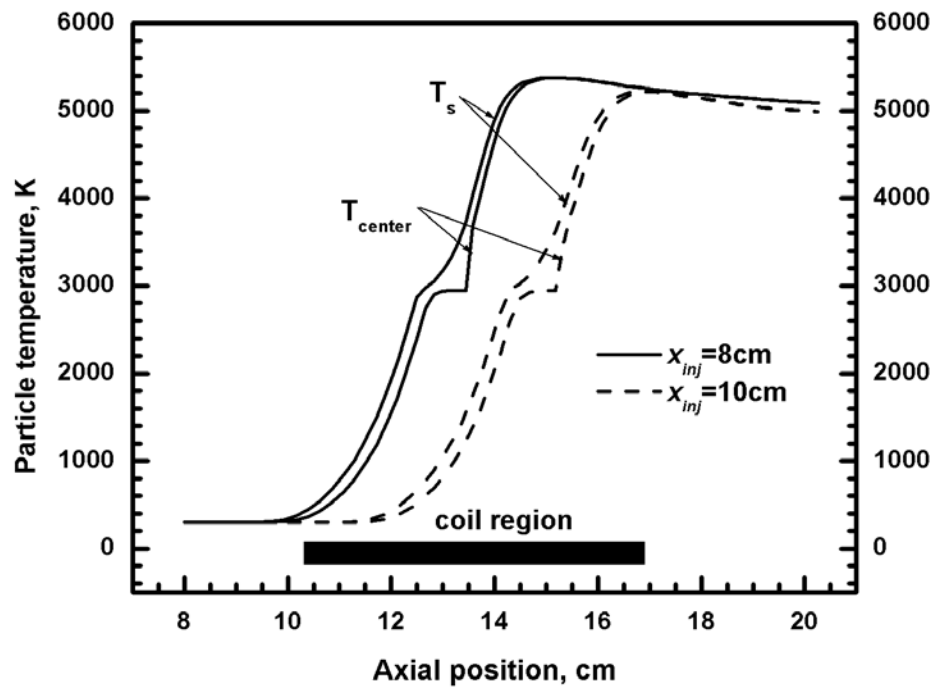
The multiple particles behaviors in RF plasma spray are also studied using simulation method. The stochastic scheme of multiple particle generation is used as details in Section 4.2. The initial  $\text{ZrO}_2$  particle diameter ranges from 50 to 110  $\mu\text{m}$ , with the average diameter of 64  $\mu\text{m}$ . Figure 7.9 shows the histograms for the particle velocity, temperature and diameter at the RF torch exit that is axially located at the position of 20.3 cm. The particle velocity is distributed between 4.2 to 15.6 m/s, with mean velocity of 9.4 m/s. The average particle temperature is 4379 K. Most particles are overheated up to 5000 K, while some large particles are difficult to be melted and stuck at the melting point of 2950 K. The results also show that the final particle diameters decrease dramatically as a result of in-flight particle evaporation, ranging from 34 to 110  $\mu\text{m}$ . The average diameter ends as 62  $\mu\text{m}$ .



(a)

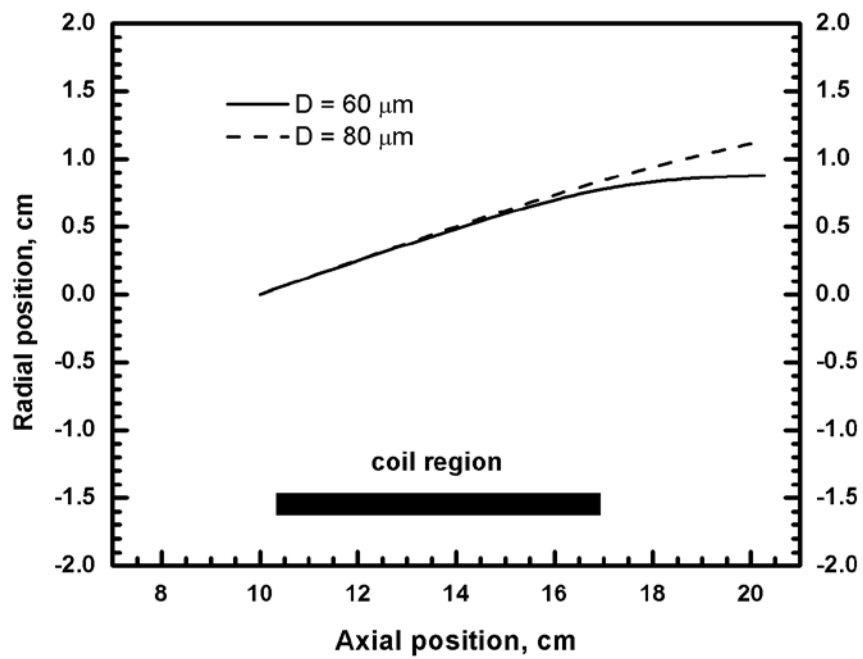


(b)

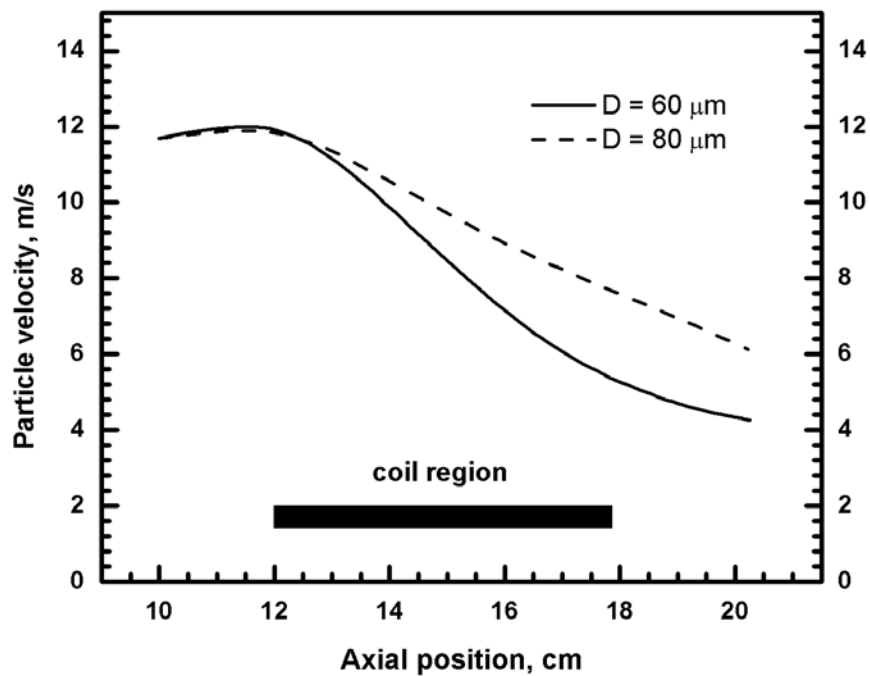


(c)

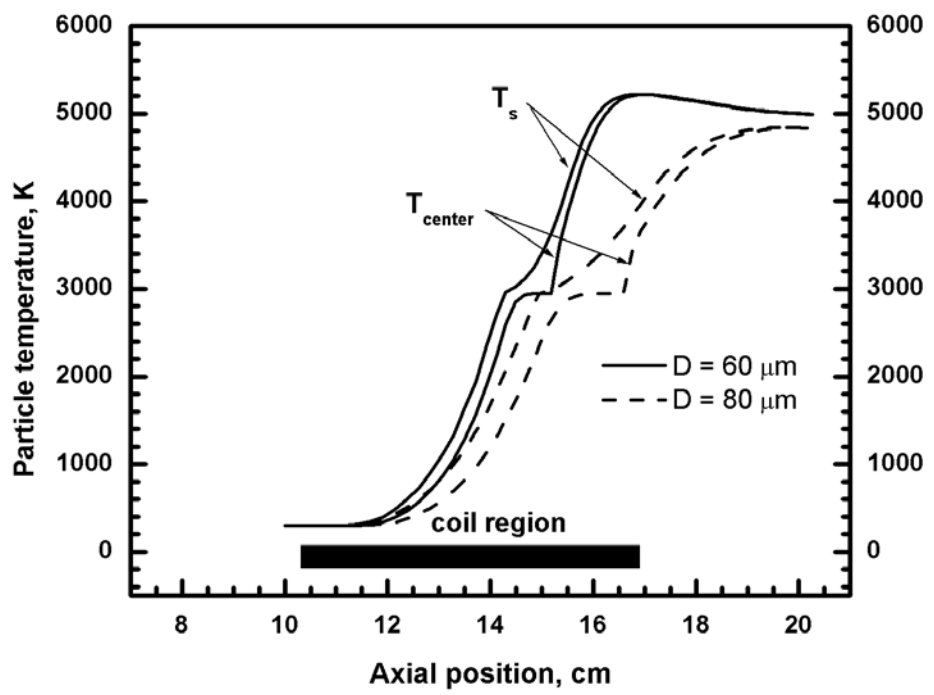
Figure 7.7: (a) Trajectory (b) velocity and (c) surface and center temperatures of  $\text{ZrO}_2$  particle in RF plasma spray with different injection location of 8 and 10 cm.



(a)



(b)



(c)

**Figure 7.8: (a) Trajectory (b) velocity and (c) surface and center temperatures of ZrO<sub>2</sub> particle in RF plasma spray with different diameter of 60 and 80  $\mu\text{m}$ .**

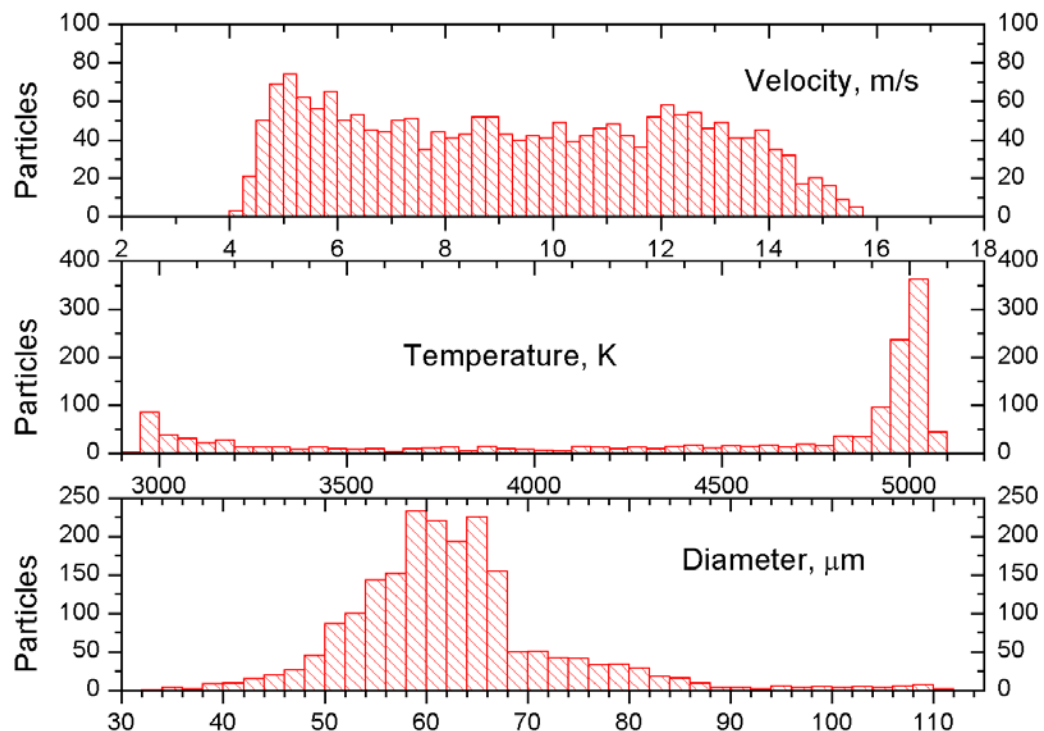


**Figure 7.9: Histograms for particle velocity, temperature and diameter of ZrO<sub>2</sub> particles in RF plasma spray with initial diameters ranging from 50 and 110  $\mu\text{m}$ .**

## **Chapter 8**

## **Conclusions and Recommendations**

### **8.1 Conclusions**

An advanced three-dimensional model for multi-component reacting DC plasma jet has been developed in this study, together with the interface tracked in-flight particle model. The radio frequency inductively coupled plasma has also been studied using a comprehensive numerical model for the electromagnetic field and the plasma flow. Using this integrated model, the numerical simulations have been carried out to predict the plasma field and the in-flight particle behaviors.

#### **8.1.2 3-D simulation of DC plasma spray**

An advanced three-dimensional model for multi-component reacting DC plasma jet has been presented in this study, together with the interface tracked in-flight particle model. The computational program has been enhanced to three-dimensional geometry of plasma jet so as to investigate the three-dimensional phenomena of plasma jet due to the radial injection of carrier gas and particles. The in-flight particle behaviors, such as melting, re-solidification, evaporation and oxidation have also been studied in the 3D geometry configuration under different operating conditions. The three-dimensional plasma jet with side injection of carrier gas and particles has been simulated. The effects of carrier gas on the plasma jet and particle behavior have been studied.

- Using the LAVA-P-3D code, a good agreement has been obtained between the simulation result and experimental data for the particle velocity.
- The carrier gas and particles loading, which are injected from the orthogonal injector above the plasma jet, introduce 3-D phenomena of plasma gas flow. The flow pattern of the plasma jet, especially in the downstream of the side injector, changes significantly due to the impact of the carrier gas jet. Numerical results show a shift of main plasma jet as the result of the side jet impact. It is also observed that side jet injection cools the plasma jet and slows the plasma jet motion in the axial direction of the plasma jet. The extent of plasma jet shift will be increased with an increase of carrier gas flow rate.

- By taking into account of carrier gas, we found that the particle behavior differs from the prediction by two-dimensional LAVA code. We observed a larger traverse velocity and distance, and lower particle temperature and velocity. Due to the interaction between carrier gas jet and the injected particles, the spray pattern predicted by LAVA-P-3D also differs from that by the simple 2D model. The current prediction matches better with the experimental data.
- Carrier gas flow rates affect the entrained particles behavior significantly. In the case of high carrier gas flow rate, the particles exhibit higher traverse velocities and deposit at lower position. Therefore, the change of particle trajectories, will affect the particle temperature and velocity as well.

### **8.1.2 2-D simulation of RF plasma spray**

A radio frequency inductively coupled plasma spraying process has been studied using a comprehensive numerical model for the electromagnetic field, plasma flow and the injected particle. To validate the numerical model of the electromagnetic field, computations have been carried out for the constant electrical conductivity load that is placed in the center of the coil. Numerical results were compared with the analytical solution and a good agreement has been achieved. The coupling between the electromagnetic field and the plasma field has been included in the model. Results show that certain selection of the operating conditions can achieve a proper skin depth and a good coupling of the electromagnetic field with the plasma. The particle behaviors, such as heating and acceleration, have also been simulated. The injection position and particle size has strong effects on the particle behavior. The results show that the particle injected from nozzle located at 10 cm downstream is better than injection from 8 cm for the better production yield.

### **8.1.3 Melting index**

Dimensionless group parameters, melting index and oxidation index, have been defined to describe particle melting status and in-flight particle oxide content based on experimentally measurable data. To fully melt a ceramic particle, the surface temperature should be much higher than the melting temperature due to the thermal resistance of the melt. Our analysis reveals that the total melting time is reciprocal to

the particle diameter and velocity, and the metal particle oxidation during in-flight is reciprocal to particle velocity and diameter square. Numerical simulations have been used to determine the unknown parameters in the melting index and oxidation index. Effects of the initial particle diameter on melting and oxidation behavior have also been studied. Melting index is found to be well correlated with the splat deposition efficiency. The splat fragmentation degree is found to be dependent primarily on particle Reynolds number. For the same Reynolds number, particles with a larger melting index will have less possibility to form fragmentation.

## 8.2 Recommendations

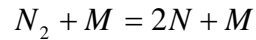
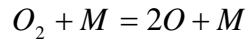
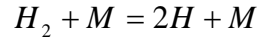
On the basis of the present explorations on the plasma jet and particles in flight, the following is recommended for the future work:

- For particles and its interaction with the plasma, the model is based on the 1-D spherical assumption. This assumption is questioned for porous materials that are commonly used, and more accurate model of energy transport would be required for the prediction of the porous particle temperature and its melting status.
- Current particle model is based on the pure materials. However, the alloy and composite materials are of great interest in many industrial applications. The advance models of phase change mechanisms for different component materials are recommended.
- For RF induction plasma spray, the liquid feedstock or precursor is often used for the deposition of nanostructure coating and material synthesis. The atomization process, which determines the droplet size and distribution, is of vital importance and should be included in the model.

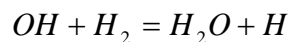
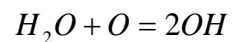
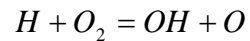
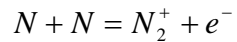
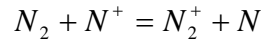
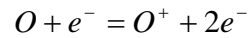
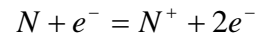
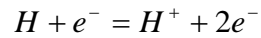
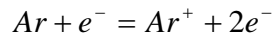
## Appendix

### A: Reaction Mechanisms for an Ar + H<sub>2</sub> Plasma into Air

Kinetic reactions:



Equilibrium reactions:



### B: Differential form of governing equations for DC plasma flame

If converting the vector differential operator to the differential form in the cylindrical coordinate ( $r, y, \theta$ ), the governing equations for DC plasma flame can then be written as follows. The continuity and species equations are:

$$\frac{\partial \rho}{\partial t} + \frac{1}{r} \frac{\partial(r\rho u)}{\partial r} + \frac{\partial(\rho v)}{\partial y} + \frac{1}{r} \frac{\partial(\rho w)}{\partial \theta} = 0, \quad (B.1)$$

$$= \frac{1}{r} \frac{\partial}{\partial r} \left[ \rho D r \frac{\partial}{\partial r} \left( \frac{\rho_i}{\rho} \right) \right] + \frac{\partial}{\partial y} \left[ \rho D \frac{\partial}{\partial y} \left( \frac{\rho_i}{\rho} \right) \right] + \frac{1}{r^2} \frac{\partial}{\partial \theta} \left[ \rho D \frac{\partial}{\partial \theta} \left( \frac{\rho_i}{\rho} \right) \right] + \dot{\rho}_i^c \quad (B.2)$$

$$\rho \left[ \frac{\partial u}{\partial t} + u \frac{\partial u}{\partial r} + v \frac{\partial u}{\partial y} + \frac{w}{r} \frac{\partial u}{\partial \theta} \right] = - \frac{\partial p}{\partial r} - \frac{\partial}{\partial r} \left( \frac{2}{3} \rho k \right) + \frac{\partial}{\partial r} \left( 2\mu \frac{\partial u}{\partial r} \right)$$

The momentum equations in the radial and  $\theta$ -directions are:

$$\begin{aligned} & \frac{\partial}{\partial y} \left( \mu \left( \frac{\partial v}{\partial y} + \frac{\partial v}{\partial r} \right) \right) + \frac{1}{r} \frac{\partial}{\partial \theta} \left[ \mu \left( \frac{\partial v}{r \partial \theta} + \frac{\partial v}{\partial r} - \frac{w}{r} \right) \right] + \frac{2\mu}{r} \left( \frac{\partial u}{\partial r} - \frac{u}{r} - \frac{1}{r} \frac{\partial w}{\partial \theta} \right) \\ & + \rho \frac{w^2}{r} + \frac{\partial}{\partial r} (\lambda \nabla \cdot \bar{u}) + F_{p,r} \end{aligned} \quad (B.3)$$

$$\begin{aligned} & \rho \left[ \frac{\partial v}{\partial t} + u \frac{\partial v}{\partial r} + v \frac{\partial v}{\partial y} + \frac{w}{r} \frac{\partial v}{\partial \theta} \right] = - \frac{\partial p}{\partial y} - \frac{\partial}{\partial y} \left( \frac{2}{3} \rho k \right) + \frac{1}{r} \frac{\partial}{\partial r} \left( \mu r \left( \frac{\partial v}{\partial r} + \frac{\partial u}{\partial y} \right) \right) \\ & + \frac{\partial}{\partial y} \left( 2\mu \frac{\partial v}{\partial y} \right) + \frac{1}{r} \frac{\partial}{\partial \theta} \left[ \mu \left( \frac{\partial v}{r \partial \theta} + \frac{\partial w}{\partial y} \right) \right] + \frac{\partial}{\partial y} (\lambda \nabla \cdot \bar{u}) + F_{p,y} \end{aligned} \quad (B.4)$$

$$\begin{aligned} & \rho \left[ \frac{\partial w}{\partial t} + u \frac{\partial w}{\partial r} + v \frac{\partial w}{\partial y} + \frac{w}{r} \frac{\partial w}{\partial \theta} \right] = - \frac{1}{r} \frac{\partial p}{\partial \theta} - \frac{1}{r} \frac{\partial}{\partial \theta} \left( \frac{2}{3} \rho k \right) \\ & + \frac{\partial}{\partial r} \left( \mu \left( \frac{\partial w}{\partial r} + \frac{1}{r} \frac{\partial u}{\partial \theta} - \frac{w}{r} \right) \right) + \frac{\partial}{\partial y} \left( \mu \left( \frac{\partial w}{\partial y} + \frac{\partial v}{r \partial \theta} \right) \right) + \frac{1}{r^2} \frac{\partial}{\partial \theta} \left[ 2\mu \left( \frac{\partial w}{\partial \theta} + u \right) \right] \\ & + \frac{2\mu}{r} \left( \frac{1}{r} \frac{\partial u}{\partial \theta} + \frac{\partial w}{\partial r} - \frac{w}{r} \right) - \rho \frac{uw}{r} + \frac{1}{r} \frac{\partial}{\partial \theta} (\lambda \nabla \cdot \bar{u}) + F_{p,\theta} \end{aligned} \quad (B.5)$$

The energy conservation equation is:

$$\rho \left[ \frac{\partial e}{\partial t} + u \frac{\partial e}{\partial r} + v \frac{\partial e}{\partial y} + \frac{w}{r} \frac{\partial e}{\partial \theta} \right] = -p \nabla \cdot \bar{u}$$

$$+ \frac{1}{r} \frac{\partial}{\partial r} \left( r \frac{K}{c_v} \frac{\partial e}{\partial r} \right) + \frac{\partial}{\partial y} \left( \frac{K}{c_v} \frac{\partial e}{\partial y} \right) + \frac{1}{r^2} \frac{\partial}{\partial \theta} \left( \frac{K}{c_v} \frac{\partial e}{\partial \theta} \right) + \rho \varepsilon + \dot{Q}_c - \dot{Q}_R + \dot{Q}_p \quad (B.6)$$

## References

- Ageorges, A., P. Fauchais, "Oxidation of stainless steel particles with and without an alumina shell during their flight in a plasma jet", *High Temperature Material Processes* 4 323-337 (2000)
- Ahmed, A. M, Rangel, R. H., Sobolev, V.V., and Guilemany, J. M., "In-flight oxidation of composite powder particles during thermal spraying," *International Journal of Heat and Mass Transfer*, Vol.44, pp.4667-4677 (2001)
- Ahmed, I., and Bergman, T.L., "Simulation of thermal plasma spraying of partially molten ceramics: effect of carrier gas on particle deposition and phase change phenomena", *Transaction of the ASME*, Vol.123, pp.188-196, (2001)
- Ahmed, I., and Bergman, T.L., "Three-dimensional simulation of thermal plasma spraying of partially molten ceramic agglomerates," *Journal of Thermal Spray Technology*, Vol.9, pp.215-224, (2000)
- Amsden, A.A., P.J. O'Rourke, T.D. Butler, "KIVA-II: a computer program for chemically reactive flows and fuel sprays," Report LA-11560-MS. Los Alamos National Laboratory, May 1989
- Bergmann, D., U. Fritsching, K. Bauckhage, "A mathematical model for cooling and rapid solidification of molten metal droplets," *Int. J. Therm. Sci.* 39, 53-62 (2000)
- Bernardi, D., V. Colombo, E. Ghedini, A. Mentrelli, and T. Trombetti, "3-D numerical simulation of fully-coupled particle heating in ICPTs," *Eur. Phys. J. D* 28, pp.423-433, (2004)
- Boulos, M.I., "RF induction plasma spraying: state-of-the-art review," *Journal of Thermal Spray Technology*, Vol.1, pp.33-48, (1991)
- Boulos, M.I., "The inductively coupled radio frequency plasma", *High Temperature Material Processes*, Vol.1, pp.17-39, (1997)
- Boulos, M.I., P. Fauchais, A. Vardelle, and E. Pfender, "Fundamentals of plasma particle momentum and heat transfer," *Plasma Spraying, Theory and Application*, (ed.) R. Suryanarayanan, (Pub.) Singapore: World Scientific, pp.3-60, (1993)

- Boulos, M.I., P. Fauchais, and E. Pfender, "Thermal plasmas," Plenum Pr, 1994
- Cai, M., D. A. Haydar, A. Montaser and J. Mostaghimi, "Computer simulation of argon-nitrogen and argon-oxygen inductively coupled plasmas", *Spectrochimica Acta Part B* 52 (1997) 369-386.
- Cai, W.D., E.J. Lavernia, "Modeling of porosity during spray forming," *Materials Science and Engineering*, A226-228, 8-12 (1997)
- Cao, M., F. Gitzhofer, D.V. Gravelle, R. Henne, and M.I. Boulos, "A torch nozzle design to improve plasma spraying techniques," *Plasma Sources Science & Technology*, Vol.6, pp39-45, (1997)
- Chang, C. H. and Ramshaw, J. D., "Modeling of nonequilibrium effects in a high-velocity nitrogen-hydrogen plasma jet," *Plasma Chemistry and Plasma Processing*, Vol. 16, No. 1, pp.4s-17s (1996)
- Chang, C.H. and E. Pfender, "Nonequilibrium modeling of low-pressure argon plasma jets: Part II: turbulent flow," *Plasma Chemistry and Plasma Processing*, Vol.10, p.493 (1990)
- Chang, C.H. and Ramshaw, J.D., "Numerical simulations of Argon plasma jets flowing into cold air," *Plasma Chemistry and Plasma Processing*, Vol.13, pp.189-209 (1993)
- Chang, C.H., R.L. Moore, "Numerical simulation of gas and particle flow in a high-velocity oxygen-fuel (HVOF) torch," *Journal of Thermal Spray Technology*, 4 (1995) 358-366
- Chase, J. D., "Theoretical and experimental investigation of pressure and flow in the induction plasma", *Journal of Applied Physics*, 42(12) pp.4870-4879, 1971
- Chen, X and Pfender, E., "Heat transfer to a single particle exposed to a thermal plasma," *Plasma Chemistry and Plasma Processing*, Vol.2, No.2, pp. 185-212 (1982)
- Chen, X. and Pfender, E., "Behavior of small particles in a thermal plasma flow," *Plasma chemistry and plasma processing*, Vol. 3, No. 3, pp.351-366 (1983)
- Chen, X. and Pfender, E., "Effect of the Knudsen number on heat transfer to a particle immersed into a thermal plasma," *Plasma Chemistry and Plasma Processing*, Vol.3, No.1, pp.97-113 (1983)

Choi, H., B. Yoon, H. Kim, C. Lee, "Isothermal oxidation of air plasma spray NiCrAlY bond coatings," *Surface and Coating Technology*, Vol.150, pp.297-308, 2002

Cochelin, E., Borit, F., Frot, G., Jeandin, M., Decker, L., Jeulin, D., Altawee, B., Michaud, V., and Noel, P., "Oxidation and particle deposition modeling in plasma spraying of Ti-6Al-4V/Sic Fiber Composites," *Journal of Thermal Spray Technology*, Vol. 8, p117-124 (1999)

Crowe, C. T., Sharma, M. P., and Stock, D.E., "The particle-source-in-cell model for gas-droplet flows," *Journal of fluids engineering*, Vol. 99, No.2, pp. 325-332 (1977)

Delplanque, J.-P., Lavernia, E.J., and Rangel, R.H., "Analysis of in-flight oxidation during reactive spray atomization and deposition processing of aluminum," *Journal of Heat Transfer, Heat Transfer Division*, Vol.122, p.126-133, 2000

Dembovsky, V., "Plasma Metallurgy: The Principles (Materials Science Monographs Vol. 23)," Elsevier Science Ltd, 1985

Desilets, M., J.-F. Bilodeau and P. Proulx, "Modeling of the reactive synthesis of ultra-fine powders in a thermal plasma reactor," *Journal of Physics D: Applied Physics*, Vol. 30, pp. 1951-1960, (1997)

Devi, P.S., Y. Lee, J. Margolis, J. B. Parise, S. Sampath, H. Herman and J.C. Hanson, "Comparison of citrate-nitrate gel combustion and precursor plasma spray processes for the synthesis of yttrium aluminum garnet," *J. Mater. Res.*, Vol. 17 (11), pp.2846-2851, (2002)

Dibble, K., J.R.T. Branco, S. Sampath, C.C. Berndt, "Iron-based deposits produced by high-throughout water stabilized plasma," *Thermal Spray: Practical Solutions for Engineering Problems*, (ed.) C.C. Berndt, (Pub.) ASM Int. OH, USA, pp.413-418, 1996

Dobler, K., H. Kreye, R. Schwetzke, Oxidation of stainless steel in the high velocity oxy-fuel process, *Journal of Thermal Spray Technology* 9(2000) 407-413

Dussoubs, B., A. Vardelle, G. Marlaux, N.J. Thermelis, and P. Fauchais, "Modeling of plasma spraying of two powders," *Journal of Thermal Spray Technology*, Vol.10, (1), p.105-110, 2001

Dussoubs, G. Marlaux, B., A. Vardelle, M. Vardelle, and P. Fauchais, "D.C. plasma spraying: effects of arc root fluctuations on particle behavior in the plasma jet", *High Temp. Material Processes* 3 (1999) 235-254

Eckert, H. U., "The induction arc: a state-of-art review", *High Temperature Science*, 6 (1974) p.99-134.

Escure, C., M. Vardelle, and P. Fauchais, Experimental and theoretical study of the impact of alumina droplets on cold and hot substrates, *Plasma Chem. Plasma Processing*, 2003, Vol. 23(2), pp. 185-221.

Espie, G., Fauchais, P., Hannoyer, B., Labbe, JC, and Vardelle, A., "Effect of metal particles oxidation during the APS on the wettability," *Heat and Mass Transfer under Plasma Conditions, Annals of the New York Academy of Sciences*, Vol. 891, pp.143-151 (1999)

Espie, G., Fauchais, P., Labbe, JC, and Vardelle, A., "Oxidation of iron particles during APS: effect of the process on formed oxide wetting of droplets on ceramics substrates", in *Thermal Spray 2001: New Surfaces for a New Millennium*, (ed.) C.C. Berndt, K.A. Knor, and E.F. Lugscheider, (Pub.) ASM Int. Ohio, USA, pp.821-827, 2001

Faeth, G. M., "Evaporation and combustion of sprays," *Prog. Energy Combustion*, Vol. 9, pp.1-76 (1983)

Fauchais, P., A. Vardelle, Heat, mass and momentum transfer in coating formation by plasma spraying, *Int. J. Therm. Sci.* (2000) 39. P852-870

Fauchais, P., and A. Vardelle, "Pending problems in thermal plasmas and actual development," *Plasma Phys. Control. Fusion* 42 (2000) B365-B383

Fauchais, P., J.F. Coudert, and M. Vardelle, "Diagnostics of plasma spray process and derived on-line control", *High Temp. Material Processes* 6 (2002) 247-265

Fauchais, P., J.F. Coudert, M. Vardelle, A. Vardelle, and A. Denoirjean, "Diagnostics of thermal spraying plasma jets," *Journal of Thermal Spray Technology*, Vol(1), pp.117-128, 1992

Fauchais, P., Vardelle, A., Dussoubs, B., "Quo Vadis Thermal Spraying?" in *Thermal Spray 2001: New Surfaces for a New Millennium*, (ed.) C.C. Berndt, K.A. Knor, and E.F. Lugscheider, (Pub.) ASM Int. Ohio, USA, pp.1-32, 2001

Favre, A., "Statistical equations of turbulent gases," in *Problems of Hydrodynamics and Continuum Mechanics*, Society for Industrial and Applied Mathematics, Philadelphia, 237 (1969)

Fincke, J.R., C.H. Chang, W.D. Swank, D.C. Haggard, "Entrainment and demixing in subsonic thermal plasma jets: comparison of measurements and predictions", *Int. J. Heat Mass Transfer* 37 pp.1673-1682, 1994

Fincke, J.R., W.D. Swank, and D.C. Haggard, "More on the influence of injector geometry and carrier gas flow rate on spray pattern and particle temperature," *International Thermal Spray Conference 2000 Proceeding*, Edited by C.C. Berndt, ASM Inter., Materials Park, OH (2000)

Fincke, J.R., W.D. Swank, and D.C. Haggard, "The influence of injector geometry and carrier gas flow rate on spray pattern," in *Thermal Spray: A United Forum for Scientific and Technological Advances*, Proceedings of the National Thermal Spray Conference, USA, (ed.) C.C. Berndt, (pub.) ASM Int. OH, USA, pp.335-342, 1997

Fincke, J.R., W.D. Swank, R.L. Bewley, D.C. Haggard, M. Gevelber, and D. Wroblewski, "Diagnostics and control in the thermal spray process", *Surface And Coating Technology*, Vol 146-147, pp.537-543, 2001

Fiszdon, J. K., "Melting of powder grains in a plasma flame," *Journal of Heat Transfer*, Vol.22, pp. 749-761, 1979

Freslon, A., "Plasma spraying at controlled temperature and atmosphere," in *Advances in Thermal Spray Science and Technology*, (eds.) C.C. Berndt and S. Sampath, (Pub.) ASM Int. OH, USA, pp.57-63, 1995

Gulbransen, E.A., K.F. Andrew, F.A. Brassart, "Oxidation of molybdenum 550°C to 1700°C," *Journal of The Electrochemical Society*, 110(1963) 952-959

Hackett, C.M., and G.S. Settles, "Turbulent mixing of the HVOF thermal spray and coating oxidation," in *Thermal Spray Industry Applications*, (Eds.) Christopher C. Bernt and Sanjay Sampath, ASM International, Materials Park, Ohio (1994) 307-312

Han, K.S., M.K. Chung and H.J. Sung, "Application of Lumley's drag reduction model to two-phase gas-particle flow in a pipe," *Trans. ASME, J. Fluids Eng.*, Vol 113 (1991) p 130-136

Hassan, B., A.R. Lopez, W.L. Oberkampf, "Computational analysis of a three-dimensional high-velocity oxygen fuel thermal spray torch," *Journal of Thermal Spray Technology*, Volume 7(1) March 1998, P71-77

He, J., Ice, M., and Lavernia, E., "Particle melting behavior during high-velocity oxygen fuel thermal spraying," *Journal of Thermal Spray Technology*, Vol.10, pp.83-93 (2001)

Heimann, R.B., *Plasma Spray Coating*, 1996

Herberlein J., Electrode phenomena in plasma torches, in: *Fauchais P., van der Muller J., Heberlein J. (Eds.), Heat and Mass Transfer Under Plasma Conditions*, Annals of the New York Academy of Sciences 891 (1999) 14-27.

Herman, H., and S. Sampath, "Thermal spray coatings (Chapter 10)," in (Eds.) K. H. Stern, *Metallurgical and Ceramic Protective Coatings*, 1996

Herman, H., S. Sampath, and R. McCune, "Thermal spray: Current status and future trends", *Material Science Bulletin*, 25 (7), pp. 17-25, 2000

Huang, P.C., J.V. Heberlein, and E. Pfender, "A two-fluid model of turbulence for a thermal plasma jet," *Plasma Chemistry and Plasma Processing*, Vol15, pp.25-46, 1995

Hurevich, V., Smurov, I., and Pawlowski, L., "Theoretical study of the powder behavior of porous particles in a flame during plasma spraying", *Surface and Coatings Technology* 151-152 (2002) 370-376

Janisson, S., Vardelle, A., Coudert, J.F., Meilot, E., Pateyron, B., and Fauchais, P., "Plasma spraying using Ar-He-H<sub>2</sub> gas mixture," *Journal of Thermal Spray Technology* (8), pp.545-552, (1999)

Jankovic, M., Mostaghimi, J., "A new nozzle design for DC plasma spray guns," *Plasma Chemistry and Plasma Processing*, Vol.15, pp.607-628 (1995)

Kaddani, A., Zahrai, S., Delalondre, C., Simonin, O., "Three-dimensional modeling of unsteady high-pressure arcs in argon," *J. Phys. D: Appl. Phys.* 28, p.2294-2305 (1995)

Kolman, B., Forman, J., Dubsky, J. and Charaska, P., "Homogeneity studies of powders and plasma-sprayed deposits," *Mikrochimica Acta* 114/115, pp.335-442 (1994)

Kyoung, D.K., and S.H. Hong, "Numerical analysis of shroud gas effects on air entrainment into thermal plasma jet in ambient atmosphere of normal pressure," *Journal of Applied Physics*, 85 (9) pp.6373-6380, (1999)

Lau, M. L., J. He, R. Schweinfest, M. Ruhle, C.G. Levi and E.J. Lavernia, "Synthesis and characterization of nanocrystalline Cu-Al coatings", *Materials Science and Engineering A* 347, pp. 231-242, 2003.

Lau, M.L., E. Strock, A. Fabel, C. J. Lavernia and E. J. Lavernia, "Synthesis and characterization of nanocrystalline Co-Cr coatings by plasma spraying", *NanoStructured Materials*, 10 (5), pp. 723-730, 1998.

Lauder, B.E., and Spalding, D. B., *Mathematical models of turbulence*, Academic Press, New York, 1972.

Law, C.K., "Recent advances in droplet vaporization and combustion," *Prog. Energy Combustion*, Vol.8, pp.171-201, 1982.

Lee, Y. C., "Modeling work in thermal spraying processing," PhD thesis, University of Minnesota, 1984

Lee, Y. C., Hsu, K.C. and Pfender, E., "Modeling of particles injected into a D.C. plasma jet," *Proceeding of 5<sup>th</sup> International Symposium on Plasma Chemistry*, Vol.2, pp.795, (1981)

Leylavergne, M., B. Dussoubs, A. Vardelle, and N. Goubot, "Comparison of plasma-sprayed coatings produced in argon or nitrogen atmosphere," *Journal of Thermal Spray Technology*, Vol. 7(4), December 1998, P527

Li, H.-P. and Chen, X., "Three-dimensional simulation of a plasma jet with transverse particle and carrier gas injection," *Thin Solid Films*, Vol. 390, pp.175-180 (2001).

Li, H.-P. and Chen, X., "Three-dimensional simulation of the turbulent plasma jet impinging upon a flat plate and with transverse particle and carrier gas injection", *Plasma Chemistry and Plasma Process*, Vol. 22, pp.27-57 (2002)

Li, K.I., M. Vardelle, A. Vardelle, and P. Fauchais, "Vaporization of metal powders in plasma sprays," *Thermal Spray: Practical Solutions for Engineering Problems*, (ed.) C.C. Berndt, (Pub.) ASM Int. OH, USA, pp.547-552, 1996

Margolies, J., "Development and evaluation of a radio frequency induction plasma facility for the processing of zirconia", M.S. thesis, State University of New York at Stony Brook, 1998.

Mariaux, G, Fauchais P, Vardelle A, Pateyron B, "Modeling of the plasma spray process: from powder injection to coating formation," *High Temperature Material Processes*, Vol. 5(1), pp.61-85, 2001

Mariaux, G., E. Legros, A. Vardelle, "Modeling of coating formation and heat flux to substrate by particles and plasma jet in plasma spraying," in *Thermal Spray 2003: Advancing the Science & Applying the Technology*, (Ed.) C. Moreau and B. Marple, ASM Int. OH, USA, 895-903 (2003)

Moreau, C., P. Gougeon, A. Burgess and D. Ross, "Characterization of particle flows in an axial injection plasma torch," *Advances in Thermal Spray Science and Technology*, (eds.) C.C. Berndt and S. Sampath, (Pub.) ASM Int. OH, USA, pp.141-147, 1995.

Neiser, R.A., M.F. Smith, R.C. Dykhuizen, "Oxidation in wire HVOF-sprayed steel," *Journal of Thermal Spray Technology*, 7(1998) 537-545

Njah, Z., J. Mostaghimi, M. Faghri and M. Boulos, "Study of 3-D mixing of a cold jet with a traverse plasma stream," *Int. J. Heat Mass Transfer* 36(16) (1993) 3897-3907

O'Rourke, P.J., "Statistical properties and numerical implementation of a model for droplet dispersion in a turbulent gas," *Journal of Computational Physics* 83 345-360 (1989)

Park, J.H., E. Pfender, C.H. Chang, "Reduction of chemical reactions in Nitrogen and Nitrogen-Hydrogen plasma jets flowing into atmosphere air," *Plasma Chemistry and Plasma Processing*, Vol. 20, p.165-181 (2000)

Pfender, E., Y.C. Lee, "Particle dynamics and particle heat and mass transfer in thermal plasma. Part I. The motion of a single particle without thermal effects," *Plasma Chemistry and Plasma Processing*, Vol.5, No.3, 1985.pp.211-237

Proulx, P., J. Mostaghimi, and M. I. Boulos, "Radiative energy transfer in induction plasma modeling", International Journal of Heat and Mass Transfer, 34 (10), pp. 2571-2579, 1991.

Prystay, M., P. Gougeon, C. Moreau, "Structure of plasma-sprayed zirconia coatings tailored by controlling the temperature and velocity of the sprayed particles," *Journal of Thermal Spray Technology*, Volume 10(1), pp.67-75, 2001

Rahmane, M., G. Soucy and M. I. Boulos, "Mass Transfer in induction plasma reactors", Int. J. of Heat Mass Transfer. 37 (1994) 2035-2046.

Ramachandran, K., and H. Nishiyama, "Fully coupled 3D modeling of plasma-particle interactions in a plasma jet", *Thin Solid Films*, 2004.

Ramachandran, K., and H. Nishiyama, "Three-dimensional effects of carrier gas and particle injections on the thermo-fluid fields of plasma jets," *J. Phys. D: Applied Physics* Vol.35, pp. 307-317 (2002)

Ramachandran, K., Sato, T., and H. Nishiyama, "3D modeling of evaporation of water injected into a plasma jet", *International Journal of Heat and Mass Transfer* 46 pp. 1653-1663, (2003)

Ramshaw, J.D. and Chang, C.H., "Iteration scheme for implicit calculation of kinetics and equilibrium chemical reaction in fluid dynamics," *Journal of Computational Physics*, Vol. 116, pp. 359-364 (1995)

Ramshaw, J.D., and Chang, C.H., "Computational fluid dynamics modeling of multi-component thermal plasmas," *Plasma Chemistry and Plasma Processing*, Vol. 12, pp.299-324 (1992)

Rat, V., P. Andre, J. Aubreton, M.F. Elchinger, P. Fauchais and D. Vacher, "Transport coefficients including diffusion in a two-temperature argon plasma", *Journal of Physics D: Applied Physics*, Vol.35, pp.981-991, 2002

Reynolds W.C. and Cebeci, T., Calculation of turbulent flows, in *Turbulence, Topics in Applied Physics*, 12, ed. B P. Bradshaw, Springer-Verlag, Berlin, Heidelberg, New York, 1976

Scott, D.A, P. Kovitya, and G. N. Haddad, "Temperatures in the plume of a dc plasma torch," *Journal Applied Physics*, Vol. 66, p.5232, 1989

Selezneva, S. E. and M. I. Boulos, "Supersonic induction plasma jet modeling", Nuclear Instruments and Methods in Physics Research B 180 (2001) 306-311.

Shaeffer J.F., "Swirl Arc: a model of swirling, turbulent radiative arc heater flow fields," *AIAA J.*, 16(10), 1068 (1989)

Shan, Y. and J. Mostaghimi, "Numerical simulation of aerosol droplets desolvation in a radio frequency inductively coupled plasma", *Spectrochimica Acta B* 58, pp.1959-1977, 2003.

Shigeta, M., T. Sato, H. Nishiyama, "Computational simulation for a particle-laden RF inductively coupled plasma with seeded potassium", *Int. J. of Heat Mass Transfer*. 47 (2004) 707-716.

Smith, M.F., R.C. Dykhuisen, and R.A. Neise: in *Thermal Spray: A United Forum for Scientific and Technological Advances*, Proceedings of the National Thermal Spray Conference, USA, (ed.) C.C. Berndt, (pub.) ASM Int. OH, USA, pp.885-893, 1997.

Sobolev, V.V., and Guilemany, J.M., "Effect of oxidation on droplet flattening and splat-substrate interaction in thermal spraying," *Journal of Thermal Spray Technology*, Vol. 8, pp.523-530 (1999)

Sobolev, V.V., Guilemany, J.M., "Prediction of powder particle behavior during high-velocity oxyfuel spraying," *Journal of Thermal Spray Technology* 4(3) 287 (1995)

Tanaka, Y. and T Sakuta, "Chemically non-equilibrium modeling of N<sub>2</sub> thermal ICP at atmospheric pressure using reaction kinetics", *J. Phys. Appl. D*: 35 (2002) 468-476.

Tawfik, H.H. and F. Zlmmerman, "Mathematical Modeling of the Gas and Powder Low in HVOF Systems," *Journal of Thermal Spray Technology*, Volume 6(3) September 1997.

Thomson, I., V. Pershine, J. Mostaghimi, and S. Chandra, "Experimental testing of a curvilinear nozzle design for improved dc plasma spraying," *Plasma Chemistry and Plasma Processing* 21 p.65-82 (2001)

Thorpe, M. L. and H. J. Richter, "A pragmatic analysis and comparison of HVOF processes," *Journal of Thermal Spray Technology*, Vol. 1, pp.161-170 (1992)

Tsunekawa, Y., M. Hiromura and M. Okumiya, "Nitride formation in synthesis of titanium aluminide matrix composite coatings by reactive rf plasma spraying," *Journal of Thermal Spray Technology*, Vol.9, pp.83-89, (2000)

Vaidya, A., G. Bancke, S. Sampath, and H. Herman, Influence of process variables on the plasma sprayed coatings: an integrated study: in *Thermal Spray: New surfaces for a new Millenium*, 2001, Ed. C.C. Berndt, K.A.Khor, E.F.Lugscheider, Pub. ASM International, Materials Park, Ohio, pp.1-9

Vardelle A, and Themelis N.J., "Transport and chemical rate phenomena in plasma sprays," *High Temperature Materials Processes* 1 (1997) 295-313

Vardelle, A, M.Vardelle, H. Zhang, N.J. Themelis, and K. Gross, "Volatilization of metal powders in plasma sprays," *Journal of Thermal Spray Technology* 11 (2), pp.224-252, 2002

Vardelle, A., P. Fauchais, and N.J. Themelis, "Oxidation of metal droplets in plasma sprays," *Proceeding of the 8<sup>th</sup> National Thermal Spray Conference*, pp.175-180 (1995)

Vardelle, A., P. Fauchais, B. Dussoubs, and N.J. Thermelis, "Heat generation and particle injection in a thermal plasma torch," *Plasma Chemistry and Plasma Processes* 18 pp.551-574, (1998)

Vardelle, M., A. Vardelle, P. Fauchais, K.-I. Li, B. Dussoubs, and N.J. Thermelis, "Controlling particle injection in plasma spraying," *Journal of Thermal Spray Technology*, Vol. 10 pp.267-284 (2001)

Vardelle, M., C. Trassy, A. Vardelle, P. Farchais, "Experimental investigation of powder vaporization in thermal plasma jets," *Plasma Chemistry and Plasma Processing*, Vol.11, pp.185-201, 1991

Vattulainen, J., E. Hamalainen, R. Hernberg, P. Vuoristio, and T. Mantyla, "Novel method for in-flight particle temperature and velocity measurements in plasma spraying using a single CCD camera," *Journal of Thermal Spray Technology*, Vol10, pp.94-104, 2001

Volenik, K., F. Hanousek, P. Charaska, J. Ilavsky, K. Neufuss, "In-flight oxidation of high-alloy steels during plasma spraying," *Materials Science and Engineering*, A272, pp.199-216, 1999

Volenik, K., V. Novak, J. Dubsky, P. Charaska, K. Neufuss, "Properties of alloy steel coatings oxidized during plasma spraying," *Materials Science and Engineering*, A234-236, pp.493-496, 1997

Wan, Y. P., Fincke, J. R., Jiang, X. Y., Sampath, S., Prasad, V., and Herman, H., "Modeling of oxidation of molybdenum particles during plasma spray deposition," *Metallurgical and Materials Transactions B*, Vol.32, pp.475-481 (2001)

Wan, Y. P., J. R. Fincke, S. Sampath, V. Prasad, H. Herman, "Modeling and experimental observation of evaporation from oxidizing molybdenum particles entrained in a thermal plasma jet," *International Journal of Heat and Mass Transfer*, 45 (2002) 1001-10015

Wan, Y.P., Gupta, V., Deng, Q., Sampath, S., Prasad, V., Williamson, R., and Fincke, J.R., "Modeling and visualization of plasma spraying of functionally graded materials and its application to the optimization of spray conditions," *Journal of Thermal Spray Technology*, Vol.10, pp. 382-389, 2001

Wan, Y.P., Prasad, V., Wang, G.-X., Sampath, S., and Fincke, J.R., "Model and powder particle heating, melting, resolidification, and evaporation in plasma spraying processes," *Journal of Heat Transfer*, Vol. 121, pp. 691-699 (1999)

Wang, G.-X., and Matthys, E. F., "Modeling of nonequilibrium surface melting and resolidification for pure metals and binary alloys," *Transaction of ASME, Heat Transfer Division*, Vol. 118, pp.944-951 (1996)

Welz, S., Y. Gosgotsi and M.J. McNallan, "Nucleation, growth, and graphitization of diamond nanocrystals during chlorination of carbides", *Journal of Applied Physics*, 93 (7), pp.4207-4214, 2003.

Westhoff, R., G. Trapaga, and J. Szekely, "Plasma-particle interaction in plasma spraying systems," *Metallurgical and Materials Transactions B*, Vol.23, pp.683-693, 1992

Wigren, J., J.F. de Vries and D. Greving, "Effects of powder morphology, microstructure, and residual stress on thermal barrier coating thermal shock performance," *Thermal Spray: Practical Solutions for Engineering Problems*, (ed.) C.C. Berndt, (Pub.) ASM Int. OH, USA, pp.855-861, 1996

Williams, F. A., Combustion Theory. 2<sup>nd</sup> Ed., Addison-Wesley, New York, p.380.

Williamson, R.L., Fincke, J.R., Chang, C.H., "A computational examination of the sources of statistical variance in particle parameters during thermal plasma spraying", *Plasma Chemistry and Plasma Processing*, Vol. 20, pp.299-324 (2000)

Xue, S., P. Proulx and M. I. Boulos, "Extended-field electromagnetic model for inductively coupled plasma", *J. Phys. Appl. D*: 34 (2001) 1897-1906.

Xue, S.W., P. Proulx and M.I. Boulos, "Effect of the coil angle in an inductively coupled plasma torch: A novel two-dimensional model," *Plasma Chemistry and Plasma Processing*, Vol. 23, pp.245-263, (2003)

Ye, R., P. Proulx, M. I. Boulos, "Turbulence phenomena in the radio frequency induction plasma torch", *Int. J. of Heat Mass Transfer*. 42 (1999) 1585-1595.

Young, E.J., E.Mateeva, J.J. Moore, B. Mishra, and M. Loch, "Low pressure plasma spray coatings,"

*Thin Solid Films*, pp.377-378, 2000

Yu, M.H., P. S. Devi, L.H. Lewis, P. Oouma, J.B. Parise and R.J. Gambino, "Towards a magnetic core-shell nanostructure: a novel composite made by a citrate-nitrate auto-ignition process", Materials Science and Engineering B 103, pp. 262-270, 2003.

Yushchenko, K., Y. Borisov, Y. Pereverzev, S. Vojnarovitch, "Microplasma spraying," *Thermal Spray: Science and Technology*, USA, (Ed.) C.C. Berndt, (Pub.) ASM Int. OH, USA, pp.1461-1467, 1997

H. Zhang, X.Y. Wang, L.L. Zheng, and X.Y. Jiang, Studies of splat morphology and rapid solidification during thermal spraying, *Int. J. Heat Mass Transfer* 44 (2001) 4579-4592.

Zhang, H., H.B. Xiong, L.L. Zheng, A. Vaidya, L. Li, and S. Sampath: in *Thermal Spray: advancing the science and applying the technology*, 2003, Ed. B. M. Marple, and C. Moreau, Pub. ASM International, Materials Park, Ohio, pp.905-911.

Zierhut, J., P. Haslbeck, K.D. Landes, G. Barbezat, "Triplex-an innovative three-cathode plasma torch," *Thermal Spray: Meeting the Challenges of the 21<sup>st</sup> Century*, (Ed.) C. Coddet, (Pub.) ASM Int. OH, USA, pp.1375-1379, 1998